Coherent light-matter interactions in π-conjugated molecules and in their assembly

by

Masazumi Fujiwara

2008

A dissertation submitted to
the Faculty of Department of Physics
Graduate School of Science
in partial fulfillment of the requirements
for the degree of
Doctor of Science

Osaka City University

ABSTRACT

π-conjugated molecular systems show very large optical response in the ultrafast time regime; therefore their characteristic optical property is of great interest in the recent optical physics. The goal of this doctoral work is to give an unified explanation for light-matter interactions occurring in any types of π-conjugated molecular systems. The main points of this dissertation are as follows.

(1) We have measured sub-20-fs time-resolved transient grating (TG) signals in π-conjugated molecules, which have different numbers of C=C bonds (n) from n = 9–15, in order to investigate the dependence of the ultrafast coherent optical response on n. The experimental TG traces can be well reproduced by computational simulations based on time-dependent perturbation theory. It is shown that the decoherence of the ground-state vibrational modes is mainly caused by system-bath interactions. The dephasing time of the C-C stretching mode depends strongly on the conjugation length, whereas that of the C=C stretching does not. This trend clearly shows that the short-chain π-conjugated molecules have a specific major channel of energy dissipation to the environment (the C=C stretching), whereas the long-chain ones do not.

(2) We show that the third-order optical nonlinearity [$\gamma(-3\omega;\omega,\omega,\omega)$] of the π-conjugated molecules can be greatly enhanced without a major red-shift of the absorption spectrum that disturbs optical transparency in the visible region. By changing n of the π-conjugated molecules from 7 to 15, a remarkable 3.4-fold increase of the γ value was observed when n = 15 relative to that of β-carotene, which is one of the largest γ value ever reported. The controversial higher-lying essential state, which has been claimed to be the origin of the large optical nonlinearity of this type of π-conjugated molecules, is not important for generating the large value of γ. Moreover this strong enhancement of $\gamma_{\max}$ mainly originates from three-photon resonance of the lowest optically allowed excited state. Thus changing n provides a way to greatly enhance the optical nonlinearity of π-conjugated molecules, which can be an alternative method that introduces polar constituents into the polyene backbone.

(3) We investigate the linear and second-order optical nonlinearity of a crystal of *N*-benzyl 2-methyl-4-nitroaniline (BNA), which is promising for efficient THz generation. Three d-tensor components of the crystal have been determined to be $d_{333} = 234 \pm 31$, $d_{322} = 15.6 \pm 0.9$, and $d_{311} \sim 0$ (pm/V). We have found that this value of d_{333} is the largest in *yellow-colored* NLO crystals reported so far. Theoretical predictions of the values of the d-tensor components have been performed on the basis of an extended oriented-gas model that incorporates effects of strong hydrogen-bond intermolecular interactions. They provide good agreement between the predicted values and the experimentally determined ones, when the number of BNA molecules in their assembly is increased along the direction of the hydrogen bonds. We propose that the very large enhancement of d_{333} is due to the significant interactions along the hydrogen bonds and its consequent resonance enhancement.

List of the author's works

Scientific paper

1. **M. Fujiwara**, M. Sugisaki, A. Gall, B. Robert, R. J. Cogdell, and H. Hashimoto, "Ultrafast optical responses of β-carotene and lycopene probed by sub-20 fs time-resolved coherent spectroscopy", *submitted to* J. Lumin.

2. Mitsuru Sugisaki, **Masazumi Fujiwara**, Ritsuko Fujii, Katsunori Nakagawa, Mamoru Nango, Richard J. Cogdell, and Hideki Hashimoto, "Transient grating spectroscopy in photosynthetic purple bacteria *Rhodobacter spaeroides 2. 4. 1*", *submitted to* J. Lumin.

3. **Masazumi Fujiwara**, Kensei Yamauchi, Mitsuru Sugisaki, Andrew Gall, Bruno Robert, Richard J. Cogdell, and Hideki Hashimoto, "Large Third-Order Optical Nonlinearity Realized in Symmetric Nonpolar Carotenoids", Phys. Rev. B **78**, 161101(R) (2008).

4. **Masazumi Fujiwara**, Kensei Yamauchi, Mitsuru Sugisaki, Andrew Gall, Bruno Robert, Richard J. Cogdell, and Hideki Hashimoto, "Energy dissipation in the ground-state vibrational manifolds of β-carotene homologues: a sub-20-fs time-resolved transient grating spectroscopic study", Phys. Rev. B **77**, 205118 (2008).

5. Katsuhiko Miyamoto, Hiroaki Minamide, **Masazumi Fujiwara**, Hideki Hashimoto, and Hiromasa Ito, "Coherent tunable monochromatic THz-wave generation using N-Benzyl-2-methyl-4-nitroaniline (BNA) crystal", Opt. Lett. **33**, 252 (2008).

6. Mitsuru Sugisaki, **Masazumi Fujiwara**, Kazuhiro Yanagi, Richard J. Cogdell, and Hideki Hashimoto, "Four-wave mixing signals from β-carotene and its $n = 15$ homologue", Photosynth. Res. **95**, 299 (2008).

7. **Masazumi Fujiwara**, Minoru Maruyama, Hironori Takahashi, Shin-ichiro Aoshima, Richard J. Cogdell, and Hideki Hashimoto, "Determination of the *d*-tensor components of a single crystal of *N*-benzyl 2-methyl-4-nitroaniline", Jpn. J. Appl. Phys. **46**, 1528 (2007).

8. **Masazumi Fujiwara**, Kazuhiro Yanagi, Minoru Maruyama, Mitsuru Sugisaki, Kazuyoshi Kuroyanagi, Hironori Takahashi, Shin-ichiro Aoshima, Yutaka Tsuchiya, Andrew Gall, and Hideki Hashimoto,
"Second order nonlinear optical properties of the single crystal of *N*-benzyl 2-methyl-4-nitroaniline: anomalous enhancement of the d_{333} component and its possible origin", Jpn. J. Appl. Phys. **45**, 8676 (2006).

9. Kazuyoshi Kuroyanagi, **Masazumi Fujiwara**, Hideki Hashimoto, Hironori Takahashi, Shin-ichiro Aoshima, and Yutaka Tsuchiya,
"Determination of the Refractive Indices and Absorption Coefficients of Highly Purified N-Benzyl-2-methyl-4-nitroaniline Crystal in Terahertz Frequency Regime", Jpn. J. Appl. Phys. **45**, L761 (2006).

10. Kazuyoshi Kuroyanagi, **Masazumi Fujiwara**, Hideki Hashimoto, Hironori Takahashi, Shin-ichiro Aoshima, and Yutaka Tsuchiya,
"All Organic THz Electromagnetic Wave Emission and Detection Using Highly Purified N-Benzyl-2-Methyl-4-Nitroaniline Crystals",
Jpn. J. Appl. Phys. **45**, 4068 (2006).

Conference proceedings

1. Katsuichi Kanemoto, Mitsuru Sugisaki, **Masazumi Fujiwara**, Tsutomu Karasawa, Hideki Hashimoto
"Ultrafast coherent vibronic oscillations in regioregular poly(3-alkylthiophene)", Phys. Stat. Solidi (c), *in press*.

2. **Masazumi Fujiwara**, Kensei Yamauchi, Mitsuru Sugisaki, Kazuhiro Yanagi, Andrew Gall, Bruno Robert, Richard J. Cogdell, and Hideki Hashimoto,
"Third-order optical nonlinearity of β-carotene homologues",
Phys. Stat. Solidi (c), *in press*.

3. Mitsuru Sugisaki, **Masazumi Fujiwara**, Selvakumar V. Nair, Harry E. Ruda, Richard J. Cogdell, and Hideki Hashimoto,
"Spectrally-resolved Transient Grating Signals from β-carotene in Benzene Solution", *submitted to* Phys. Stat. Solidi (c).

4. **Masazumi Fujiwara**, Kensei Yamauchi, Mitsuru Sugisaki, Andrew Gall, Bruno Robert, Richard J. Cogdell, and Hideki Hashimoto,
"Specific Channel of Energy Dissipation in Carotenoids: Coherent Spectroscopic Study", in *Ultrafast Phenomena XVI, Springer Series in Chemical Physics*, edited by P. Corkum, S. De Silvestri, K. Nelson, E. Riedle and R. Schoenlein, *in press*.

5. Mitsuru Sugisaki, **Masazumi Fujiwara**, Kazuhiro Yanagi, Ritsuko Fujii, Richard J. Cogdell, and Hideki Hashimoto,

"Coherent spectroscopy of carotenoid and bacteriochlorophyll", in *Photosynthesis. Energy from the Sun: 14th International Congress on Photosynthesis*, edited by J. F. Allen, E. Gantt, J. H. Golbeck, and B. Osmond (Springer-Verlag, Berlin, 2008), p. 259–262.

6. **M. Fujiwara**, K. Yamauchi, and H. Hashimoto, "THG Maker Fringes in β-carotene Homologues", Carotenoid Science **11**, 32 (2007).

List of international conference talks

1. H. Hashimoto, Mitsuru Sugisaki, **Masazumi Fujiwara**, and Richard J. Cogdell "Sub-20-fs coherent spectroscopy of carotenoids", ESF Workshop "Novel Methods in Exploring Carotenoid Excited State Dynamics", September, 2008, Nove Hrady, Czech.

2. **M. Fujiwara**, K. Yamauchi, M. Sugisaki, K. Yanagi, A. Gall, B. Robert, R. J. Cogdell, and H. Hashimoto, "Third-Order Optical Nonlinearity of β-Carotene Homologues Investigated by Third-Harmonic Generation Spectroscopy", No: No.5 of Organics III session, Third International Conference on Optical, Optoelectronic and Photonic Materials and Applications, July, 2008, Edmonton, Canada.

3. M. Sugisaki, **M. Fujiwara**, S. V. Nair, H. E. Ruda, R. J. Cogdell, and H. Hashimoto, "Spectrally-resolved Transient Grating Signal of β-carotene", No: No.3 of Organics II session, Third International Conference on Optical, Optoelectronic and Photonic Materials and Applications, July, 2008, Edmonton, Canada.

4. Mitsuru Sugisaki, **Masazumi Fujiwara**, Ritsuko Fujii, Katsunori Nakagawa, Mamoru Nango, Richard J. Cogdell, and Hideki Hashimoto, "Vibronic Coherence of Photosynthetic Pigments", No: MoC-O1, The 15th International Conference on Luminescence and Optical Spectroscopy of Condensed Matter (ICL08), July, 2008, Lyon, France.

5. **Masazumi Fujiwara**, Mitsuru Sugisaki, Andrew Gall, Bruno Robert, Richard J. Cogdell, and Hideki Hashimoto, "Ultrafast optical responses of β-carotene and lycopene probed by sub-20 fs time-resolved coherent spectroscopy", No: We-P-154, The 15th International Conference on Luminescence and Optical Spectroscopy of Condensed Matter (ICL08), July, 2008, Lyon, France.

6. Katsuhiko Miyamoto, **Masazumi Fujiwara**, Hiroaki Minamide, Hideki Hashimoto, and Hiromasa Ito, "Bridgman method grown BNA crystal for wideband THz-wave generation", No: We-P-071, The 15th International Conference on Luminescence and Optical Spectroscopy of Condensed Matter (ICL08), July, 2008, Lyon, France.

7. Andrew Gall, **Masazumi Fujiwara**, Kensei Yamauchi, Mitsuru Sugisaki, Bruno Robert and Hideki Hashimoto, "Resonance Raman Spectroscopy of β-carotene Homologues Containing Different π-Conjugation Lengths and Side Chain Distributions", The 15th International Symposium on Carotenoids, June, 2008, Okinawa, Japan.

8. **Masazumi Fujiwara**, Kensei Yamauchi, Mitsuru Sugisaki, Kazuhiro Yanagi, Andrew Gall, Bruno Robert, Richard J. Cogdell, and Hideki Hashimoto, "A New Optically-Forbidden Excited State in β-Carotene Homologues: Investigated by Third-Harmonic Generation Spectroscopy", The 15th International Symposium on Carotenoids, June, 2008, Okinawa, Japan.

9. **Masazumi Fujiwara**, Mitsuru Sugisaki, Andrew Gall, Bruno Robert, Richard J. Cogdell, and Hideki Hashimoto, "Sub-20 fs time-resolved degenerate four-wave mixing spectroscopy of β-carotene and lycopene", The 15th International Symposium on Carotenoids, June, 2008, Okinawa, Japan.

10. Mitsuru Sugisaki, **Masazumi Fujiwara**, Selvakumar V. Nair, Harry E. Ruda, Richard J. Cogdell, and Hideki Hashimoto, "Spectrally-resolved Transient Grating Signals from β-carotene in Benzene Solution", The 15th International Symposium on Carotenoids, June, 2008, Okinawa, Japan.

11. Mitsuru Sugisaki, **Masazumi Fujiwara**, Ritsuko Fujii, Katsunori Nakagawa, Mamoru Nango, Richard J. Cogdell, and Hideki Hashimoto, "Transient Grating Spectroscopy in Rhodobactor sphaeroides 2.4.1", The 15th International Symposium on Carotenoids, June, 2008, Okinawa, Japan.

12. **M. Fujiwara**, K. Yamauchi, M. Sugisaki, A. Gall, B. Robert, R. J. Cogdell, and H. Hashimoto, "Specific Channel of Energy Dissipation in Carotenoids: Coherent Spectroscopic Study", No: MON5I.3, XVI International Conference on Ultrafast Phenomena, June, 2008, Stresa, Italy.

13. **Masazumi Fujiwara**, "Nonlinear Optical Spectroscopic Studies on β-carotene homologues", Private Seminar of Prof. Marcus Motzkus Laboratory at Philipps Universität Marburg, on June 6th, 2008, Marburg, Germany.

14. Katsuhiko Miyamoto, Hiroaki Minamide, **Masazumi Fujiwara**, Hideki Hashimoto, and Hiromasa Ito, "0.1-15THz Generation Using BNA (N-Benzyl-2-Methyl-4-Nitroaniline) Crystal", No: CTuHH6, Conference on Lasers and Electro-Optics (CLEO) 2008, May, 2008, San Jose, USA.

15. K. Miyamoto, H. Minamide, **M. Fujiwara**, H. Hashimoto, H. Ito "Coherent tunable monochromatic terahertz-wave generation using N-Benzyl-2-methyl-4-nitroaniline (BNA) crystal", No: 6875-11, SPIE Photonics West 2008, January, 2008, San Jose.

16. **M. Fujiwara**, K. Yamauchi, M. Sugisaki, A. Gall, B. Robert, R. J. Cogdell, and H. Hashimoto, "Ultrafast dephasing processes in β-carotene homologues", 2nd International Workshop on Photosynthetic Antennae and Coherent Phenomena, No: Oral 6, December, 2007, Osaka, Japan.

17. D. Kosumi, K. Abe, **M. Fujiwara**, H. Hashimoto, and M. Yoshizawa, "Ultrafast S_1 dynamics induced by two-photon excitation in all-trans-β-carotene", 2nd International Workshop on Photosynthetic Antennae and Coherent Phenomena, No: Poster 17, December, 2007, Osaka, Japan.

18. K. Yamauchi, **M. Fujiwara**, M. Sugisaki, and H. Hashimoto, "THG Maker Fringe Measurements of β-carotene Homologues", 2nd International Workshop on Photosynthetic Antennae and Coherent Phenomena, No: Poster 10, December, 2007, Osaka, Japan.

19. M. Sugisaki, **M. Fujiwara**, and H. Hashimoto, "Coherent spectroscopy of photosynthetic pigments", 2nd International Workshop on Photosynthetic Antennae and Coherent Phenomena, No: Poster 6, December, 2007, Osaka, Japan.

20. M. Sugisaki, **M. Fujiwara**, K. Yanagi, R. Fujii, R. J. Cogdell, and H. Hashimoto, "Coherent Spectroscopy in Carotenoid and Bacteriochlorophyll", 14th International Congress on Photosynthesis, July, 2007, Glasgow, UK.

21. **M. Fujiwara**, M. Maruyama, M. Sugisaki, K. Kuroyanagi, H. Takahashi, S. Aoshima, Y. Tsuchiya, and H. Hashimoto, "Linear and nonlinear optical properties of a single crystal of *N*-benzyl 2-methyl-4-nitroaniline", International Workshop on Photosynthetic Antennae and Coherent Phenomena, No: Poster 6, December, 2005, Osaka, Japan.

List of domestic conference talks

1. M. Sugisaki, **M. Fujiwara**, R. Fujii, and Hideki Hashimoto, "Degenerated Four-wave-mixing Signals from photosynthetic purple bacteria *Rba. Sphaeroides 2.4.1*", No: 22aPS-66, 2008 Autumn Meeting of The Physical Society of Japan, September, 2008, Iwate University.

2. **M. Fujiwara**, K. Yamauchi, M. Sugisaki, and H. Hashimoto, "Qubic optical nonlinearity in π-conjugated molecules", No: 21pYH-5, 2008 Autumn Meeting of The Physical Society of Japan, September, 2008, Iwate University.

3. H. Hashimoto, M. Sugisaki, **M. Fujiwara**, R. Fujii, and R. J. Cogdell, "Functions of light-harvesting antenna pigment-protein complex investigated by ultrafast laser spectroscopy", No. 5S4-05, 88th Annual Meeting of The Chemical Society of Japan, March, 2008, Rikkyo University.

4. K. Miyamoto, **M. Fujiwara**, H. Minamide, H. Hashimoto, and H. Ito, "Wide-frequency THz generation using organic nonlinear optical crystal BNA", No. 29P-ZH-15, 55th Annual Meeting of The Japan Society of Applied Physics, March, 2008, Nippon University.

5. D. Kosumi, K. Abe, **M. Fujiwara**, H. Hashimoto, and M. Yoshizawa, "Excitation energy dependence of the S_1 dynamics induced by two-photon excitation in all-*trans*-β-carotene", No: 26pPS-34, 63th Annual Meeting of The Physical Society of Japan, March, 2008, Kinki University.

6. M. Sugisaki, **M. Fujiwara**, and H. Hashimoto, "Excitation energy dependence of degenerate four-wave mixing signals from β-carotene", No: 26pPS-29, 63th Annual Meeting of The Physical Society of Japan, March, 2008, Kinki University.

7. **M. Fujiwara**, M. Sugisaki, and H. Hashimoto, "Temporal frequency shift of vibronic coherent oscillation", No: 26pPS-28, 63th Annual Meeting of The Physical Society of Japan, March, 2008, Kinki University.

8. D. Kosumi, **M. Fujiwara**, R. Fujii, H. Hashimoto, and M. Yoshizawa "Ultrafast optical responses and multi-photon excitation process of carotenoids exploring by non-resonant excitation" No: 23pPSA-93, 62th Annual Meeting of The Physical Society of Japan, September, 2007, Hokkaido University.

9. **M. Fujiwara**, K. Yamauchi, M. Sugisaki, and H. Hashimoto "Ultrafast optical dynamics in β-carotene homologues" No: 23pPSA-90, 62th Annual Meeting of The Physical Society of Japan, September, 2007, Hokkaido University.

10. K. Yamauchi, **M. Fujiwara**, M. Sugisaki, and H. Hashimoto "THG Maker fringe measurement of β-carotene homologs" No: 23pPSA-89, 62th Annual Meeting of The Physical Society of Japan, September, 2007, Hokkaido University.

11. K. Yamauchi, **M. Fujiwara**, M. Sugisaki, H. Hashimoto "THG Maker Fringe Measurements in β-carotene homologues" No: 29, 21th Annual Meeting of Japanese Society for Carotenoid Research, September, 2007, Osaka City University.

12. **M. Fujiwara**, K. Yamauchi, M. Sugisaki, H. Hashimoto "Ultrafast optical processes in β-carotene homologues" No: 28, 21th Annual Meeting of Japanese Society for Carotenoid Research, September, 2007, Osaka City University.

13. M. Sugisaki, **M. Fujiwara**, H. Hashimoto "Four-wave mixing signals in β-carotene: excitation energy dependence" No: 27, 21th Annual Meeting

of Japanese Society for Carotenoid Research, September, 2007, Osaka City University.

14. **M. Fujiwara**, K. Yamauchi, H. Hashimoto "THG Maker Fringe Measurements in β-carotene homologues" No: 3, 20th Annual Meeting of Japanese Society for Carotenoid Research, September, 2006, Hotel Moon Beach.

15. **M. Fujiwara**, M. Maruyama, M. Sugisaki, K. Kuroyanagi, H. Takahashi, S. Aoshima, Y. Tsuchiya, and H. Hashimoto "Determination of the second-order nonlinear susceptibilities of a single crystal of *N*-benzyl 2-methyl-4-nitroaniline" No: 26a-M-6, 53th Annual Meeting of The Japan Society of Applied Physics, March, 2006, Musashi Institute of Technology.

16. **M. Fujiwara**, M. Maruyama, M. Sugisaki, K. Kuroyanagi, H. Takahashi, S. Aoshima, Y. Tsuchiya, and H. Hashimoto "Charge Transfer Excitons in the quadratic optical nonlinear crystal, *N*-benzyl 2-methyl-4-nitroaniline" No: 28aPS-17, 61th Annual Meeting of The Physical Society of Japan, March, 2006, Ehime University and Matsuyama University.

17. **M. Fujiwara**, M. Maruyama, M. Sugisaki, K. Kuroyanagi, H. Takahashi, S. Aoshima, Y. Tsuchiya, and H. Hashimoto "Linear and second-order optical properties of a *N*-Benzyl MNA single crystal", No: II-A-43, 16th Annual Meeting of Association for Condensed Matter Photophysics, December, 2005, Osaka City University.

18. **M. Fujiwara**, K. Yanagi, M. Maruyama, M. Sugisaki, K. Kuroyanagi, H. Takahashi, S. Aoshima, Y. Tsuchiya, and H. Hashimoto "Second-order optical properties of a *N*-Benzyl MNA single crystal", No: 24aps-49, 60th Annual Meeting of The Physical Society of Japan, March, 2005, Tokyo University of Science.

19. **M. Fujiwara**, K. Yanagi, M. Maruyama, M. Sugisaki, K. Kuroyanagi, H. Takahashi, S. Aoshima, Y. Tsuchiya, and H. Hashimoto "Second-order optical properties of a *N*-Benzyl MNA single crystal", No: IV-97, 15th Annual Meeting of Association for Condensed Matter Photophysics, December, 2004, Kyoto University.

ACKNOWLEDGMENTS

First of all, I would like to thank my supervisor, Prof. Dr. Hideki Hashimoto for his 6-year guidance of my doctoral work. He gave me the greatest working place. Studying in his laboratory was really exciting for me because there was everything we needed for high-quality scientific research, *e.g.* fascinating laboratory equipment, and a good atmosphere that stimulates research. Off course, scientific discussion with him was the most important thing, which he provided for me. Furthermore he showed me how to advance scientific research, *i.e.* what topic is important in science, how to manage laboratory, how to write a paper. I believe that all that he gave me in these 6 years will be a firm foundation for my future research life.

I would like to thank Prof. Dr. Mitsuru Sugisaki. He supported me with many scientific suggestions and discussions about the whole part of this dissertation. His scientific suggestions are always very good points, so that I have really enjoyed a scientific *catch ball* with him. I would like to emphasize that his suggestions greatly refined the quality of my doctoral work. The present quality of this dissertation would have never been accomplished without his support.

I appreciate the generous support of Prof. Dr. Richard Cogdell at University of Glasgow, UK. He gave me valuable discussions about almost all of the works included in this dissertation. Also he told me what Science is. I cannot remember the exact words he said, but he surely told me "Scientific research should fascinate people. Such a research is always difficult and takes a long time and an enormous amount of work, but this is Science we should do." I have been strongly motivated by these words. I am delighted to have shared the work with him in this start-up time of my long research career.

For the contributions of the carotenoid research, I appreciate the contributions of Prof. Dr. Bruno Robert and Dr. Andrew Gall at Centre National de la Recherche Scientifique (CNRS), France. They provided me with several experimental results and fruitful discussion. I would like to thank Dr. Kazuhiro Yanagi at National Institute of Advanced Industrial Science and Technology, Japan. He has constantly encouraged me to do good scientific research, since I joined the laboratory. It was great time for me when we constructed the Maker fringe setup. I would like to thank Prof. Dr. Masayuki Yoshizawa at Tohoku University, Japan. He gave me many insightful questions and suggestions on the carotenoid research. I am grateful for the collaborations with Dr. Ritsuko Fujii and Dr. Daisuke Kosumi at our laboratory.

For the contributions of the THz research, I would like to thank Prof. Dr. Hiromasa Ito, Dr. Katsuhiko Miyamoto, and Dr. Hiroaki Minamide at RIKEN, Japan. It was exciting for me to participate in the collaborative research on the THz generation using BNA crystals, with one of the most famous laboratories in the THz research field. In particular, Dr. Miyamoto has encouraged me all the time since we first met. I was very happy to share the time with him in Photonics West. I would like to thank Prof. Dr. Yutaka Tsuchiya at The Graduate School for The

Creation of New Photonics Industries, Japan, who is unfortunately not with us. Also I would like to thank Dr. Shin-ichiro Aoshima, Mr. Hironori Takahashi, and Dr. Kazuyoshi Kuroyanagi at Hamamatsu Photonics, Japan. I am very happy to share the works on THz generation using BNA with them. I am grateful for the support of Prof. Dr. Minoru Maruyama at our laboratory. He advised me on the crystallization of the BNA crystal.

Many thanks should be given to Mr. Kensei Yamauchi. He is my good friend and was 3-year collaborator at Osaka City University. I appreciate that Dr. Keisuke Saito at our laboratory provided me with very fruitful discussions about the dissertation. I am grateful for Mr. Toshiyuki Kusumoto that we have shared much time to discuss physics since we got into our university 8 years ago. Also, I would like to thank all of the members of our laboratory who have shared the time with me.

Financial support from Japan Society for the Promotion of Science is gratefully acknowledged.

Finally I would like to thank those who have supported me in every part of my life. The fellowship in the Abiko Baptist Church has really strengthened me all the time. They always accepted me as a *member of the household of God*. My loving family, Tsuyoshi, Hiromi, and Naozumi have always supported me with their abundant love, since I decided to study in the doctoral course. My special thanks is given to my fiancée Akiko. She knows every difficulty I had in the doctoral course, and has given me a proper encouragement for each difficulty.

Contents

Chapter 1

Introduction

1.1 Light-matter interactions in π-conjugated molecular systems

1.1.1 Importance of π-conjugated molecular systems in the study of light-matter interactions

The present doctoral work is motivated by the urge to give a unified explanation for light-matter interactions occurring in any types of complicated π-conjugated molecular systems. Light-matter interaction is one of the fundamental physical processes that can be seen everywhere in our daily life. In biological systems, for example, it triggers many kinds of physiological functions such as photosynthesis in various living organisms (higher plants, algae, phototropic prokaryotes, bacteria, *etc* ...) [1–3], photochemical reactions in our eyes [4, 5], and so on. The first step of most of these biological reactions is in a certain class of photosensitive biological molecules, *i.e.* π-conjugated molecules whose optical response is characterized by π-electrons that delocalize in the molecule. In general, π-conjugated molecules show very large optical response, therefore, it seems reasonable that nature selects these photosensitive molecules for the main constituents of the light receptors. Characteristic time of the optical response in π-conjugated molecules varies from milliseconds to femtoseconds, depending on the molecular structures as well as on the optical processes involved, as we see a wide range of timescale in the excited-state dynamics of carotenoids (one of the main topics of this thesis) [6]. In particular, the ultrafast optical response of the π-conjugated molecules occurring in sub-picosecond timescale has attracted much attention in relation with the above-mentioned biological activities.

Such an ultrafast photosensitive character of π-conjugated molecules is also very important for photonic device applications [7]. Their large and ultrafast optical response facilitates use of nonlinear optical (NLO) phenomena in photonic devices, which is a key to the realization of *all-optical* devices that may dramatically reduce the processing time of computation in comparison with modern electronic devices. Notably, π-conjugated molecules show various optical prop-

erties depending on the molecular structures, extent of π-electron delocalization, and correlations of molecules in their molecular assembly. Unfortunately, it is still very difficult for basic physics to explain how this attractive photosensitive characters of π-conjugated molecules are changed with increasing the size of the molecular system. Low-dimensional π-conjugated molecular systems are thus an ideal target for the study of light-matter interactions, because its structure is modifiable by using techniques of organic chemistry. For the detailed understanding on the light-matter interactions, it is vitally important to provide a unified physical explanation of the light-matter interaction processes that occur in π-conjugated molecular systems.

1.1.2 Two cases of typical photosensitive π-conjugated molecular systems

We will now briefly mention two typical cases, in which observed optical properties of π-conjugated molecular system are greatly changed by structurally controlling the light-matter interaction processes.

Case 1: photosynthetic light-harvesting complexes

One of the most impressive examples that nature utilizes the light-matter interactions for biological activity is the primary process of photosynthesis. It is an light-to-biochemical energy conversion process, which finally produces ATP (adenosine tri-phosphate). This reaction starts by capturing photons in light-harvesting antenna complexes, LH1 and LH2 [see Fig. 1.1 (a)] [2]. The light energy captured by these antenna complexes is transferred to the reaction center (RC), in which charge separation occurs. This charge is used to generate ATP in the subsequent processes. In terms of the light-matter interactions, mechanisms of energy transfer within either of these light-harvesting complexes and also between each of these complexes are of strong interest because these energy flows occur within a very short period of time, together with high efficiency.

In purple photosynthetic bacteria, molecules of two types of π-conjugated pigments [carotenoid and bacteriochlorophyll (BChl)] are spatially arranged in the binding sites of proteins to organize *supramoleular* assembly in the light-harvesting complexes (see Refs. [8–10] for the details of *supramoleule*). BChls absorb both ultraviolet and near-infrared spectral regions of light, and carotenoids absorb its blue-green region [see Fig. 1.1 (b)]. In the LH2, the light energy absorbed by carotenoids is transferred to either of two distinct kinds of BChl rings, which are named B800 and B850 for their respective peak positions of near-infrared absorption bands. There are two pathways for these energy transfers from carotenoids to BChls [see Fig. 1.1 (c)]. One is from the lowest optically allowed state (S_2) of carotenoids to second excited state of BChls (Q_X), which occurs in the timescale of 100 fs. Another pathway is from the lowest optically forbidden state of carotenoids (S_1) to BChl's first excited state (Q_Y) in the time range of 1–40 ps. It should be noted that it has not been clarified yet which BChl ring is the main

acceptor of energy from carotenoids, therefore we have simply denoted the accepting absorption band of BChl as Q_Y, which is the intrinsic excited state of BChls (the B800 and B850 exciton band derive from the Q_Y state). The overall efficiency of the energy transfer from carotenoids to BChls varies from 50 to ∼100% contingent upon the extent of π-conjugation length of carotenoids. The energy, coming from carotenoids, is then sequentially transferred to the adjacent BChl molecules within each of the rings as shown in Fig. 1.1. These flows of energy occur in the sub-ps time regime with a very high quantum yield of ∼1.0 [1, 11–14]. The mechanism of these efficient and ultrafast energy transfers have been intensively studied.

In real photosynthetic membrane, the LH1-RC complexes are surrounded by the LH2s. Ratio of LH2 to LH1-RC depends on the growth condition, specifically on the amount of sunlight irradiated in the growth time. This indicates that the purple photosynthetic bacteria optimize the amount of energy in the RC that is transferred from the surrounding LH2s. The energy transfer among different complexes is very efficient and ultrafast as well as that within the complex. The lifetime of energy transfer from LH2 to LH1 is 3–5 ps, much shorter than that between LH1 to RC, which occurs in ∼ 50 ps. In other words, the energy captured by the peripheral LH2s is stored in the LH1, and only necessary amount of energy is used for making charge separation in the RC at any time when the energy is required. This energy-storing system is vitally important to prevent unnecessary charge separation in the RC, which eventually leads to efficient energy use.[§]

Recent studies clarified that the ultrafast energy transfer within the complexes cannot be explained in terms of the conventional Förster theory, where individual constituent BChl molecules are assumed to be isolated [15–18]. Instead, it is able to be described with the non-conventional Förster theories such as generalized Förster or Redfield theories [16, 18], which take account of excitonic correlations (coherence) between pigment molecules. In addition, coherent wavelike energy transfer has been proposed as a possible mechanism of this efficient energy transfer system of the light-harvesting complexes, on the basis of the observation of long-lasting excitonic coherence in the Fenna-Matthews-Olson (FMO) BChl light-harvesting complexes [19, 20]. The characteristic of this wavelike energy transfer makes it possible, in vast areas of phase space, to find the most efficient pathway immediately, in contrast to the conventional hopping process of Frenkel exciton, opposite to wavelike migration [1]. It should also be emphasized that the long-lasting excitonic coherence in the complex is a remarkable observation. Since the protein environment strongly affects the optical response due to its significant electrostatic interactions to the pigments [14, 21, 22], this outstanding observation naturally leads us to plausible explanation that the protein environment protects the excitonic coherence [18]. These are the strong evidence that the constituent pigment molecules are effectively assembled to produce new biological functions, which the isolated molecules themselves do not have. Proteins act as

[§]This energy transfer is always *downhill* process; *i.e.* the energy storing excited state of RC is located below compared to all other excited states of peripheral antenna complexes.

smart matrix to manipulate the optical responses of the complicated biological systems by choosing proper π-conjugated molecules and effectively assembling them in order to obtain preferable biological functions.

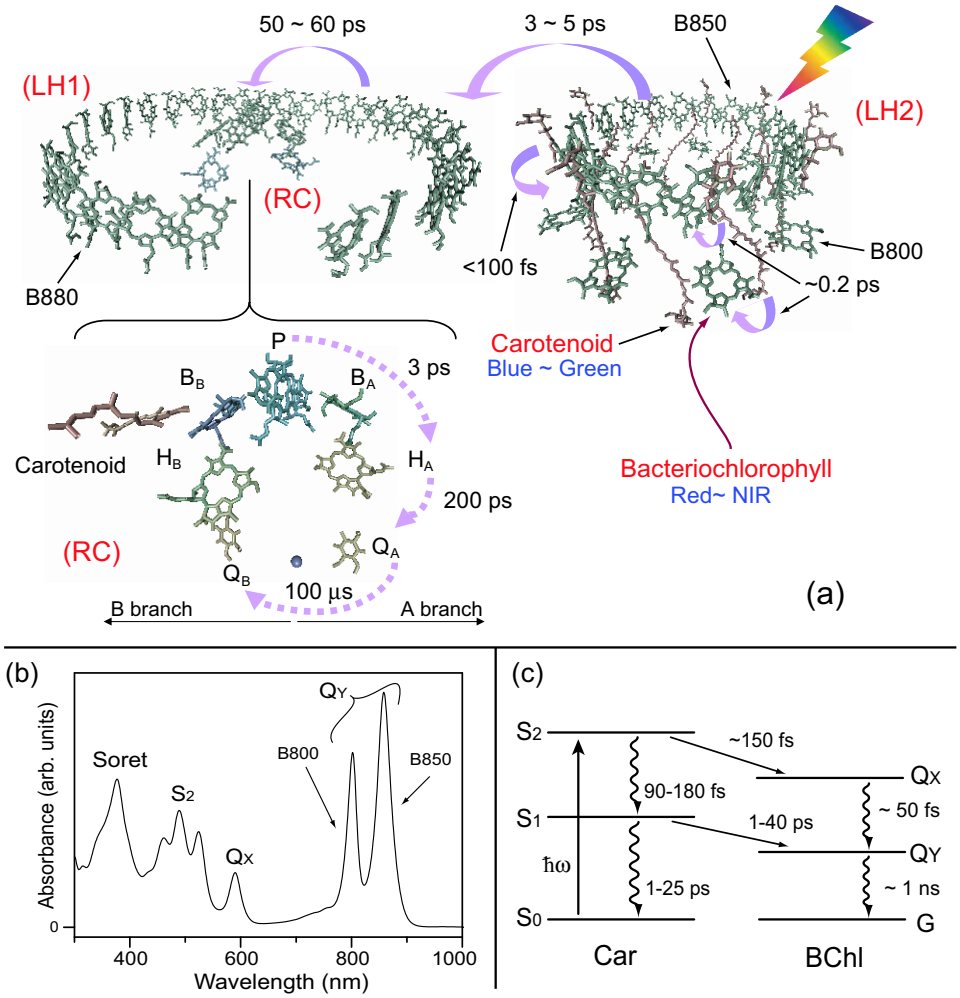

Figure 1.1: (a) A schematic illustration of the primary process of photosynthesis in purple bacteria [2]. (b) Absorption spectrum of LH2 taken from *Rps. acidophila*. BChl has three absorption bands, Soret, Q_X, and Q_Y, while carotenoid has one absorption band coming from S_2. Note that there is a optically forbidden state below S_2 state, S_1, which involves energy transfer to the Q_Y state. (c) The energy flow diagram between carotenoids and BChls. The straight arrow indicates energy transfer, whereas the wavy arrow does internal conversion. The energy absorbed by the carotenoids is transferred to BChls through two pathways as shown in Fig. (c). The energy trapped by the LH2 is moved to the LH1 in 3–5 ps. After 50 to 60 ps, the energy reaches the RC. In the RC, the energy is used to cause charge separation at special pair unit of BChls (P). The electron generated at P is sequentially transferred: $P \rightarrow$ accessory BChl (B_A) $\rightarrow$ bacteriopheophytin (H_A) $\rightarrow$ quinone of A branch (Q_A). The electron then goes to another quinone (Q_B). Finally Q_B is stored in "quinone pool" for the use of the subsequent ATP synthesis. The time constants are described elsewhere [11–14].

Case 2: nonlinear optical materials for photonic device applications

The other extreme of an impressive example that shows the importance of light-matter interactions in π-conjugated systems can be found in the study for NLO photonic device applications. The photosensitive character of π-conjugated molecules is promising for photonic device applications, such as ultrafast photoswitch or efficient frequency converter [7]. For the device applications, largeness of optical nonlinearity is of particular concern because magnitudes of the optical nonlinearity of all π-conjugated molecules ever reported are not enough for the requirements for practical applications [23]. Therefore, a huge amount of effort has been devoted to find a strategy that greatly enhances the optical nonlinearity of π-conjugated molecules [7, 23–25]. In order to enlarge the optical nonlinearity beyond the present maximum value, the relation between extent of π-electron delocalization and the optical nonlinearity is especially important due to the fact that the extent of π-electron delocalization dominates the optical properties of π-conjugated molecules. Indeed, Kuzyk *et. al.* showed that theoretical limit of the magnitude of the optical nonlinearity is simply determined by the number of delocalized π-electrons in a π-conjugated structure [26]. In an extended work based on this principle, they proposed that the largest optical nonlinearity ever reported may be multiplied by a factor of 30 [27]. The understanding of the dependence of the NLO property on the extent of π-electron delocalization is strongly desired for realizing the ultimate magnitude of the optical nonlinearity in π-conjugated molecules.

More recently, the study of the NLO optical response of π-conjugated molecular crystals, together with vast knowledge of crystal engineering, has led to realization of efficient terahertz (THz) light sources [28, 29]. THz wave is an electromagnetic wave whose frequency is located between radio frequency and light frequency ($0.1–30\times10^{12}$ Hz, see Fig. 1.2). It is, for example, very promising for imaging and spectroscopy [28–39]. THz wave was, historically, generated by using synchrotron radiation (or free-electron laser), which are too large to be accommodated in small laboratory space, and hence not be preferable for conventional experiments [29, 40, 41]. The advent of the femtosecond Ti:Sapphire laser made efficient THz generation technique widely available. There are two types of techniques of femtosecond THz pulse generation: one is by use of photoconductive switch, and the other is by means of differential frequency generation (optical rectification) process in NLO crystals. As for the latter case, organic NLO crystals (most of them are π-conjugated molecular crystals) have much larger optical

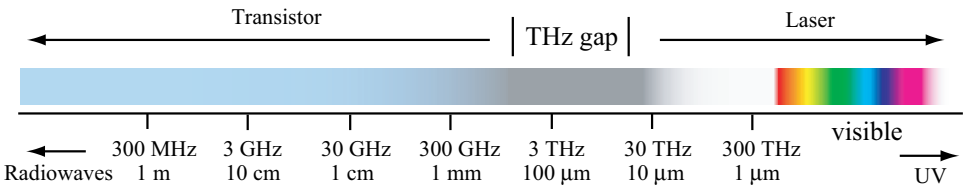

Figure 1.2: THz wave as one of various kinds of electromagnetic wave.

nonlinearity than that of inorganic NLO crystals, such as ZnTe or GaP [29]. In many cases, the optical properties of the π-conjugated molecular crystals cannot be only ascribed to those of the isolated molecule, as pointed out by number of researchers [42–47]. In these crystals, π-conjugated molecules form a supramolecular cluster through intermolecular interactions, which results in the enhancement of the optical nonlinearity. Thus the relation between the supramolecular state and the optical nonlinearity should be clarified in order to develop effective NLO crystals.

1.2 Optical polarization of a complex system

A physical quantity, into which light-matter interactions are incorporated, is optical polarization. It can be considered as the only material quantity that appears in the Maxwell equations because most of dielectric media of our interest have very small magnetic permeability compared to their electric susceptibility: the effect of the optical magnetic field is typically smaller than that of the electric field by a factor of 10^{-2} [48, 49]. In a simplest two-level material system that comprises the ground state, $|g\rangle$, and excited state, $|e\rangle$, the optical polarization ($\boldsymbol{p}$) of the system is given by $\boldsymbol{p} = q\langle e|\boldsymbol{r}|g\rangle$, where q and $\boldsymbol{r}$ indicate an electric charge and a displacement vector, respectively. In this case, the optical response of the system is completely known. It is, however, obvious that optical responses of almost of all materials that we can see in the world cannot be explained in such a very simple framework. For example, a molecule of dye in a solvent has infinitely large number of eigenstates due to electron-vibration and solute-solvent interactions [50, 51], even if the molecule itself affords the simple two electronic levels in gaseous phase.

Owing to recent high performance computing resources available, various types of numerical calculations, such as quantum chemical calculations or molecular dynamics simulations, can be applied to a quite large system, including a dye molecule in solvent and a biological protein complex, for example [52–56]. In fact, these calculations have made significant progress in material science. However, they are not conceptually new in physics. If the computational capacity is increased much more, these calculations could be possible to provide more accurate predictions of the experimental data. The problem is that they have not moved basic physical concept forward from the simple two-level system, because the essence of these calculation is a reduction of one many-body (or many-eigenstate) problem to a set of large number of simple two-level problems (or several-level problems at most) by using many approximations. These types of calculations frequently hinder us to get a clear insight into an essential physics that governs the optical processes in the complex materials. A proper physical theory is required, as the band theory made remarkable progress in the solid-state physics by employing the Bloch theorem that greatly simplifies the many-body problem [57]. We need to describe the optical processes in the complicated molecular systems with a simple manner of physics, depending on the hierarchical complexity of matter as Anderson claimed “More is different” [58].

Optical processes in such a many-eigenstate system are usually studied by

focusing on a small subset of eigenstates (*system*), and the remaining part is regarded as *bath* [59]. This is the *system-bath reduced picture*, which is a very important physical concept used through this dissertation. The eigenstates included in the system can be arbitrarily chosen, but they should be small such as a single molecule, or a molecule plus its nearest surroundings. In practice, this selection depends on what physical phenomena we are focusing on. Let us consider again coherent optical processes in the photosynthetic light-harvesting complexes. In Section 1.1.2, we mentioned that coherent energy transfer, between the effectively assembled pigments, occurs in the protein environment that possibly protects the excitonic coherence between the pigments. The energy transfer is, in principle, a physical process that occurs between two molecules, *i.e.* donor and acceptor, and so it can be considered as the system in *system-bath reduced picture*. It should be noted that the concept of "donor and acceptor" is very useful in explaining the energy-transfer process, even in which the separation between donor and acceptor is not true in a strict sense, such as a case of generalized Förster theory [17]. This system of correlated two molecules can be studied without suffering from uncertainty coming from the presence of many eigenstates as stated above. We will show one possible demonstration of physical description of the optical response in such a supramolecular assembly where several π-conjugated molecules are strongly correlated in Chapter 5.

The thermal effect of protein to the energy transfer can be considered as a bath contribution to the system.[¶] The dynamics of the bath involves infinitely large number of degrees of freedom, therefore it should be treated by a different manner of physics. A very successful physical theory that can be applied to such a many-eigenstate problem is statistical physics [60, 61]. In this theory, we project complicated microscopic motions of chromophores to a small number of macroscopic variables. Therefore, the effects of the bath part to the system's optical response can be obtained as the ensemble average of optical polarization. This means that the information on the effects of the bath part always affords uncertainty of probability that comes from the stochastic approach. Nevertheless, by using the manner of statistical physics, we are able to describe the system's optical response correctly. Since the effect of protein to the energy transfer in the light-harvesting complexes are very important, we need a proper physical explanation for the bath contribution to the optical response of the system.

1.3 Outline and goal of this doctoral work

1.3.1 Outline of this dissertation

The present dissertation is organized as follows: Chapter 1 has described the introduction and motivation of the present doctoral work. We have claimed the usefulness of π-conjugated systems for the study of light-matter interactions.

[¶]The electrostatic effect of protein is very important. This can be, in principle, treated in the same theoretical frame of the above correlated molecules. The effect of several protein molecules to the correlated pigment molecules are estimated in this case.

In Chapter 2 we will describe the macroscopic optical polarization in terms of quantum mechanics. Specifically Section 2.1 introduces basic protocols of calculating the polarization on the basis of time-dependent perturbation theory. We will discuss not only the linear optical polarization but also the NLO polarization because NLO spectroscopy conveys rich information on the light-matter interactions in comparison with linear spectroscopy. Indeed various NLO spectroscopic techniques have been used in the present doctoral work. Section 2.2 treats a relaxation of quantum states. In the *system-bath reduced picture*, we are able to treat the system's optical response quantum mechanically. We will show that the environmental contributions can be incorporated into the system as relaxations of the system's eigenstates, namely *depopulation* and *decoherence*. Section 2.3 will provide one possible demonstration of incorporating the bath (environmental) contributions into the time-dependent perturbation theory in a semiclassical way. Specifically we use a multimode Brownian oscillator model under Franck-Condon approximation. The multimode Brownian oscillator model can potentially describe the environmental contributions from static limit to the fast modulation limit in a unified fashion. In Section 2.4 we will introduce the oriented-gas model that is very effective in describing the optical response of molecular crystals, in which intermolecular interactions can be neglected. The oriented-gas model will be combined with a supramolecular approach in order to predict the crystalline NLO polarization where supramolecules are formed by significant intermolecular interactions in Chapter 5.

Chapter 3 describes the dependence of the ultrafast optical response on the number of π-conjugated C=C double bonds (n). This chapter will provide the systematic understanding on how the size of π-electron delocalization affects the electronic population relaxation dynamics and the vibrational decoherence dynamics. We show ultrafast transient grating (TG) responses of β-carotene homologues of n = 9–15. It is shown that the dephasing time of the C-C stretching mode strongly depends on n, whereas that of the C=C stretching does not. The ultrafast TG responses of the β-carotene homologues are satisfactorily simulated by using the time-dependent perturbation theory. These theoretical predictions of the time-domain NLO signals will facilitate the understanding on frequency-domain NLO signals that will be calculated in the next chapter. This is because the frequency NLO signals are obtained by time-ordered half-Fourier transformation of the time-domain signals.

Chapter 4 shows the dependence of the third-harmonic generation (THG) response on n. By using the β-carotene homologues, we will show that the optical nonlinearity for the THG process is greatly enhanced with increasing the size of π-electron delocalization. Their frequency-domain THG responses are simulated very well by using the time-dependent perturbation theory, as well as the time-domain TG responses discussed in Chapter 3. Chapters 3 and 4 clarify how the third-order NLO responses are affected, as the size of π-electron delocalization increases. We show that the third-order NLO responses of any lengths of these carotenoids can be satisfactorily described with a unified manner of a time-dependent perturbation theory, where environmental contributions to the system's

optical response are properly incorporated through a Brownian oscillator model. We believe that this theoretical framework can also potentially describe the protein environmental contributions to the pigment molecules in the biological systems.

In Chapter 5, we try to clarify the relation between the supramolecular state that comprises several π-conjugated molecules and the second-order optical nonlinearity. Specifically we will focus on a supramolecular assembly of *N*-benzyl 2-methyl-4-nitroaniline (BNA) molecules, which are formed in a BNA crystal by intermolecular interactions. This supramolecular cluster show multi-fold increase of the optical nonlinearity relative to that of a corresponding set of the isolated molecules, in which the intermolecular interactions are ignored. It demonstrates how the optical response of the π-conjugated molecules is changed, when several π-conjugated molecules are correlated by the strong intermolecular interactions. We think that this study can provide good implications of the supramolecular state in the large optical nonlinearity of organic NLO crystals.

The conclusions of this dissertation is presented in Chapter 6.

1.3.2 The goal of this doctoral work

The goal of this doctoral work is to provide a unified explanation for light-matter interactions occurring in any types of complicated π-conjugated molecular systems. For this purpose, we apply NLO spectroscopy to artificial π-conjugated systems whose optical properties are substantially changed contingent upon the molecular structures, extent of π-electron delocalization, and correlations of molecules in their molecular assembly. The NLO spectroscopy conveys rich information on the light-matter interactions in comparison with linear spectroscopy, so that we expect to obtain much deeper insight into the optical response of the π-conjugated systems. The advantage of using the artificial π-conjugated systems is that their structures can be systematically changed, which facilitates the understanding of the intrinsic optical properties of π-conjugated systems. The author believes that the combination of the NLO spectroscopy and the artificial π-conjugated systems is the best choice to obtain the experimental data that is characteristic in all kinds of π-conjugated systems. Having such a well-planned experimental strategy, we are now ready to give an unified explanation for optical processes in any types of complicated π-conjugated molecular systems.

> *Lift up your eyes on high, and See who has created these things, ...*
> *The everlasting God, the LORD, The Creator of the ends of the earth.*
> *His understanding is unsearchable.*
>
> *Isaiah, 40:26, 28, Bible, New King James Version.*

Chapter 2

Physical theory of optical response

2.1 Nonlinear optical polarization

2.1.1 Optical polarization in density matrix formalism

The optical polarization, $P(\boldsymbol{r}, t)$, can be considered as the only material quantity that appears in the Maxwell equations because most of dielectric media have very small magnetic permeability compared with their electric susceptibility. Correct theoretical descriptions of the optical polarization allow us to understand all possible optical phenomena in principle. The Hamiltonian of the radiation-matter interactions, $H_{int}(\boldsymbol{r}, t)$, is semiclassically given by

$$H_{int}(\boldsymbol{r}, t) = -\int d\boldsymbol{r} E(\boldsymbol{r}, t) \cdot P(\boldsymbol{r}, t), \tag{2.1}$$

where $E(\boldsymbol{r}, t)$ is the classical transverse electric field. In general, the interaction with the electromagnetic field creates a complex spatial excitation profile in the matter, so that the integral in Eq. (2.1) is impossible to be calculated in practice. For simplicity, we will consider optical responses of a single particle whose size is much smaller than the wavelength in order to validate the dipole approximation. Hence Eq. (2.1) can be approximated to

$$H_{int}(\boldsymbol{r}, t) = -E(\boldsymbol{r}, t) \cdot V(\boldsymbol{r}, t), \tag{2.2}$$

where $V(\boldsymbol{r}, t)$ is the dipole operator. Accordingly, the optical polarization is naturally given by the expectation value of the dipole operator,

$$P(\boldsymbol{r}, t) = \mathrm{Tr}\Big[V\rho(E(\boldsymbol{r}, t), t)\Big]. \tag{2.3}$$

Here, $\rho(E(\boldsymbol{r}, t), t)$ is a time-dependent density operator of the system that depends on the external electric field $E(\boldsymbol{r}, t)$. In the interaction picture, the total Hamiltonian of the system (H_{T}) is given by $H_{\mathrm{T}} = H + H_{\mathrm{int}}$, where H is the Hamiltonian of the system in the thermal equilibrium. The temporal evolution of the density matrix is then described by the Liouville equation [50]:

$$\frac{d\rho}{dt} = -\frac{i}{\hbar}[H, \rho] - \frac{i}{\hbar}[H_{\mathrm{int}}(t), \rho]. \tag{2.4}$$

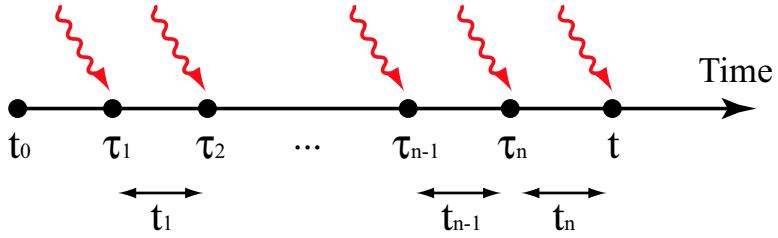

Figure 2.1: Time variables used in Eq. (2.7). The time proceeds from t_0 to t through n times photon interactions. The nth photon interaction occurs at time τ_n. $t_1, \cdots, t_n$ indicate time intervals between two photon interactions. The density matrix evolves during these time intervals, and we finally calculate the density matrix at time t.

It should be noted that Eq. (2.4) is sometimes called quantum Liouville equation or von Neumann's equation [50, 60]. By employing Liouville space notation (see Appendix A.1), we have

$$\frac{d\rho}{dt} = -\frac{i}{\hbar}\mathscr{L}\rho - \frac{i}{\hbar}\mathscr{L}_{\rm int}(t)\rho. \tag{2.5}$$

Here $\mathscr{L}$, $\mathscr{L}_{\rm int}$, and $\mathscr{V}$ are Liouville space operators. Using an arbitrary Hilbert space operator, A, they are defined as $\mathscr{L}A = [H, A]$, $\mathscr{L}_{\rm int}A = [H_{\rm int}, A]$, and $\mathscr{V}A = [V, A]$, respectively.

As we see in Eq. (2.3), the time-dependent density operator is a function of $E(\boldsymbol{r}, t)$. It is now to be expanded in powers of the electric field, *i.e.*

$$\rho(t) = \rho^{(0)}(t) + \rho^{(1)}(E, t) + \rho^{(2)}(EE, t) + \cdots, \tag{2.6}$$

where $\rho^{(n)}(t)$ shows the nth-order term. Using the time-ordered expansion technique (see Appendix A.2), we obtain

$$\rho^{(n)}(t) = \left(\frac{i}{\hbar}\right)^n \int_0^\infty dt_n \int_0^\infty dt_{n-1} \cdots \int_0^\infty dt_1 \mathscr{G}(t_n)\mathscr{V}\mathscr{G}(t_{n-1})\mathscr{V}\cdots\mathscr{G}(t_1)\mathscr{V}\rho(-\infty)$$
$$\times E(\boldsymbol{r}, t - t_n)E(\boldsymbol{r}, t - t_n - t_{n-1})\cdots E(\boldsymbol{r}, t - t_n - t_{n-1}\cdots - t_n). \tag{2.7}$$

Here, t_n represents the time intervals between successive interactions as shown in Fig. 2.1 ($t_n > 0$), and

$$\mathscr{G}(t) \equiv \theta(t)\exp\left[-\frac{i}{\hbar}\mathscr{L}t\right] \tag{2.8}$$

is the Liouville space Green function for the system after the photon interaction. $\theta(t)$ is the Heaviside step function, and $\rho(-\infty)$ means that the system was in the thermal equilibrium before the photon interactions (or infinitely past time).

Employing the Liouville-space notation where the double bracket means ensemble average in the Liouville space, Eq. (2.3) can read

$$P(\boldsymbol{r}, t) = {\rm Tr}[{\rm V}\rho({\rm t})] = \langle\langle {\rm V}|\rho({\rm t})\rangle\rangle. \tag{2.9}$$

By expanding the polarization in powers of the electric field, Eq. (2.9) can be recast as

$$P(\boldsymbol{r},t) = P^{(1)}(\boldsymbol{r},t) + P^{(2)}(\boldsymbol{r},t) + P^{(3)}(\boldsymbol{r},t) + \cdots , \tag{2.10}$$

with

$$P^{(n)}(\boldsymbol{r},t) = \langle\langle V|\rho^{(n)}(t)\rangle\rangle. \tag{2.11}$$

The nth-order nonlinear optical (NLO) polarization, $P^{(n)}(\boldsymbol{r},t)$, is finally given by

$$\begin{aligned} P^{(n)}(\boldsymbol{r},t) = \int_0^\infty dt_n \int_0^\infty dt_{n-1} \cdots \int_0^\infty dt_1 S^{(n)}(t_n, t_{n-1}, \ldots, t_1) \\ \times E(\boldsymbol{r}, t-t_n)E(\boldsymbol{r}, t-t_n-t_{n-1}) \cdots E(\boldsymbol{r}, t-t_n-t_{n-1}\cdots-t_1), \end{aligned} \tag{2.12}$$

with

$$S^{(n)}(t_n, t_{n-1}, \ldots, t_1) \equiv \left(\frac{i}{\hbar}\right)^n \langle\langle V|\mathscr{G}(t_n)\mathscr{V}\mathscr{G}(t_{n-1})\mathscr{V}\cdots\mathscr{G}(t_1)\mathscr{V}|\rho(-\infty)\rangle\rangle. \tag{2.13}$$

$S^{(n)}(t_n, t_{n-1}, \ldots, t_1)$ in Eq. (2.13) is nth-order NLO response function that contains all the information necessary for the calculation of the nth-order NLO process. Thus the optical polarization dynamics can be known from the time-domain response functions. It should be noted that any frequency-domain optical spectra can be derived as time-ordered half-Fourier transformations of the response functions. A linear optical absorption spectrum, $\mathrm{Im}[\chi^{(1)}(-\omega;\omega)]$, and a THG $\chi^{(3)}$ spectrum, $[\chi^{(3)}(-3\omega;\omega,\omega,\omega)]$, will be calculated in this dissertation. The details of the calculations of these frequency spectra will be discussed in the later chapters. We emphasize that the Liouville-space notation is much more useful for developing the theoretical formulation of optical dynamics compared to the Hilbert-space notation. On the other hand, the Hilbert-space notation facilitates the actual calculations in comparison with the Liouville-space notation. Therefore one usually formulate a theory in the Liouville space and then switches the expression from the Liouville space to the Hilbert space. The Hilbert-space expression of Eq. (2.13) is given by

$$\begin{aligned} S^{(n)}(t_n,t_{n-1},\ldots,t_1) = \left(\frac{i}{\hbar}\right)^n \theta(t_1)\theta(t_2)\cdots\theta(t_n) \\ \times\langle[[[\cdots[V(t_n+\cdots t_1), V(t_{n-1}+\cdots t_1)]\cdots], V(t_1)], V(0)]\rho(-\infty)\rangle. \end{aligned} \tag{2.14}$$

2.1.2 Response functions and Liouville-space pathways

Here we will present an eigenstate representation of the response function of Eq. (2.13). The eigenstate representation provides a clear insight into the significance of Liouville-space pathways. More conveniently, these pathways always have their corresponding double-sided Feynman diagrams, which reduces the complexity of theoretical derivations of the response functions to a great extent. Obviously the ensemble average taken in the response functions cannot be completely calculated because of the presence of the infinitely large number of

eigenstates. Nonetheless, optical processes in condensed phases are usually studied by focusing on a small subset of eigenstates, and the remaining part is treated semiclassically (see Section 2.2). For this reason, the eigenstate representation is still very important to interpret the physical processes of light-matter interactions even in case that there is a huge number of degrees of freedom in the system.

Linear response

The linear response function that governs all of linear optical phenomena is given by

$$S^{(1)}(t_1) = \frac{i}{\hbar}\langle\langle V|\mathscr{G}(t_1)\mathscr{V}|\rho(-\infty)\rangle\rangle, \tag{2.15a}$$

or

$$S^{(1)}(t_1) = \frac{i}{\hbar}\theta(t_1)\langle[V(t_1), V(0)]\rho(-\infty)\rangle. \tag{2.15b}$$

We thus obtain

$$S^{(1)}(t_1) = \frac{i}{\hbar}\theta(t_1)[J(t_1) - J^*(t_1)], \tag{2.16}$$

where

$$J(t_1) \equiv \langle V(t_1)V(0)\rho(-\infty)\rangle, \tag{2.17a}$$
$$J^*(t_1) \equiv \langle V(0)V(t_1)\rho(-\infty)\rangle. \tag{2.17b}$$

$J(t)$ and $J^*(t)$ have the corresponding Liouville-space pathways, respectively.

We will take an ensemble average that can be seen in Eq. (2.17a), in order to obtain the eigenstate representation of the linear response function, and hence

$$J(t) = \sum_{a,b} P(a)|\mu_{ab}|^2 I_{ab}(t). \tag{2.18}$$

Here, $P(a)$ is the thermal population of the state $|a\rangle$. $I_{ab}(t)$ describes the propagation of the state of the density matrix after the photon interaction, which is defined by

$$\mathscr{G}(t) = \theta(t)\sum_{\nu,\nu'} |\nu\nu'\rangle\rangle I_{\nu\nu'}(t)\langle\langle\nu\nu'|. \tag{2.19}$$

Under the fast modulation limit (homogeneous broadening), for example, $I_{\nu\nu'}(t)$ is given by

$$I_{\nu\nu'} = \theta(t)\exp(-i\omega_{\nu\nu'}t - \Gamma_{\nu\nu'}t). \tag{2.20}$$

It should be noted that the suffices a and b in Eq. (2.18) take all possible quantum states of the *system*. The double-sided Feynman diagrams of these pathways are shown in Fig. 2.2 (a).

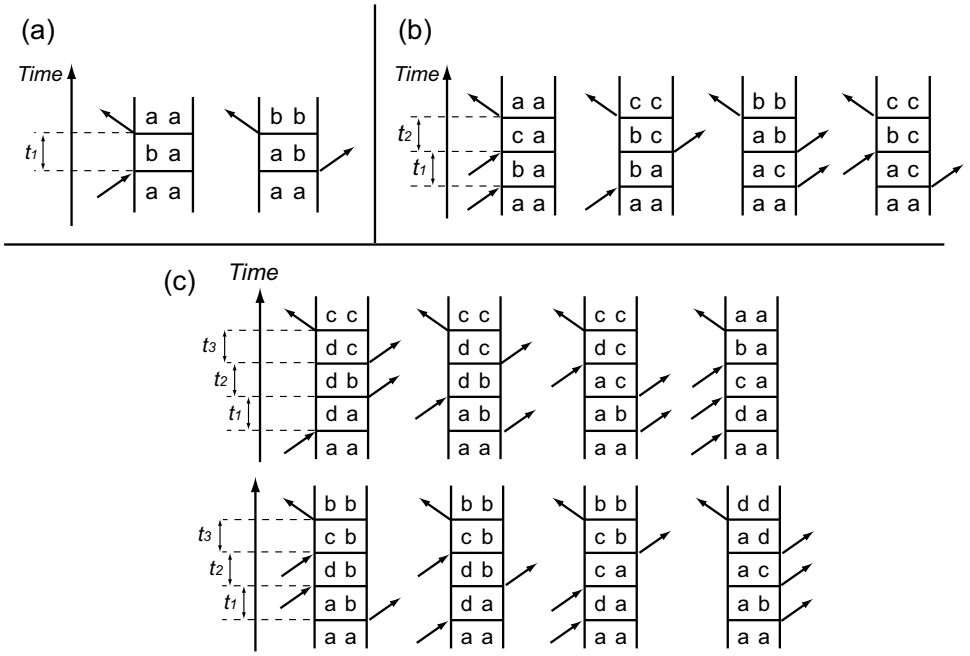

Figure 2.2: The double-sided Feynman diagrams of (a) linear response functions, (b) quadratic response functions, and (c) cubic response functions. Half of the response functions are complex conjugate of the remaining response functions. The final output wave vector $\boldsymbol{k}$ is given by sum of wave vectors of input photons ($\boldsymbol{k} = \sum_i \boldsymbol{k_i}$). Explicitly, $\boldsymbol{k} = \boldsymbol{k_1}$ for linear response, $\boldsymbol{k} = \boldsymbol{k_1} + \boldsymbol{k_2}$ for quadratic response, and $\boldsymbol{k} = \boldsymbol{k_1} + \boldsymbol{k_2} + \boldsymbol{k_3}$ for cubic response.

Second-order response

Analogous to the linear response function, the second-order response function is given by

$$S^{(2)}(t_2, t_1) = \left(\frac{i}{\hbar}\right)^2 \langle\langle V|\mathscr{G}(t_2)\mathscr{V}\mathscr{G}(t_1)\mathscr{V}|\rho(-\infty)\rangle\rangle. \tag{2.21}$$

We also get

$$S^{(2)}(t_2, t_1) = \left(\frac{i}{\hbar}\right)^2 \theta(t_1)\theta(t_2) \sum_{\alpha=1}^{2} [Q_\alpha(t_2, t_1) - Q_\alpha^*(t_2, t_1)], \tag{2.22}$$

where

$$\begin{cases} Q_1(t_2, t_1) = \sum_{a,b,c} P(a)\mu_{ac}\mu_{cb}\mu_{ba}I_{ca}(t_2)I_{ba}(t_1), \\ Q_2(t_2, t_1) = -\sum_{a,b,c} P(a)\mu_{ac}\mu_{cb}\mu_{ba}I_{bc}(t_2)I_{ba}(t_1). \end{cases} \tag{2.23}$$

Third-order response

The third-order response function is given by

$$S^{(3)}(t_3, t_2, t_1) = \left(\frac{i}{\hbar}\right)^3 \langle\langle V|\mathscr{G}(t_3)\mathscr{V}\mathscr{G}(t_2)\mathscr{V}\mathscr{G}(t_1)\mathscr{V}|\rho(-\infty)\rangle\rangle. \tag{2.24}$$

We also get

$$S^{(3)}(t_3,t_2,t_1) = \left(\frac{i}{\hbar}\right)^3 \theta(t_1)\theta(t_2)\theta(t_2) \sum_{\alpha=1}^{4} [R_\alpha(t_3,t_2,t_1) - R_\alpha^*(t_3,t_2,t_1)], \tag{2.25}$$

where

$$\begin{cases} R_1(t_3,t_2,t_1) &= \sum_{a,b,c,d} P(a)\mu_{ab}\mu_{bc}\mu_{cd}\mu_{da} I_{dc}(t_3) I_{db}(t_2) I_{da}(t_1), \\ R_2(t_3,t_2,t_1) &= \sum_{a,b,c,d} P(a)\mu_{ab}\mu_{bc}\mu_{cd}\mu_{da} I_{dc}(t_3) I_{db}(t_2) I_{ab}(t_1), \\ R_3(t_3,t_2,t_1) &= \sum_{a,b,c,d} P(a)\mu_{ab}\mu_{bc}\mu_{cd}\mu_{da} I_{dc}(t_3) I_{ac}(t_2) I_{ab}(t_1), \\ R_4(t_3,t_2,t_1) &= \sum_{a,b,c,d} P(a)\mu_{ab}\mu_{bc}\mu_{cd}\mu_{da} I_{ba}(t_3) I_{ca}(t_2) I_{da}(t_1). \end{cases} \tag{2.26}$$

2.2 Relaxation of quantum states

2.2.1 System-bath reduced picture

In Eqs. (2.18), (2.23), and (2.26), the summation is taken over all of the possible eigenstates in the total system. This is obviously impossible in almost of all practical cases, *e.g.* chromophores in a condensed phase, in which we have to consider huge number of eigenstates. Optical processes in condensed phases are usually studied by focusing on a small subset of eigenstates (*system*), and the remaining part is regarded as *bath*. The eigenstates included in the system can be arbitrarily chosen, but they should be small such as a single molecule, or a molecule plus its nearest surroundings. This is the *system-bath reduced picture*. In this picture, the Hamiltonian of the total system (H_T) can be separated into two parts,

$$H_T = H_S(\boldsymbol{q_S}) + H_B(\boldsymbol{q_B}) + H'(\boldsymbol{q_S}, \boldsymbol{q_B}). \tag{2.27}$$

H_S, H_B and H' are Hamiltonians of the system, bath, and system-bath interactions, respectively. $\boldsymbol{q_S}$ and $\boldsymbol{q_B}$ are the coordinates of the system and bath, respectively.

We will now calculate the expectation value of the system's operator, $A(\boldsymbol{q_S})$, as

$$\langle A(\boldsymbol{q_S})\rangle = \mathrm{Tr}[\rho(t)A(\boldsymbol{q_S})], \tag{2.28}$$

where $\rho(t)$ is the density matrix operator of the total system. Supposing that eigenstates of the system and bath are respectively denoted a, b and α, β, Eq. (2.28) can be expanded as follows:

$$\mathrm{Tr}[\rho(t)A(\boldsymbol{q_S})] = \sum_{a,b,\alpha,\beta} \langle a\alpha|\rho(t)|b\beta\rangle\langle b\beta|A(\boldsymbol{q_S})|a\alpha\rangle. \tag{2.29}$$

Since the operator $A(\boldsymbol{q_S})$ does not depend on the bath degrees of freedom, its matrix elements can be factorized as

$$\langle b\beta|A(\boldsymbol{q_S})|a\alpha\rangle = \langle b|A|a\rangle\langle\beta|\alpha\rangle. \tag{2.30}$$

The first matrix element and the second element are calculated in the system's subspace and in the bath's subspace, respectively. By using $\langle\beta|\alpha\rangle = \delta_{\alpha\beta}$, we obtain

$$\langle A(\boldsymbol{q_S})\rangle = \sum_{a,b,\alpha} \langle a\alpha|\rho(t)|b\alpha\rangle\langle b|A(\boldsymbol{q_S})|a\rangle. \tag{2.31}$$

With the definition of reduced density matrix operator of the system,

$$\sigma_{ab}(t) \equiv \sum_{\alpha} \langle a\alpha|\rho(t)|b\alpha\rangle = \mathrm{Tr_B}\langle a|\rho(t)|b\rangle, \tag{2.32}$$

we then have

$$\langle A(\boldsymbol{q_S})\rangle = \mathrm{Tr_S}[\sigma(t)A(\boldsymbol{q_S})]. \tag{2.33}$$

Here $\mathrm{Tr_S}$ and $\mathrm{Tr_B}$ are partial traces over the degrees of freedom of the system part and of the bath part, respectively. The reduced density operator, $\sigma(t)$, still obeys the Liouville equation. Therefore we are ready to discuss the macroscopic polarization in terms of only the system's eigenstates, even under the effect of the system-bath interactions. It should be emphasized that the effect of the system-bath interactions, $H'(\boldsymbol{q_S}, \boldsymbol{q_B})$, results in relaxations of the system's eigenstate. In the next, we will simply discuss the system-bath interactions by incorporating the relaxations into the system in a phenomenological way. The details of the rigid theoretical treatment, in which the relaxations are derived from $H'(\boldsymbol{q_S}, \boldsymbol{q_B})$, are beyond the scope of the present dissertation. The interested reader may refer to other literatures [50, 61].

2.2.2 System-bath interactions and relaxation

Under the effects of the system-bath interactions, the wave function of the system evolves into a superposition of quantum states. This superposition will soon get into quantum mixture because of the large number of degrees of freedom in the bath part. Thus the quantum nature of the system rapidly fade out. This is decoherence. By studying decoherence nature we are able to obtain rich information on the excited state dynamics because decoherence is a result of the bath interactions to the excited state of the system. In this section, we will clarify how relaxation is treated in the framework of quantum mechanics.

We expand the wavefunction of the total system, $\Psi(t)$, by using a complete set of the system's wavefunction, $\phi_n^S(t)$ [59]:

$$\Psi(t) = \sum_n c_n(t)\phi_n^S(t)\phi_n^B(t), \tag{2.34}$$

where $c_n(t)$ and $\phi_n^B(t)$ are the expansion coefficient and initial state of the bath, respectively. It should be noted that $\phi_n^B(t)$ is not a wavefunction of the eigenstate of the bath. Using Eq. (2.34), the expectation value of the operator $A(\boldsymbol{q_S})$ is given by

$$\langle A(t)\rangle = \langle\Psi(t)|A|\Psi(t)\rangle = \sum_{n,m} c_n(t)c_m^*(t)A_{nm}\langle\phi_m^B(t)|\phi_n^B(t)\rangle, \tag{2.35}$$

where $A_{nm} = \langle \phi_m^S(t)|A|\phi_n^S(t)\rangle$. The important point of Eq. (2.35) is that the expectation value of the total system are divided into the system part, $c_n(t)c_m^*(t)A_{nm}$, and the bath part, $\langle \phi_m^B(t)|\phi_n^B(t)\rangle$. In this way we can discuss the relaxations of the system and bath, independently.

Under the system-bath interactions, time-dependent values in the right-hand side of Eq. (2.35) should be decayed. Supposing that the state $|n\rangle$ decays in an exponential way with a rate constant of γ_n,

$$|c_n(t)|^2 = |c_n(0)|^2 e^{-\gamma_n t} \tag{2.36}$$

is obtained, since the relaxation of the quantum state is a decay of the probability of the quantum state. Hence the probability amplitude must vary in time as [62]

$$c_n(t) = c_n(0)e^{-i\omega_n t}e^{-\gamma_n t/2}. \tag{2.37}$$

On the other hand, $\langle \phi_m^B(t)|\phi_n^B(t)\rangle$ gradually vanishes, as well as $c_n(t)$. It can be written as

$$\langle \phi_m^B(t)|\phi_n^B(t)\rangle \to \langle \phi_m^B(0)|\phi_n^B(0)\rangle \exp(-\Gamma_{nm}t) = \exp(-\Gamma_{nm}t), \quad n \neq m. \tag{2.38}$$

Here we assume that the bath wavefunctions initially coincide with each other, hence $\langle \phi_m^B(0)|\phi_n^B(0)\rangle = 1$. The relaxation of the bath part in the case of $n = m$ does not have to be considered because we have already incorporated this contribution to the population relaxation, $e^{-\gamma_n t/2}$. This apparent inconsistency directly comes from the fact that we have introduced population relaxation of the quantum state $|n\rangle$ in the phenomenological way. In order to throughly understand the nature of the relaxation, we have to begin with the rigid theoretical treatment of the relaxation, in which the relaxation is derived from the unique system-bath interaction Hamiltonian, $H'(\boldsymbol{q_S}, \boldsymbol{q_B})$, as discussed in Refs. [50, 61]. Hence, Eq. (2.35) can be finally recast as

$$\langle A(t)\rangle = \sum_{n,m} c_n(t)c_m^* e^{-i\omega_{nm}t}(t)e^{-(\gamma_n+\gamma_m)t/2}A_{nm}\langle \phi_m^B(t)|\phi_n^B(t)\rangle \exp(-\Gamma_{nm}t), \tag{2.39}$$

with

$$\begin{cases} \exp(-\gamma_n t), & n = m, \\ \exp[-(\gamma_n + \gamma_m)t/2 - \Gamma_{nm}t], & n \neq m. \end{cases} \tag{2.40}$$

This equation shows population relaxation of the state $|n\rangle$ when $n = m$, while it shows the decoherence between the state $|n\rangle$ and $|m\rangle$ when $n \neq m$. The rate constant of this decoherence is called total dephasing rate. The total dephasing rate consists of population-induced dephasing rate, $(\gamma_n + \gamma_m)/2$, and pure dephasing rate, Γ_{nm}. The important point here is that decoherence contains information on the relaxation dynamics of the bath. In other words, we can investigate the environmental contributions to the chromophores by watching the decoherence dynamics.

2.3 Solvation dynamics of the optical response

2.3.1 Cumulant expansion and line-broadening function

In the system-bath reduced picture, we regard a subset of several electronic states as the system and the remaining part as the bath. The calculations of the system part of the response functions are not so difficult due to the small number of eigenstates involved, in contrast to the response functions of the bath part having infinitely large number of eigenstates. Here we shall provide a method that calculates the bath part in a semiclassical way. This method greatly simplifies the calculations of response functions.

We shall evaluate the response functions perturbatively using the cumulant expansion to second order. We begin with a linear response function, $J(t)$, of a two-level system, comprising a ground state $|g\rangle$ and excited state $|e\rangle$ [50]. Following Eq. (2.15a), it is given by

$$J(t_1) = \langle\langle V_{eg}|\mathscr{G}_{eg}(t_1)|V_{eg}\rho_g\rangle\rangle, \tag{2.41}$$

for $t_1 > 0$. We now introduce coherence Green function $\mathscr{G}_{nm}(t)$, which is defined by

$$\mathscr{G}_{nm}(t) \equiv \exp\left(-\frac{i}{\hbar}H_n t\right) A \exp\left(\frac{i}{\hbar}H_m t\right) \tag{2.42}$$

when $t > 0$. In view of practical use, it is more convenient to separate $J(t)$ into an electronic part and a vibronic part by using Franck-Condon approximation. In this case, the electronic part is regarded as the system, and the vibronic part is the bath. By using the above-defined coherence Green function and time-ordered expansion technique (see Appendix A.3 for the detail), Eq. (2.41) can be recast as

$$J(t_1) = \exp\left(-i\omega_{eg}t_1\right)\left\langle V_{ge}(t_1)\exp_+\left[-\frac{i}{\hbar}\int_{t_0}^{t_1} d\tau U(\tau)\right]V_{eg}\rho_g\right\rangle. \tag{2.43}$$

Here we have introduced a collective nuclear coordinate between $|g\rangle$ and $|e\rangle$, *i.e.* $U \equiv H_e - H_g - \hbar\omega_{eg}$ (see Fig. 2.3). It can be expressed as $U(\tau)$ in the Heisenberg picture with respect to the ground state dynamics, which is given by

$$U(\tau) = \exp\left(\frac{i}{\hbar}H_g\tau\right) U \exp\left(-\frac{i}{\hbar}H_g\tau\right). \tag{2.44}$$

Furthermore, $\exp_+[\cdots]$ in Eq. (2.43) is positive time-ordered exponential that is defined by

$$\begin{aligned}\exp_+&\left[-\frac{i}{\hbar}\int_{t_0}^{t_1} d\tau U(\tau)\right] \\ &\equiv 1 + \sum_{n=1}^{\infty}\left(-\frac{i}{\hbar}\right)^n \int_{t_0}^{t} d\tau_n \int_{t_0}^{\tau_n} d\tau_{n-1}\cdots\int_{t_0}^{\tau_2} d\tau_1 U(\tau_n)U(\tau_{n-1})\cdots U(\tau_1).\end{aligned} \tag{2.45}$$

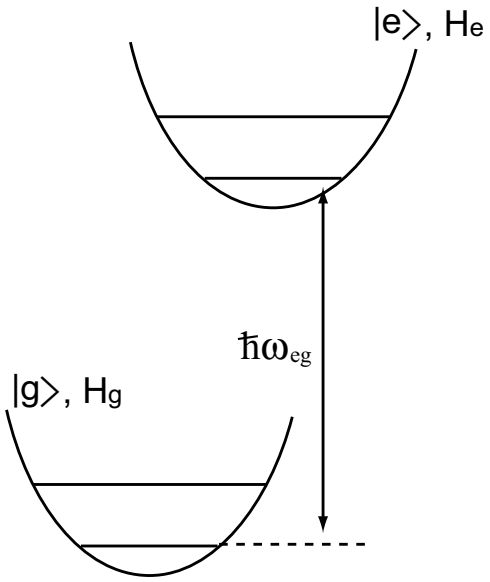

Figure 2.3: A simple two-level system comprises the ground state $|g\rangle$ and the excited state $|e\rangle$. The two states have their respective Hamiltonians, H_g and H_e. The energy between these two states is $\hbar\omega$. U can be defined as the difference of these two potential energy surfaces, $U \equiv H_e - H_g - \hbar\omega$.

The dipole interaction operator gives a transition dipole moment between $|g\rangle$ and $|e\rangle$ states, *i.e.* $V_{eg} = V_{ge} = |\mu_{eg}|$, so that Eq. (2.43) can be further recast as

$$J(t_1) = |\mu_{eg}|^2 \exp(-i\omega_{eg}t_1)\left\langle \exp_+\left[-\frac{i}{\hbar}\int_{t_0}^{t_1} d\tau U(\tau)\right]\rho_g\right\rangle. \tag{2.46}$$

Now the problem is to evaluate $\langle\cdots\rangle$ of Eq. (2.46). To obtain the ensemble average, we use cumulant expansion [50, 63], which is given by

$$\ln\left\langle e^X\right\rangle = \sum_{N=1}^{\infty}\frac{1}{N!}\langle X^N\rangle \equiv \langle e^X - 1\rangle_c. \tag{2.47}$$

Here we have assumed that X is a random variable, and $\langle X\rangle_c$ indicates the corresponding cumulant average of the usual expectation value, $\langle X\rangle$. From Eq. (2.46), we have

$$\ln\langle|\mu_{eg}|^{-2}J(t_1)\exp(i\omega_{eg}t_1)\rangle = \left\langle \exp_+\left[-\frac{i}{\hbar}\int_{t_0}^{t_1} d\tau U(\tau)\right]\rho_g - 1\right\rangle_c. \tag{2.48}$$

By using Eq. (2.45), the right-hand side of Eq. (2.48) can be recast as

$$-\frac{i}{\hbar}\int_0^{t_1} d\tau\langle U(\tau)\rho_g\rangle_c + \left(-\frac{i}{\hbar}\right)^2\int_0^{t_1} d\tau_2\int_0^{t_2} d\tau_1\langle U(\tau_2)U(\tau_1)\rho_g\rangle_c + \cdots. \tag{2.49}$$

Therefore the cumulant average of $\langle|\mu_{eg}|^{-2}J(t_1)\exp(i\omega_{eg}t_1)\rangle$ is obtained by truncating Eq. (2.49) at second order of U. In addition to this, $\int_0^{t_1} d\tau\langle U(\tau)\rho_g\rangle_c$ vanishes

when we take the ensemble average, *i.e.* $\int_0^{t_1} d\tau \langle U(\tau)\rho_g\rangle_c \sim 0$. Hence, we obtain

$$\ln \langle |\mu_{eg}|^{-2} J(t_1) \exp(i\omega_{eg} t_1)\rangle = \left(-\frac{i}{\hbar}\right)^2 \int_0^{t_1} d\tau_2 \int_0^{t_2} d\tau_1 \langle U(\tau_2)U(\tau_1)\rho_g\rangle_c. \tag{2.50}$$

It should be noted that the second-order cumulant, $\langle X^2\rangle_c$, corresponds to a variance, $\langle X^2\rangle - \langle X\rangle\langle X\rangle$ [63]. This means that the right-hand side of Eq. (2.50) shows fluctuations of the potential energy surface, U.

Equation (2.41) can finally be written as

$$J(t_1) = |\mu_{eg}|^2 \exp[-i\omega_{eg} t_1 - g(t_1)], \tag{2.51a}$$

with

$$g(t) \equiv \int_0^t d\tau_2 \int_0^{\tau_2} d\tau_1 C(\tau_1), \tag{2.51b}$$

and

$$C(\tau_1) \equiv \frac{1}{\hbar^2}\langle U(\tau_1)U(0)\rho_g\rangle_c. \tag{2.51c}$$

Here we have changed $\langle U(\tau_2)U(\tau_1)\rho_g\rangle_c$ in Eq. (2.50) to $\langle U(\tau_1)U(0)\rho_g\rangle_c$, since $U(\tau)$ is assumed to be stationary [61]. The function $g(t)$ is a line-broadening function that expresses a time evolution of the vibronic contribution to the electronic excitation. In other words, it determines a spectral shape of linear optical absorption.

2.3.2 Line-broadening function and spectral density

The response function has been now expressed in terms of the line-broadening function. The main point of using the line-broadening function is to provide a semiclassical procedure that evaluates the necessary correlation functions without calculating the nuclear eigenstates explicitly. Here we will describe the frequency-domain expression of the line-broadening function, *spectral density*. The spectral density dramatically reduces the amount of the work for the evaluation of the line-broadening function.

The two-time correlation function, $C(t)$ in Eq. (2.51c), can be expressed in frequency domain as

$$\tilde{C}(\omega) = \int_{-\infty}^{\infty} dt \exp(i\omega t) C(t), \tag{2.52a}$$

with

$$\tilde{C}(\omega) = \tilde{C}'(\omega) + i\tilde{C}''(\omega). \tag{2.52b}$$

Using the detailed balance condition in the fluctuation-dissipation theorem [50, 61], we have

$$\tilde{C}(-\omega) = \exp(-\beta\hbar\omega/2)\tilde{C}(\omega), \tag{2.53}$$

where $\beta = (k_B T)^{-1}$, k_B is the Boltzmann constant, and T is the temperature. We then obtain

$$C(t) = \int_{-\infty}^{\infty} d\omega \tilde{C}''(\omega) \cos\omega t \coth(\beta\hbar\omega/2) - i\int_{-\infty}^{\infty} d\omega \tilde{C}''(\omega)\sin\omega t. \tag{2.54}$$

The spectral density, $\rho(\omega)$, is defined by $\tilde{C}''(\omega)/\omega^2$ [64–68]. The line-broadening function $g(t)$ can be expressed in terms of $\rho(\omega)$ as

$$\begin{aligned} g(t) = &- \frac{(\Delta_{in}t)^2}{2} - \frac{i\lambda t}{\hbar} \\ &+ \int_0^\infty d\omega\rho(\omega)\coth\left(\frac{\beta\hbar\omega}{2}\right)(1-\cos\omega t) + i\int_0^\infty d\omega\rho(\omega)\sin\omega t, \end{aligned} \tag{2.55}$$

where Δ_{in} is an inhomogeneous linewidth, and λ is the solvation reorganization energy :

$$\lambda = \hbar\int_0^\infty d\omega\ \omega\rho(\omega). \tag{2.56}$$

2.3.3 Multimode Brownian oscillator model

Until now we have not explicitly considered the solvent-chromophore interactions because there is no difference between molecular vibrations and the solvent-chromophore interactions, especially for photon. Therefore they can be regarded as the environmental contributions to optical transition, if their characteristic frequencies are much smaller ($\leq 10^{-1}$) than the energy of the electronic optical transition. These environmental contributions to the electronic optical transition can be described by the linearly displaced Brownian harmonic oscillator model [50, 61, 69], which is given by

$$H = \sum_n \left[\frac{p_n^2}{2m_n} + \frac{m_n\omega_n^2}{2}\left(x_n - \sum_j \frac{c_{nj}q_j}{m_n\omega_n^2}\right)^2\right]. \tag{2.57}$$

The Brownian oscillator model is able to describe any types of environmental contributions from inhomogeneous limit to homogeneous limit. In the inhomogeneous (static) limit, the spectral shape of the Brownian oscillator model shows a Gaussian profile. This has been already included in Eq. (2.55). In the homogeneous (fast modulation) limit, the Brownian oscillator model gives a Lorentzian profile. The important result of the Brownian oscillator model is a case of overdamped region where the oscillator's characteristic frequency is much smaller than its damping constant. This region is an intermediate between the inhomogeneous and homogeneous limit. In this case, the Brownian oscillator model gives a following expression for the spectral density [50, 68, 70]:

$$\rho_L(\omega) = \frac{2}{\pi\omega}\frac{\lambda_B\omega_B^2\gamma_B}{(\omega_B^2-\omega^2)^2+\omega^2\gamma_B^2}. \tag{2.58}$$

Here, λ_B, ω_B, and γ_B are the coupling strength, the central frequency, and the linewidth of the overdamped-Brownian oscillator, respectively. The rigorous derivation of Eq. (2.58) is quite complicated [71], so that we briefly review this model by using Langevin equation in this section.

The Langevin equation is given by

$$m_j\ddot{q}_j(t) + m_j\omega_j^2 q_j(t) + m_j \int_{-\infty}^{t} d\tau\gamma_j(t-\tau)\dot{q}_j(t) = f_j(t) + F_j(t). \tag{2.59}$$

Here $q_j(t)$, m_j, ω_j, $\gamma_j(t)$, f_j and F_j represent normal coordinate, mass, central frequency, time-dependent friction, Gaussian stochastic random force, and external driving force of jth harmonic oscillator, respectively. Noting that $\langle f_j(t)\rangle = 0$, it can be recast as

$$m_j\langle\ddot{q}_j(t)\rangle + m_j\omega_j^2\langle q_j(t)\rangle + m_j \int_{-\infty}^{t} d\tau\gamma_j(t-\tau)\langle\dot{q}_j(t)\rangle = F_j(t), \tag{2.60}$$

since $\langle q_j(t)\rangle$ also satisfies Eq. (2.59) because of the linearity of the Langevin equation. This equation can be solved by applying Fourier transformation to the both sides:

$$-m_j\omega^2\langle\tilde{q}_j(\omega)\rangle + m_j\omega_j^2\langle\tilde{q}_j(\omega)\rangle - im_j\omega\tilde{\gamma}_j(\omega) = \tilde{F}_j(\omega), \tag{2.61}$$

where $\tilde{F}_j(\omega)$ and $\langle\tilde{q}_j(\omega)\rangle$ are the Fourier transforms of $F_j(t)$ and $\langle q_j(t)\rangle$, respectively. $\tilde{\gamma}_j(\omega)$ is defined as

$$\tilde{\gamma}_j(\omega) \equiv \int_{-\infty}^{\infty} dt\, e^{i\omega t}\langle q_j(t)\rangle \int_{-\infty}^{t} d\tau\gamma_j(t-\tau). \tag{2.62}$$

Furthermore we have assumed $\langle q_j(t)\rangle \propto e^{i\omega_j t}$. By assuming that thermal motions of the bath are very fast compared with the oscillator motion, we set $\tilde{\gamma}_j(\omega) = \gamma_j$, independent of ω. Equation (2.60), hence, can be solved:

$$\langle\tilde{q}_j(\omega)\rangle = \alpha_j(\omega)\tilde{F}_j(\omega), \tag{2.63a}$$

with a linear susceptibility of the oscillator's bath part,

$$\alpha_j(\omega) = \frac{1}{m_j}\frac{1}{-\omega^2 + \omega_j^2 - i\omega\gamma_j}. \tag{2.63b}$$

By referring to the expression of the linear response function in Eqs. (2.16), (2.17), and (2.51), the linear susceptibility of the oscillator's bath part can be written as

$$\alpha_j(\omega) = \int_0^{\infty} dt\, e^{i\omega t}\left\langle -\frac{i}{\hbar}\Big[\langle q_j(t)q_j(0)\rho_g\rangle - \langle q_j(0)q_j(t)\rho_g\rangle\Big]\right\rangle. \tag{2.64}$$

It should be noted that the electronic energy gap is given by

$$U = \sum_j m_j\omega_j^2 d_j q_j. \tag{2.65}$$

Analogous to Eq. (2.52b), the time-domain two-time correlation function of jth Brownian oscillator, $C_j(t)$, can be separated into the real and imaginary parts:

$$C_j(t) = C_j'(t) + iC_j''(t), \tag{2.66a}$$

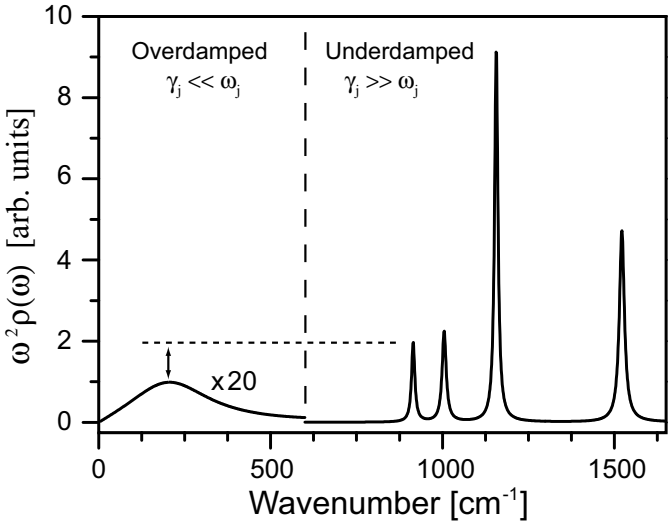

Figure 2.4: The spectral density of β-carotene in tetrahydrofran (THF) solvent. β-carotene has three high-frequency vibrational modes, at around 1000, 1150, and 1500 cm^{-1}, which are the in-plane methyl-rocking, central C-C stretching, and central C=C stretching modes, respectively. The mode at 912 cm^{-1} is a solvent mode.

where, in this case,

$$C_j'(t) \equiv \frac{1}{2\hbar^2}[\langle q_j(t)q_j(0)\rho_g\rangle + \langle q_j(0)q_j(t)\rho_g\rangle] \tag{2.66b}$$

and

$$C_j''(t) \equiv -\frac{i}{2\hbar^2}[\langle q_j(t)q_j(0)\rho_g\rangle - \langle q_j(0)q_j(t)\rho_g\rangle]. \tag{2.66c}$$

From Eq. (2.52), we have

$$\tilde{C}_j''(\omega) = 2\int_0^\infty dt \sin(\omega t) C_j''(t). \tag{2.67}$$

Comparing Eq. (2.64) and Eq. (2.67), the following relation is obtained:

$$\tilde{C}_j''(\omega) = -\frac{i}{2\hbar}[\alpha_j(\omega) - \alpha_j^*(\omega)] \tag{2.68}$$

with

$$\tilde{C}''(\omega) = \sum_j \left(\frac{m_j\omega_j^2 d_j}{\hbar}\right)\tilde{C}_j''(\omega). \tag{2.69}$$

Finally the mathematical expression of the above spectral density is given by

$$\rho(\omega) = \frac{\tilde{C}''(\omega)}{\omega^2} \propto \sum_j \frac{1}{\omega}\frac{\omega_j^2\gamma_j}{(\omega_j^2 - \omega^2)^2 + (\omega\gamma_j)^2}. \tag{2.70}$$

Now we are ready to simulate any time-domain and frequency-domain spectroscopic signals in a unified fashion. Figure 2.4 shows a spectral density of

β-carotene in tetrahydrofuran (THF) solvent, which is calculated based on the Brownian oscillator model. The spectral density shown in Fig. 2.4 is actually a combination of several underdamped Lorentzian modes and one overdamped mode expressed by Eq. (2.58). The detailed simulations of the spectroscopic signals will provide rich information on the chromophore's optical property and the chromophore-environment interactions.

2.4 Polarization in crystalline phase

In the last section, the macroscopic polarization was reduced to the microscopic polarization of the system that consists of a few electronic states. This method can be applied to chromophores in any isotropic media, including solvent and polymer matrix. On the other hand, we need to allow for anisotropy in the crystalline phase. The most famous method that describes the optical property of the molecular crystal is the oriented-gas model [72–74]. The oriented-gas model is an excellent model for the qualitative understanding of the mechanism that gives rise to the optical properties. It should be noted that the oriented-gas model failed to give a quantitative prediction of NLO susceptibilities in many cases [42–47]. These discrepancies are accounted for that π-electrons delocalize over several molecules, whereas the oriented-gas model assumes that π-electrons are localized within one molecule. Such π-electron delocalization is caused by the strong intermolecular interactions. This kind of problem will be discussed in Chapter 5. In this section, we briefly review the conventional oriented-gas model.

The oriented gas model has two theoretical assumptions. (1) the intermolecular interactions are sufficiently weak compared to the intramolecular interactions, therefore the intermolecular interactions can be ignored. (2) the overall crystal polarization is expressed as a geometrical sum of the individual polarization of molecules in the unit cell. Based on these assumptions, for example, the second-order NLO susceptibility is given by

$$d_{IJK} = \mathcal{N} f_I^{2\omega} f_J^{\omega} f_K^{\omega} b_{IJK}, \tag{2.71a}$$

where

$$d_{IJK} = \frac{1}{2}\chi^{(2)}_{IJK}(-2\omega;\omega,\omega), \tag{2.71b}$$

$$b_{IJK} = \frac{1}{n}\sum_{s=1}^{n} \cos[I, i(s)]\cos[J, j(s)]\cos[K, k(s)]\beta_{ijk}. \tag{2.71c}$$

Here I, J, K denote principal dielectric axes of crystal. f_I^{Ω}, $\mathcal{N}$, n, and β_{ijk} are local field correction factor of dielectric axis I at frequency Ω, number density, number of molecules in the unit cell, and a tensorial component of second molecular hyperpolarizability in the molecular coordinate (i, j, k). $\cos[I, i(s)]$ is a direction cosine that defines the orientation of the molecular axis i relative to the crystalline axis I. b_{IJK} is a tensorial component of quadratic nonlinearity of the unit cell per

molecule. The summation in Eq. (2.71a) is taken over all n molecules in the unit cell.

In case of two-dimensional molecules in crystal of $mm2$ (C_{2h}) point group symmetry, which we will use in Chapter 5, Eq. (2.71a) are expressed as

$$\begin{aligned} b_{ZZZ} &= \beta_{yyy}\cos^3\alpha, \\ b_{ZYY} &= -\beta_{xyy}\frac{(\sin 2\Phi \sin 2\alpha)}{2} + \beta_{yxx}\sin^2\Phi\cos\alpha + \beta_{yyy}\cos^2\Phi\cos\alpha\sin^2\alpha, \\ b_{ZXX} &= \beta_{xyy}\frac{(\sin 2\Phi \sin 2\alpha)}{2} + \beta_{yxx}\cos^2\Phi\cos\alpha + \beta_{yyy}\sin^2\Phi\cos\alpha\sin^2\alpha, \end{aligned} \quad (2.72a)$$

Here the definitions of the angles α and Φ are shown in Fig. 5.6 (see page 76). In this way, the macroscopic crystal polarization is reduced to the microscopic polarization of the unit cell. The optical response of the crystal is now to be described in the same framework used through this chapter.

It should be noted that the local field correction factor f_I^{Ω} in Eq. (2.71a) actually acts as environmental contributions to the system that consists of the eigenstates of the unit cell. If the local field correction factor is properly taken, the oriented-gas model gives the correct prediction. Nevertheless, the proper evaluation of the local field correction factor is a difficult task in reality. The supramolecular approach is one possible way that properly incorporates this environmental contribution to the oriented-gas model.

Chapter 3

Sub-20-fs time-resolved transient grating spectroscopic study of β-carotene homologues

3.1 Introduction

3.1.1 Coherent spectroscopy and excited-state dynamics

Carotenoids, together with bacteriochlorophylls (BChls), are involved in the ultrafast primary reactions of photosynthesis. Molecules of these two types of pigments are spatially arranged in proteins, forming a light-harvesting complex in purple bacteria (see Fig. 1.1 on page 4). In the light-harvesting complex, the light energy absorbed by carotenoids are transferred to BChls. This energy is then sequentially transferred to the adjacent BChl molecules in the complexes. These flows of energy transfer occur in the sub-ps ultrafast time regime. This integrated biological function is of great interest in the field of the recent ultrafast spectroscopy [16, 18–20, 75–79].

The energy relaxation and energy-transfer dynamics in the light-harvesting complexes have been usually studied by probing their excited-state population dynamics by using such techniques as pump-probe absorption spectroscopy [77, 80, 81] or femtosecond time-resolved Raman spectroscopy [77, 82–84]. These spectroscopic techniques are used to describe how energy flows in the system. Unfortunately in some cases (especially in case of carotenoids), the conclusions based upon these types of experiments strongly depend on the model used to interpret the data. For example, the transient spectrum has a complex feature and is difficult to be understood by clarifying which excited state has a major contribution. It will not be able to unequivocally determine the route that the excitation energy follows between the initial and final excited states. An alternative approach to study these complicated dynamics is required.

It is generally accepted that high-frequency molecular vibrations are deeply related to these population relaxation dynamics (the carotenoid-to-BChl energy

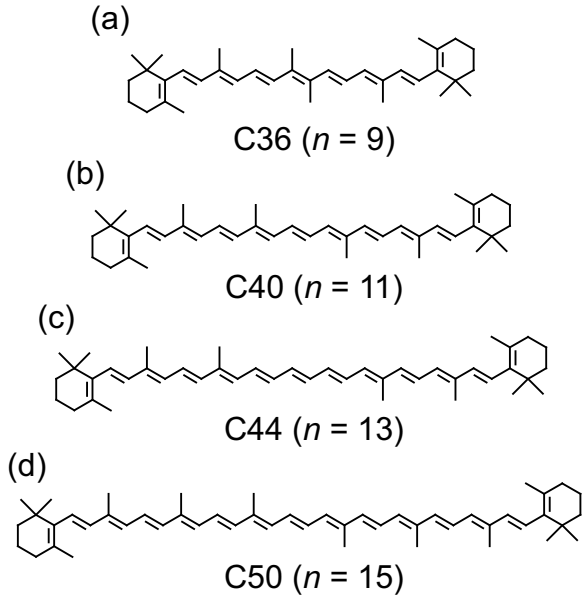

Figure 3.1: Chemical structures of the β-carotene homologues used in the present study. They are named after the number of constituent carbon atoms (a) C36, (b) C40 (β-carotene), (c) C44, and (d) C50. The conjugation length is denoted as n.

transfer and the internal conversion within carotenoids) [77, 85]. In fact, Herek *et al.* demonstrated that the efficiency of the energy transfer in the light-harvesting complex can be manipulated by controlling the superposition of high-frequency nuclear wavepackets of carotenoids with optimally shaped excitation pulses [3, 86]. This coherent control technique has been more recently used as a spectroscopic technique. Hauer *et al.* investigated the coherence dynamics of the carotenoid's excited states by using "coherent control spectroscopy" [87, 88]. The idea of coherent control spectroscopy is very interesting. In order to see the vibrational coherence dynamics of the excited state whose lifetime is too short to be directly measured, they investigate how the energy dissipation dynamics is affected by the initial state of the coherent nuclear wavepacket, which is artificially prepared by shaped excitation pulses. These coherent spectroscopic studies have a great impact on the current understanding of the carotenoid's photophysics [3, 86–90]. Therefore it is vitally important to investigate the coherence dynamics in carotenoids.

We have recently constructed an ultrashort-pulse-generation system that can produce sub-20-fs pulses across the whole visible wavelength region [70, 91]. These ultrashort excitation pulses generated coherent nuclear motions in β-carotene, so that the coherent oscillations were observed in the ordinary transient signals that simply come from the electronic population dynamics. In addition, we have successfully described the ultrafast optical responses of β-carotene in terms of time-dependent perturbation theory, together with a Brownian oscillator model. In this chapter, we extend this study by using a series of β-carotene homologues (Fig. 3.1) in order to investigate how the ultrafast optical response of carotenoids

depends on the extent of the π-conjugation length.

3.1.2 Carotenoid's classical excited state dynamics

The ultrafast excited-state dynamics of carotenoids have been extensively studied [77, 78]. Classically, carotenoid's excited singlet-states are described based on the theoretical formalism introduced by Tavan and Schulten [92, 93]. The ground state, S_0, is classified on the basis of the C_{2h} point symmetry group as the $1^1A_g^-$ state. The one-photon allowed transition goes from S_0 to S_2, which is designated as the $1^1B_u^+$ state. A lower excited singlet-state called S_1 also exists but can only be populated by a two-photon process from S_0. S_1 has been designated as the $2^1A_g^-$ state. After photoexcitation from S_0 to S_2, the population in S_2 rapidly decays into S_1, within a few hundreds femtoseconds [77, 94, 95]. The lifetime of S_1 varies from a few picoseconds to several nanoseconds depending on the number of conjugated C=C double bonds [77, 83, 94]. It should also be pointed out that additional singlet excited states lying between S_2 and S_1 have been proposed (a detailed discussion of these is beyond the scope of this present work [77, 79, 95–97]).

3.2 Experimental Procedures

3.2.1 Sub-20-fs pulse generation technique

A schematic diagram of our home-built noncollinear optical parametric amplifier (NOPA), which is used as a excitation light source of the subsequent measurement, is shown in Fig. 3.2 [70] (for other references, see Refs. [98–102]). Initially, a femtosecond Ti:sapphire regenerative amplifier (Spectra Physics, Hurricane) is used to generate 100 fs pulses at 780 nm at a 1 kHz repetition rate. Part of the beam from the amplifier (~400 μJ) is used for the NOPA system. This beam is then divided into two with a ratio of 9:1. The pump pulses for the parametric amplification are obtained by generating second harmonic pulses using a 400-μm-thick BBO crystal (Type I, $\theta = 29^\circ$). The residual of the fundamental laser beam is passed through a delay line for synchronization and then focused onto a 1-mm-thick sapphire plate in order to generate white-light continuum pulses by the self-phase modulation effect. This white-light continuum is used for the seed pulses to produce a stable output of the NOPA. This type of continuum is obtained by carefully adjusting the incident pulse energy so that it is only slightly higher than the threshold required for the white-light continuum generation. The stabilization of the intensity of the white-light continuum is the most important point for the stable output of the NOPA.

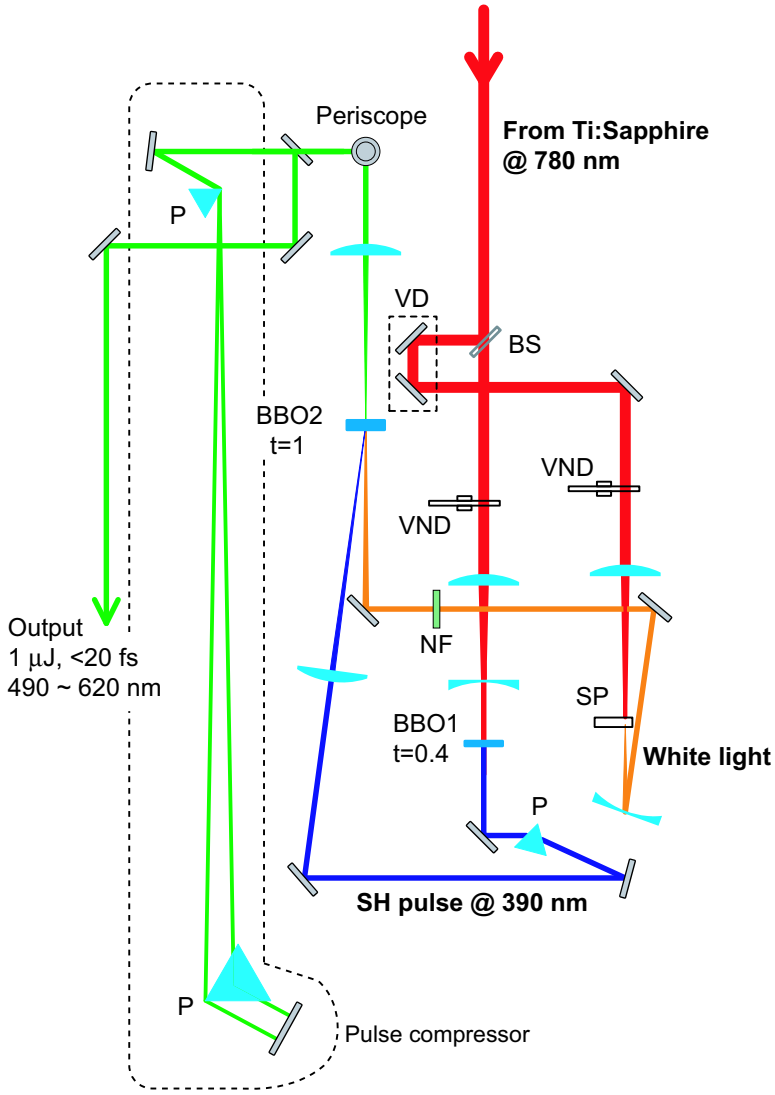

Figure 3.2: Schematic setup of the NOPA. BS: beam splitter, VD: variable optical delay line, VND: variable neutral density filter, P: prism, SP: sapphire plate, NF: notch filter.

In order to further stabilize the NOPA output, we suppressed part of the NOPA spectrum near the fundamental pump beam wavelength by placing a thin bandpass dielectric filter (notch filter) into the seed beam. Parametric gain is achieved in a single path through a 1-mm-thick BBO crystal, cut at $\theta = 31^\circ$ by using the type I phase matching. To minimize the self-focusing effect, the BBO crystal is positioned slightly beyond the focus of the pump beam. The amplified beam, having $\sim$1 μJ in power, is collimated by a spherical lens and then sent to a pulse compressor, made of a pair of Brewster-cut glass prisms. By adjusting the insertion of the Brewster prism, the pulse width was optimized. The SHG-intensity cross correlation measured between two of divided beams from the NOPA output was typically about 10–20 fs in the visible region (λ = 490–620 nm).

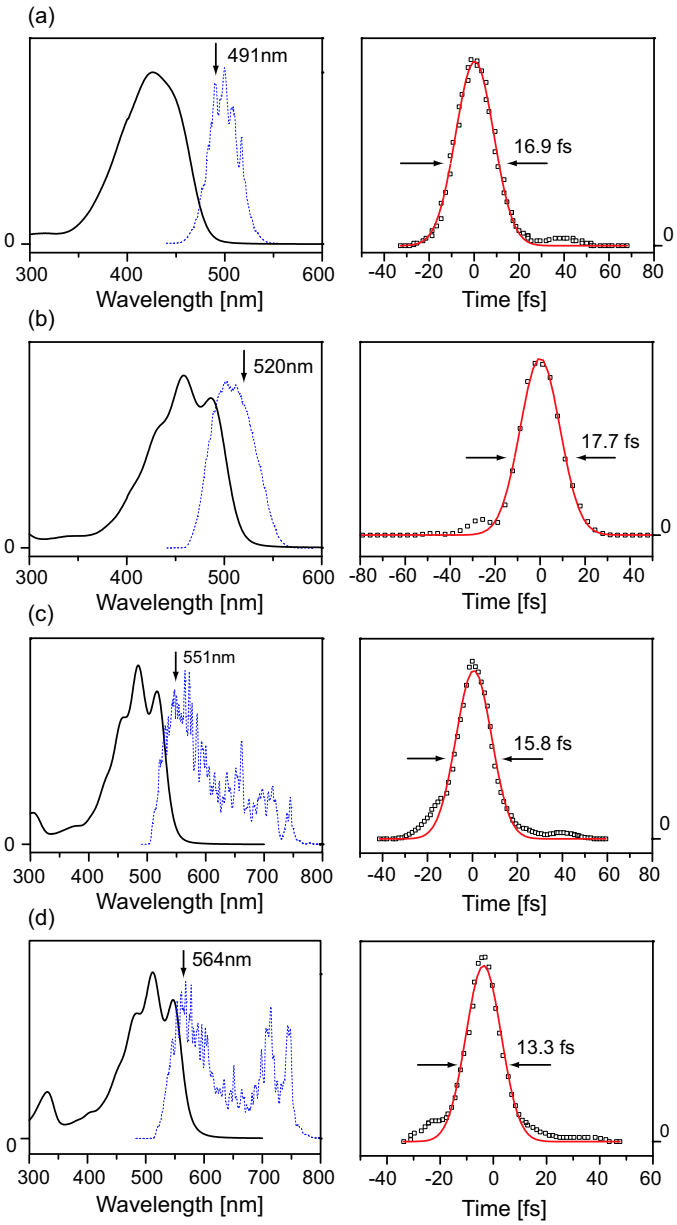

Figure 3.3: Spectrum of the excitation pulse (blue-dotted line, left-hand panel) and its SHG-intensity autocorrelation trace (open box: experimental data, red-solid line: gaussian fit, right-hand panel) used for the measurement of (a) C36, (b) C40, (c) C44, and (d) C50. The absorption spectrum (black-solid line, left-hand panel) is depicted in each graph and the detection wavelength is indicated with an arrow. The temporal bandwidth of the excitation pulse is shown in the left-hand panel with its half width at half maximum.

3.2.2 Transient grating measurements

The light from the NOPA were split into three beams, and they were used for the excitation pulses for the transient grating (TG) measurements in the folded boxcars geometry. The measured TG signals from β-carotene were independent

of the intensity of each pulse from 15 nJ to 170 nJ. The four-wave mixing beam, which was generated in the sample, was spatially selected using a mask, and then detected with a photomultiplier tube (Hamamatsu, R636-10) following dispersion through a monochromator (JASCO, HR10). The signal was filtered and amplified by using a lock-in technique.

β-carotene was commercially purchased from Wako and recrystallized once from a benzene solution. The other homologues were synthesized and purified as described in Ref. [103]. The UV-visible absorption spectra of the homologues in tetrahydrofuran (THF) were measured with a Jasco V-530 spectrophotometer at room temperature and no *cis*-peaks were observed. Also the ^{1}H-NMR spectra of all of the homologues were measured using a JEOL JNM-LA 400 Fourier Transform (FT)-NMR spectrometer and showed that they were all in the all-*trans* configuration.

The sample was dissolved in THF and flowed through a 100-μm-thick optical flow cell sandwiched between 1-mm-thick windows in order to prevent sample degradation. The sample concentrations were adjusted so that the optical densities were 1.0–1.4 at their absorption maxima. The time durations of the pulses were determined by a second harmonic generation (SHG) intensity autocorrelation technique using a 100-μm-thick β-BaB_2O_4 (BBO) crystal, where a 1-mm-thick glass plate was placed just in front of the BBO crystal to properly compensate the frequency chirp of the pulses imposed by the window of the flow cell.

The spectrum and the autocorrelation trace of the laser pulse used in the TG measurement of each homologue, together with its absorption spectrum, are shown in Fig. 3.3. The excitation and the detection wavelengths were the same. The time durations of all of the pulses used in the measurements were under 18 fs. The excitation pulses shown in Figs. 3.3(c) and (d) have non-negligible intensities on the longer wavelength side at around 700 nm. We have experimentally confirmed that the TG profiles do not depend on whether these off-resonance parts exist in the pulse spectra.

3.2.3 Resonance Raman measurements

Resonance Raman (RR) spectra were recorded with a Jobin Yvon U1000 spectrometer equipped with a liquid nitrogen cooled charge-coupled device camera (Spectrum One, Jobin Yvon). The spectral resolution (bandwidth) was less than 1 cm^{-1} at each excitation wavelength. The excitation was provided by Coherent Argon (Innova 100) and Krypton (Innova 90) lasers at approximately -1000 cm^{-1} from the 0-0 electronic transition and, where possible, under full resonance conditions in order to identify vibrational modes ascribed as overtones. The β-carotene/THF samples were sealed in oxygen depleted quartz cells and the solutions stirred during data acquisition. The RR spectra were recorded at 298 K with a 90-degree geometry. The laser power at the sample did not exceed 20 mW. At each excitation wavelength, no evolution of the RR signals were observed during data acquisition.

3.3 Results and Discussion

3.3.1 Transient grating measurements

Figure 3.4 shows the experimentally obtained TG signals. With every homologue, a sharp peak was observed at $t = 0$ (coherent spike), and the subsequent coherent oscillations were superimposed on a slowly varying component. The slowly

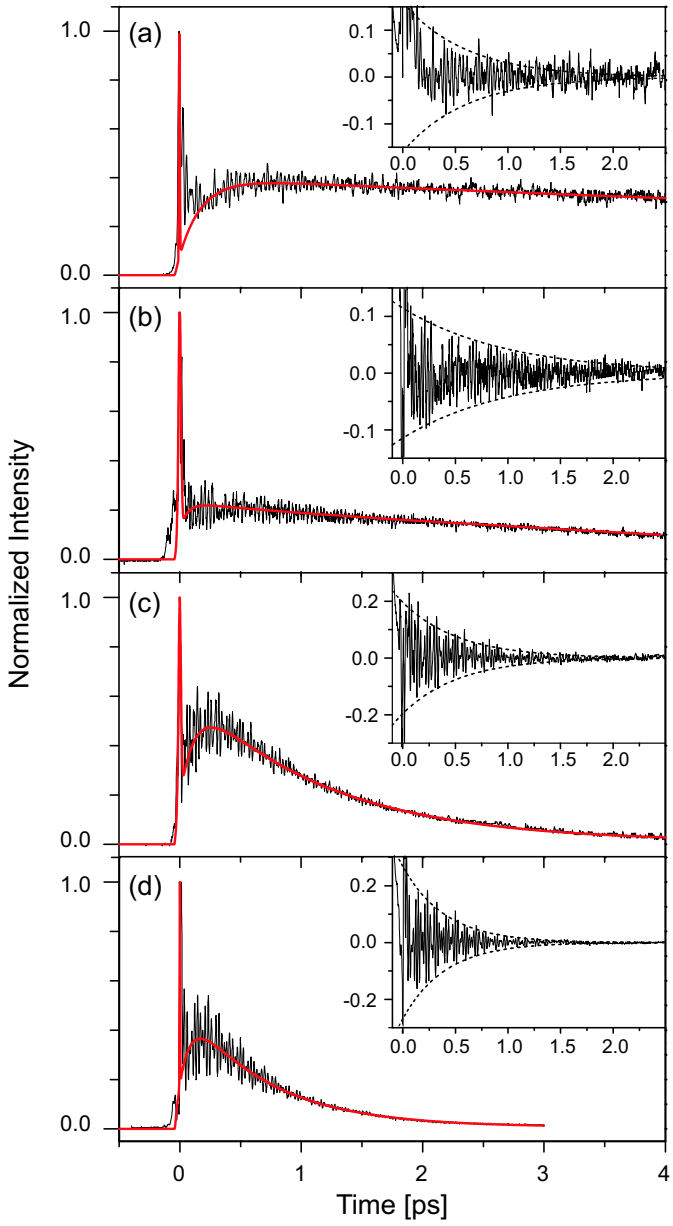

Figure 3.4: The TG signals (black line) observed with (a) C36, (b) C40, (c) C44, and (d) C50. The inset shows the oscillatory component which is obtained by subtracting the slowly varying component (red line) from the TG trace. The dashed lines indicate the exponential envelope of the coherent oscillations.

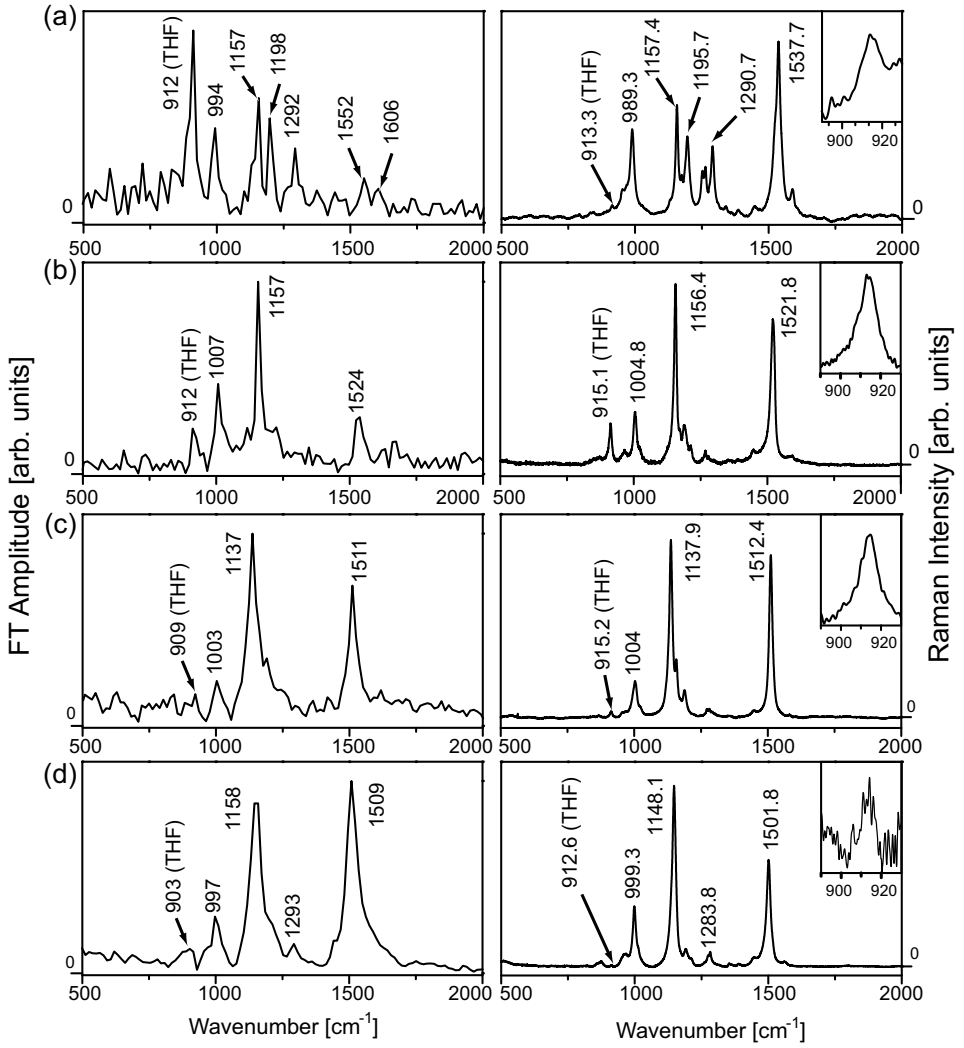

Figure 3.5: The CO-FT spectra (left-hand side) and the RR spectra (right-hand side) of (a) C36, (b) C40, (c) C44, and (d) C50. The ν_{THF} peak is magnified in the inset of the RR spectrum. The background fluorescence has been subtracted in the RR spectra.

varying component was fitted by using a Gaussian-shaped coherent spike and an electronic population function, which was derived from the two-state master equation. It is known that the slowly varying component originates from the population relaxation dynamics of the excited singlet states [70]. In particular, the gradual decay of the signal after the coherent spike shows a population relaxation from S_1 to S_0. The signal decays faster with increasing conjugation length of the homologues. The time constants of this decay are $\sim$ 20 ps for C36, 4.5 ps for C40, 1.2 ps for C44, and 0.6 ps for C50. These time constants are in agreement with previously reported values multiplied by a factor of 2 [77]. This is because the intensity of the TG signal is proportional to the square of the electric field, the magnitude of which linearly depends on the population relaxation lifetime, $\exp(-t/\tau)$. Here τ is the population relaxation time.

Homologue	ν_0	Assign.	Γ_{Raman}	Intensity
C36	913.3	ν_{THF}	9.7	0.13
	989.3	ν_3	8.4	1
	1157.4	ν_2	5.7	1.27
	1537.7	ν_1	10.0	2.03
C40	915.1	ν_{THF}	5.8	0.78
	1004.8	ν_3	7.3	1
	1156.4	ν_2	6.3	3.33
	1521.8	ν_1	8.6	2.68
C44	915.2	ν_{THF}	5.4	0.18
	1004.0	ν_3	10.3	1
	1137.9	ν_2	7.6	4.87
	1512.4	ν_1	7.3	4.46
C50	912.6	ν_{THF}	4.5	0.02
	999.3	ν_3	7.2	1
	1148.1	ν_2	8.4	3.06
	1501.8	ν_1	8.8	1.77

Table 3.1: The parameters of the main four peaks in the RR spectra. They were obtained by fitting the experimental data with a Lorentzian function. ν_0 and Γ_{Raman} indicate peak position of the Raman peak and half width at half-maximum, respectively (units: cm^{-1}). The value of intensity of each peak is normalized to that of ν_3.

The FT power spectra of the coherent oscillations (CO-FT spectra) and the RR spectra are shown in Fig. 3.5. The vibrational modes at around 1000 (ν_3), 1150 (ν_2), and 1500 (ν_1) cm^{-1} are the in-plane methyl-rocking, central C-C stretching, and central C=C stretching modes, respectively. The details of these four main peaks are summarized in Table 3.1. The frequency resolution in the CO-FT analyses is 10–20 cm^{-1}. The mode at 912 cm^{-1} is a solvent mode (ν_{THF}). Almost all of the modes observed in the CO-FT spectra are also observed in the RR spectra. This means that the observed coherent oscillations come from the ground-state vibrational modes [104–107].

The intensity of the peak of a vibrational mode in the CO-FT spectrum does not always correspond to that of its counterpart in the RR spectrum. Such differences arise because of the pulse character (finite pulse width or excitation energy) and initial phases of the vibrations [108]. In our study, these differences can be caused by following two factors: (1) Different pulse widths were used for generating the coherent oscillations in the measurements with the different homologues. Specifically the temporal pulse width used for C50 was shorter than that used for C36, because of the different excitation wavelengths required. The finite pulse width strongly diminishes the intensity of the ν_1 mode in comparison to the other lower-frequency vibrational modes, such as ν_2, ν_3, and ν_{THF} (this is because the frequency of the ν_1 mode is comparable to the width of the excitation pulse in the time domain). Therefore, the intensity of the ν_1 mode is more clearly observed in C50. (2) The excitation wavelength used for the RR measurement of each ho-

mologue is not at the same detuning wavelength relative to the S_2 energy. The deviation of this detuning wavelength more strongly affects the intensity of the chromophore's vibrational modes than that of the solvent. Therefore we will discuss only the relaxation rate of each vibrational mode in the coherent oscillations.

3.3.2 Simulations

We reported that both the TG profile and the linear absorption spectrum of β-carotene can be well reproduced using time-dependent perturbation theory [70]. Obtaining the mathematical expressions for the linear and nonlinear optical response functions is essential for the success of simulations of the optical responses of the homologues. Since the configurations of the energy-level diagrams of the β-carotene homologues are very similar to that of β-carotene, the TG profiles of the homologues are also expected to be describable within the same theoretical framework.

Briefly, third-order NLO phenomena in the homologues can be understood by a four-state model comprising S_0, S_1, S_2, and S_T (this is the two-photon absorption state that lies above the S_2 state). The four-state model gives five double-sided Feynman diagrams (R_1–R_5). The energy diagram and the five double-sided Feynman diagrams are shown in Fig. 3.6. Here the actual contribution of R_6, which was reported in Ref. [70], to the overall signal is negligible because our excitation energy is at an isosbestic point where the bleaching of the ground state is canceled out by the excited-state absorption [70]. Therefore we have omitted R_6 in this study. The mathematical expressions of R_1–R_5 are given by

$$R_1 = |\mu_{20}|^4 \exp[-g^*(\tau) + g^*(T) - g(\tau') - g^*(\tau + T) - g^*(T + \tau') + g^*(\tau + T + \tau')], \tag{3.1a}$$

$$R_2 = |\mu_{20}|^4 n_2(t) \exp[-g^*(\tau) + g(T) - g^*(\tau') - g^*(\tau + T) - g(T + \tau') + g^*(\tau + T + \tau')], \tag{3.1b}$$

$$R_3 = |\mu_{20}|^4 r(t) \exp[-g^*(\tau) - g(\tau')], \tag{3.1c}$$

$$R_4 = |\mu_{20}|^2 |\mu_{T2}|^2 n_2(t) \exp[-g^*(\tau) - g(\tau')], \tag{3.1d}$$

$$R_5 = |\mu_{20}|^4 [n_0(t) - r(t)] \exp[-g^*(\tau) - g(\tau')], \tag{3.1e}$$

where, by introducing $\Gamma \equiv \Gamma_{20} + \Gamma_{21}$,

$$n_2(t) = e^{-\Gamma t}, \tag{3.1f}$$

$$n_1(t) = \frac{\Gamma_{21}}{\Gamma_{10} - \Gamma}(e^{-\Gamma t} - e^{-\Gamma_{10} t}), \tag{3.1g}$$

$$n_0(t) = \frac{1}{\Gamma_{10} - \Gamma}[(\Gamma_{10} - \Gamma)(1 - e^{-\Gamma t}) + \Gamma_{21}(e^{-\Gamma_{10} t} - e^{-\Gamma t})], \tag{3.1h}$$

$$r(t) = (1 - \Gamma_{21})/\Gamma(1 - e^{-\Gamma t}). \tag{3.1i}$$

These response functions assume that the collective nuclear coordinate between any two states can be satisfactorily represented by the coordinate between S_0 and

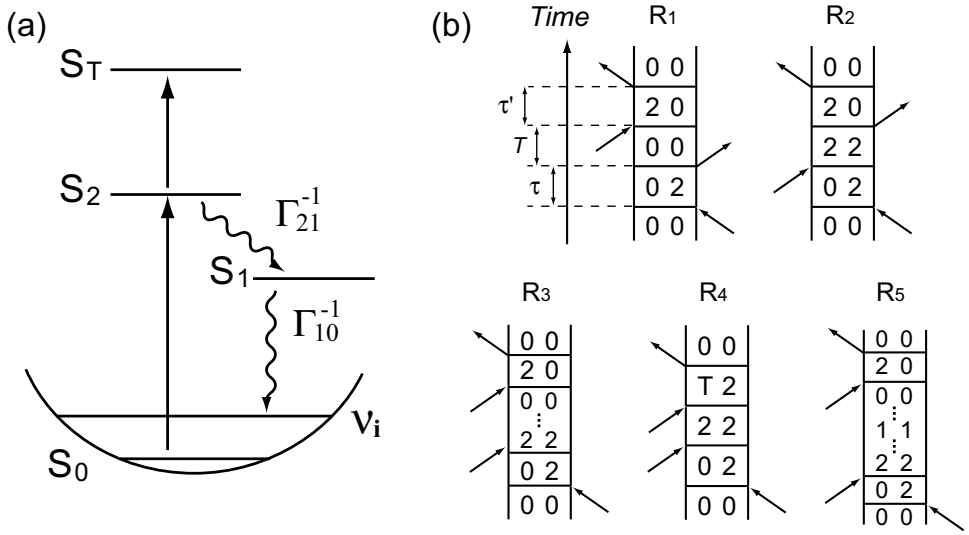

Figure 3.6: (a) The four-state model of β-carotene homologues, which comprises S_0, S_1, S_2, and S_T. The ν_i-frequency (i = 1–4) potential energy surface of the S_0 state is depicted. Γ_{21}^{-1} and Γ_{10}^{-1} are lifetimes of the S_2-S_1 and S_1-S_0 relaxations, respectively. (b) Double-sided Feynman diagrams that are used for the calculation. The symbols 0, 1, and 2 indicate the S_0, S_1, and S_2 states, respectively. The symbol T represents the state S_T. In the transient grating setup, $\tau = \tau' = 0$. The horizontal axis of the TG profile (Fig. 3.4) corresponds to the time duration T. The diagrams R_1 and R_2 are the same as a simple two-level system. The diagram R_3 includes the relaxation directly from S_2 to S_0, while R_5 represents the relaxation from S_2 to S_0 through S_1. The diagram R_4 indicates the two-photon absorption process. The details have been described in Ref. [70].

S_2. This approximation is not an oversimplification because the coherent oscillations observed in this study mainly consist of molecular vibrations from the ground state. Therefore, the response functions are constructed with a unique line-broadening function $g(t)$. The line-broadening function $g(t)$ indicates the time evolution of the transition frequency correlation and thus can be calculated from the spectral density [50]. The spectral density is determined by a combination of high-frequency (underdamped) vibrational modes, low-frequency (overdamped) vibrational modes and inhomogeneous broadening in the frame of a Brownian oscillator model. Here, the words "underdamped" and "overdamped" respectively mean $\gamma_j \ll \omega_j$ and $\gamma_j \gg \omega_j$ where ω_j and γ_j are the central frequency and the dephasing constant, respectively, of the jth Brownian oscillator mode. The graphs of spectral density used for the calculations are shown in Fig. 3.7. The population change of each electronic state is included in the master equation of the four states. The mathematical expressions of the linear absorption spectra (σ_a) is given by

$$\sigma_a \propto \mathrm{Re} \int_0^\infty \exp\left[\mathrm{i}(\omega - \omega_{20}) - g(\mathrm{t})\right], \tag{3.2}$$

supposing ω_{20} is the frequency between S_2 and S_0. The details of the theoretical descriptions of the TG profiles are discussed in Appendix B.

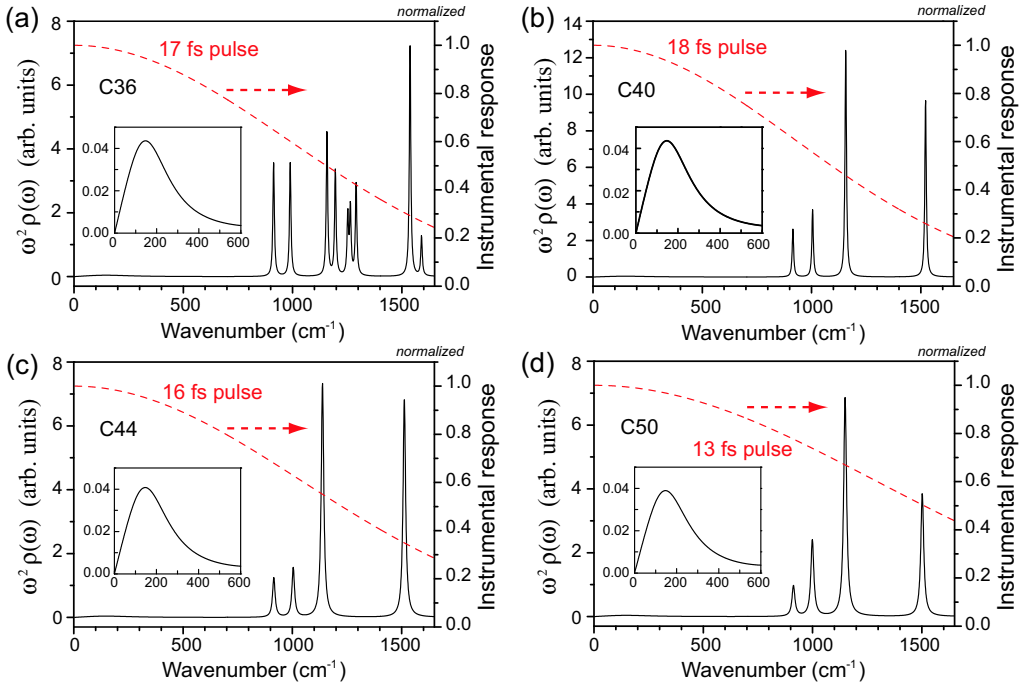

Figure 3.7: The graphs of spectral density used for the calculations (solid line) of (a) C36, (b) C40, (c) C44, and (d) C50. The instrumental response of the pulse width is also shown in each graph (dashed line). The instrumental response is a weighted factor that comes from the fact that finite pulse width diminishes the contributions of high-frequency region of spectral density. The inset shows the magnification of the spectral density of the low-frequency region. Note that the inhomogeneous contributions are not included in these spectral density. They are directly incorporated into the line-broadening function, $g(t)$.

The absorption spectra and the TG signals, which are simulated using the above treatment, are presented in Figs. 3.8 (a)–(d), and in Figs. 3.8 (e)–(h), respectively. As the degree of conjugation increases, the vibrational structure is more clearly observed in the absorption spectra. The spectral diffusion is determined by a combination of low-frequency vibrational modes and inhomogeneous broadening. In the Brownian oscillator model, this can be understood as an increase in the coupling strength of the overdamped Brownian oscillator (ω_B) and by the introduction of inhomogeneous broadening (Δ_{in}) [70]. In fact as the number of conjugated C=C double bonds increases, the coupling strength of these low-frequency mode (λ_B) is decreased and Δ_{in} vanishes as shown in Table 3.2. The dependence of the spectral broadening on the conjugation length has been suggested to be caused by the presence of the β-ionone ring [109]. Myers *et al.* showed that the presence of the double bond in the β-ionone ring gives rise to spectral broadening in the absorption spectrum [110]. By analogy to retinal and its homologues, this broadening has been attributed to steric hindrance between the β-ionone ring and the polyene backbone. Every β-carotene homologue has two β-ionone rings, one at each end. Therefore, the spectral broadening effect of

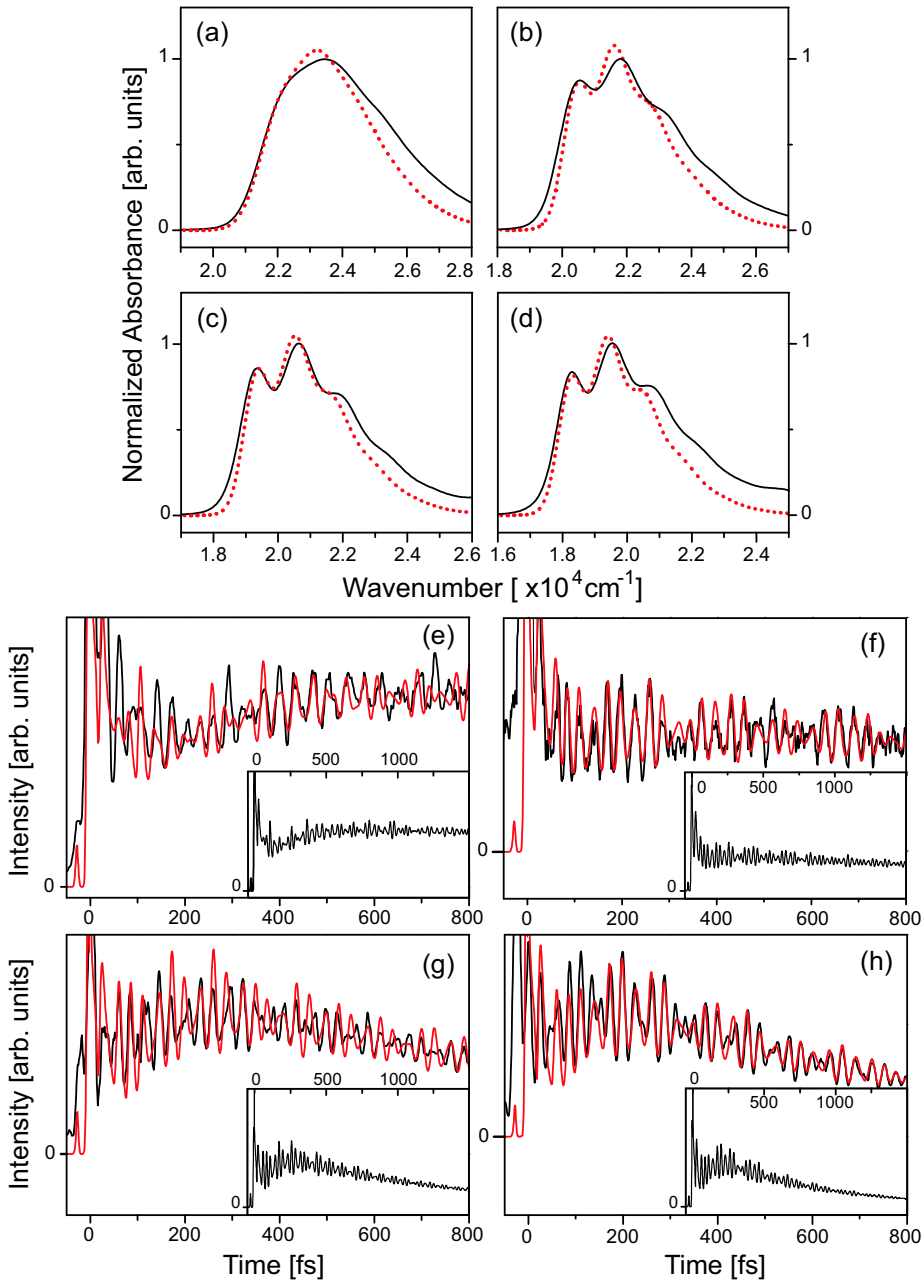

Figure 3.8: The calculated absorption spectra (red-dotted line) and the experimentally obtained absorption spectra (black-solid line) of (a) C36, (b) C40, (c) C44, and (d) C50 are compared. The calculated TG signals (red-solid line) and experimental data (black-solid line) from (e) C36, (f) C40, (g) C44, and (h) C50 are shown in the right panels. The insets in Figs. (e)–(h) show the calculated TG traces over a 1.5 ps time range.

β-ionone rings would be expected to be more dominant in the case of the shorter-chain homologues.

In the present simulation, we assume that the overdamped mode results only from the system-bath (molecule-solvent) interactions. The low-frequency modes

of the β-ionone ring typically exist in the region below 200 cm^{-1}, where molecule-solvent interactions are also found [110]. This complicates our situation, because these molecular-origin low-frequency modes give rise to spectral diffusion, as we have no experimental information on these low-frequency vibrational modes of the homologues owing to a strong Rayleigh scattering. Therefore, we ignore the fact that several low-frequency vibrational modes exist in the spectral density and assumed, for simplicity, one overdamped-Brownian mode as the contribution of the system-bath interaction and a single value of the inhomogeneous broadening as the contribution of the remaining low-frequency vibrational modes.

The linewidth of the underdamped vibrational mode (Γ_{HWHM}) is equivalent to the decay constant of the coherent oscillations divided by a factor of 2. Therefore, Γ_{HWHM} was determined from the experimental decay profile of the coherent oscillations. The mode frequencies and relative intensities of the vibrations of the homologues were determined from the RR spectra as summarized in Table 3.1. Since the relative intensities of the ν_{THF} mode of C36, C44 and C50 in the RR spectra are very weak, because of the resonance enhancement of the chromophore molecules, these values are set as a fitting parameter. The population relaxation constants and S_0–S_2 transition energies (ω_{20}) used for the calculations are summarized in Table 3.2. The simulated TG signals, which are shown in Fig. 3.8, were slightly shifted with respect to the experimental data, by less than 30 fs, in order that the calculated coherent oscillations match the experimental ones. The coherent spike is an instantaneous process and many response functions, which have been ignored under the condition of resonant stimulated 3-pulse photon echo, are necessary to accurately simulate it. The discrepancies at the early times reflect the difficulty in accurately accounting for such factors as the coherent spike, pulse shape or chirp.

We have successfully simulated the experimental TG traces simply by accounting for the electronic population dynamics and the ground-state vibrational coherences in these carotenoids. Our coherent spectroscopic study is able to clarify the mechanism of the energy dissipation in the ground-state vibrational manifold without any specific theoretical models. The vibrational relaxation in the ground state has been studied almost exclusively by means of anti-Stokes Raman scattering [77, 111]. In previous anti-Stokes Raman scattering studies, the population-relaxation times of the ground-state vibrational modes were also determined based on the theoretical model. In subsequent sections of this paper, we will clarify the relaxation dynamics in the ground-state vibrational manifolds without accounting for any specific theoretical models.

3.3.3 Time-frequency analysis of the coherent oscillations

It is important to know how the dephasing constants of the molecular vibrations are experimentally observed in the TG profiles. For this purpose, we have performed a simplified model calculation of the TG signal assuming an underdamped single Brownian oscillator in the high-temperature limit. Supposing the underdamped high-frequency modes (ω_0), which determine the dephasing constant γ_0,

Parameters	C36	C40	C44	C50
Δ_{in} (cm^{-1})	300	0	0	0
Γ_{HWHM} (cm^{-1})	4	4	7	8
ω_B (cm^{-1})	200	200	200	200
γ_B (cm^{-1})	300	300	300	300
λ_B (cm^{-1})	470	470	440	420
ω_{20} (cm^{-1})	23700	22150	20860	20050
Γ_{20}^{-1} (ps)	0.5	0.5	0.5	0.5
Γ_{21}^{-1} (fs)	210	150	90	70
Γ_{10}^{-1} (ps)	44.0	9.00	2.45	1.50
μ_{T2}/μ_{20}	1.2	1	1.2	1.2

Table 3.2: The parameters used for the calculation of the absorption spectra and TG signals observed with each homologue. Γ_{20}^{-1}, Γ_{21}^{-1}, and Γ_{10}^{-1} are the population relaxation times between S_2–S_0, S_2–S_1, and S_1–S_0, respectively. μ_{T2} and μ_{20} are the S_T–S_0 and S_2–S_0 transition dipole moments, respectively. The decay time of S_2 population is dominated by Γ_{21}^{-1} since Γ_{21}^{-1} is much smaller than Γ_{20}^{-1}. Therefore, we must assume that Γ_{20}^{-1} is 0.5 ps in all cases. The values of Γ_{21}^{-1} and Γ_{10}^{-1} were taken from Refs. [94] and [95], respectively. The simulations using these values closely reproduced the experimental results, though in the simulation with C50, Γ_{10}^{-1} was slightly longer than its reported value of Ref. [94].

the line-broadening function is given by [50, 112, 113]

$$g(t) = \exp\left(-\frac{\gamma_0}{2}t\right)\left[\coth\left(\frac{\hbar\omega_0}{2k_BT}\right)(1-\cos\omega_0 t) + i(\sin\omega_0 t - \omega_0 t)\right]. \tag{3.3}$$

The frequency spectrum of this Brownian oscillator (*i.e.* the spectral density) exhibits a Lorentzian shape with the half width at half-maximum (HWHM) of γ_0.

From this calculation, it can be concluded that the coherent oscillations observed in the TG signal come mainly from R_1 and the contributions from the other response functions are eventually seen as a slowly varying component. It should be noted that R_2, in which vibrational modes of the S_2 state will contribute to the coherent oscillations, very rapidly decays on the time scale of Γ_{21}^{-1} ($S_2 \rightarrow S_1$: ~150 fs for β-carotene), and this means that the measured coherent oscillations do not include any vibrational modes from the S_2 state. Thus the decay of the coherent oscillations can be considered as the temporal profile of R_1. The decay of the coherent oscillations in the simulated R_1 temporal profile has an asymmetric form at early times, as shown in Fig. 3.9. This shows that the decay of the coherent oscillations is not a simple exponential function, because it has the mathematical form $\exp[\exp(-\gamma_0 t/2)] - A_{\text{offset}}(t)$, where $A_{\text{offset}}(t)$ is the slowly varying component. Nevertheless the decay of the coherent oscillations can be well approximated by $\pm\exp(-\gamma_0 t/2)$ in the time region beyond 0.5 ps. Therefore the dephasing constant γ_0 can be determined by fitting $\pm\exp(-\gamma_0 t/2)$ to the experimentally determined decay profile of the vibrational mode.

The coherent oscillations contain information on how vibrational modes behave in the time domain. This temporal behavior can be examined by using

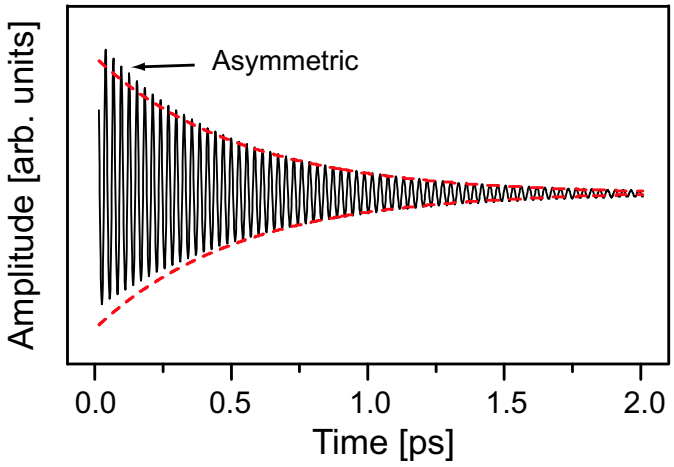

Figure 3.9: The temporal profile of R_1, which was calculated using the line-broadening function of Eq. (3.3). Red-dashed lines indicate a fit to $\pm\exp(-\gamma_0 t/2)$. Asymmetric feature of the decay of the coherent oscillations is observed in the early time, but it can be fitted to $\pm\exp(-\gamma_0 t/2)$ in the time region more than 0.5 ps.

a wavelet transformation (WT), which affords minimum time-frequency uncertainty [114–117]. The WT signal, that is a function of variables a and b, is expressed by

$$F(a,b) = \int_{-\infty}^{\infty} dt\, f(t)\psi\left(\frac{t-b}{a}\right), \tag{3.4}$$

where $f(t)$ is the signal to be analyzed. $\psi(t)$ is known as the mother wavelet [114]. The parameters a and b are the dilation and translation parameters, respectively. The unit of parameter a is in the frequency scale, but does not correspond to the exact frequency obtained in the Fourier transformation. This is because a and b cannot be simultaneously determined due to the time-frequency uncertainty. Analogously, the unit of parameter b is in the time scale but does not match the exact time after excitation as determined in the experimental measurements. If the mother wavelet does not have a maximum peak at b, such as in the case of a Daubechies wavelet [114], the physical meanings of the parameters a and b are very complex and difficult to understand. Therefore, we have employed a wavelet whose physical meaning is straightforward, *i.e.*, a complex Morlet wavelet, which is defined by [114]

$$\psi(t) = \pi^{-1/4}(e^{i\omega_0 t} - e^{-\omega_0^2/2})e^{-t^2/2}. \tag{3.5}$$

The second term in the parentheses becomes negligible for values of $\omega_0 \gg 0$ in practice. In this case Eq. (3.5) can be written as

$$\psi(t) \sim \pi^{-1/4}\exp[i\omega_0 t - t^2/2]. \tag{3.6}$$

Here ω_0 is the central frequency of the wavelet. We will use rad s^{-1} unit for ω_0 for consistency with the description in Ref. [114]. It determines how localized the WT of the spectrogram is in the frequency domain; a large value of ω_0 makes the WT localized in the frequency domain but delocalized in the time domain [114].

In principle it is an arbitrary parameter, but its choice is actually constrained. Consequently, the choice of the value of ω_0 is not a critical factor for the determination of the dephasing times. In this study, we have confirmed that the dephasing time of the vibrational mode does not depend on the value of ω_0 ranging from 8 to 15. $\omega_0 = 8$ corresponds to the Gaussian width (HWHM: σ) of $\sigma = 350$ fs at 1000 cm^{-1}. It should be noted that the Gaussian width is a frequency-dependent value in the WT. Analogously, $\omega_0 = 15$ corresponds to $\sigma = 650$ fs. When $\omega_0 < 5$ ($\sigma < 220$ fs), the vibrational modes included in the coherent oscillations cannot be well separated in the frequency domain because of an insufficient number of wave forms included in the Gaussian envelope. A value of ω_0 of more than 15 makes the WT meaningless, since the Gaussian envelope with such a large ω_0 will cover almost of all of the ranges of the TG profiles. No temporal information on the vibrational frequency mode can be known by using the time-frequency analysis. Therefore, one can determine the correct dephasing time by using the WT without loss of generality. In the subsequent analyses we set ω_0 to be 8 (σ = 350 fs.) because it gives a good separation between the vibrations included in the coherent oscillations (specifically between the 1157 and 1196 cm^{-1} modes of C36), without a large loss of time information .

The WT of the spectrograms of the coherent oscillations of the homologues are presented in Fig. 3.10. These spectrograms clearly show the temporal behavior of the vibrational modes included in the coherent oscillations. In order to determine the dephasing times of the vibrational modes observed in the WT spectrograms, a single exponential decay function has been fitted to the temporal profile of each vibrational mode. The dephasing times of the four main vibrational modes of each homologue are shown in Fig. 3.11 and summarized in Table 3.3. One clearly sees that the dephasing times of the vibrational modes of the homologues decrease as the conjugation length increases. In particular, the dephasing times of the ν_2 and ν_3 modes drastically decrease as the conjugation length increases, while those of ν_1 and ν_{THF} only show moderate changes.

It should be noted that the frequencies of the vibrational modes fluctuate in time. This probably reflects the fact that any given mode is coupled by interactions with many other vibrational modes. In principle, these fluctuations cannot be observed in the population-based time-resolved Raman spectra because they result from the phase of the vibrational mode, which is perturbed by the environment. In other words, this is a purely coherent phenomenon. Therefore, a different experimental approach is needed to be able to analyze these fluctuations [118]. The fact that we can, however, detect these purely coherent phenomena demonstrates the advantage of our spectroscopic technique. Since these fluctuations are on the order of a few tens of wave numbers and this corresponds to a translation of ~ 0.4 μm of the optical delay line, a very high temporal resolution is required to study this phenomenon in detail. Unfortunately this is beyond the capabilities of our present apparatus. It will be a subject of a future work.

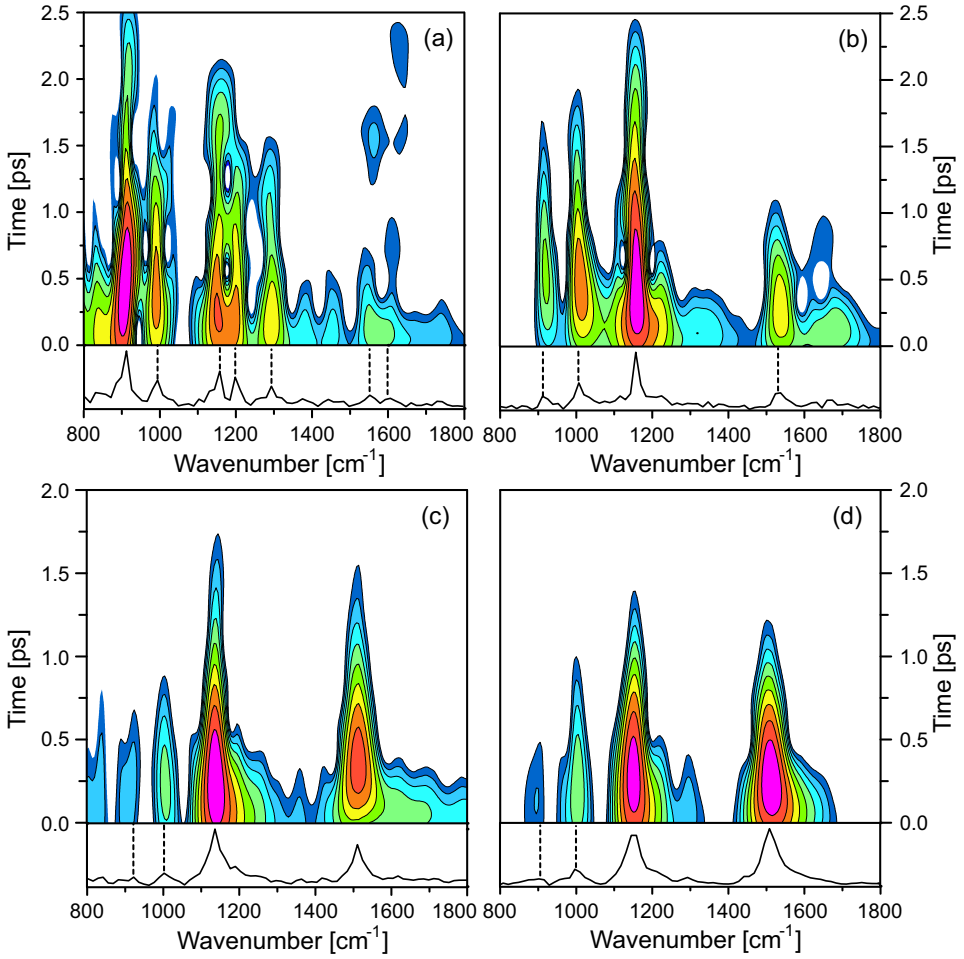

Figure 3.10: The WT spectrograms of (a) C36, (b) C40, (c) C44, and (d) C50. The data are shown with a log-scale coloring: amplitude increases from blue to red. The bottom panel at each spectrogram shows the CO-FT spectrum of each homologue.

Assign.	C36	C40	C44	C50
ν_{THF}	1.45 ± 0.05	1.64 ± 0.20	1.35 ± 0.39	1.22 ± 0.2
ν_3 (-CH_3)	1.41 ± 0.18	1.73 ± 0.10	0.88 ± 0.03	0.97 ± 0.10
ν_2 (C-C)	1.87 ± 0.31	1.58 ± 0.09	1.29 ± 0.12	0.89 ± 0.09
ν_1 (C=C)	0.99 ± 0.07	1.04 ± 0.09	1.05 ± 0.03	0.81 ± 0.09

Table 3.3: The total dephasing times of the four main vibrational modes of the homologues (unit: ps). The error margins show experimental errors. We have analyzed a set of three TG profiles for each homologue under the same condition of the wavelet transformation.

3.3.4 The conjugation-length dependence of vibrational dephasing

The time-dependent perturbation theory, which has been employed for the simulations in this study, does not explicitly specify the mechanism of relaxation because the relaxation is phenomenologically included in this theory. The dephasing time, which we have determined here, is defined as the total dephasing time T_2. The total dephasing consists of two types of dephasing, and it can be given by (see Section 2.2 on page 16) [50, 122–124]

$$T_2^{-1} = (2T_1)^{-1} + T_2^{*-1}. \tag{3.7}$$

Here, T_1 is the population-relaxation time and T_2^* is the pure dephasing time. Pure dephasing originates from fluctuations in the energy levels that come from the environment, namely the bath. These two relaxations cause dephasing in the system, and the relaxations of most of the physical observables reflecting coherent processes (*e.g.* the linewidth of the Raman scattering peak and of the hole-burning spectrum, and the temporal decay constant of the coherent oscillations) are expressed by an exponential decay, with the total dephasing time T_2 under the fast modulation limit.

The population-relaxation times of the ground-state vibrational modes of β-carotene have been reported to be 8–15 ps [77]. Similar relaxation times have also been found for C50 and an $n = 19$ homologue [125]. Although the relaxation times of the other homologues have not been determined, these relaxation times are probably similar for all of the homologues used in the present study. These population-relaxation times are sufficiently large compared to the total dephasing

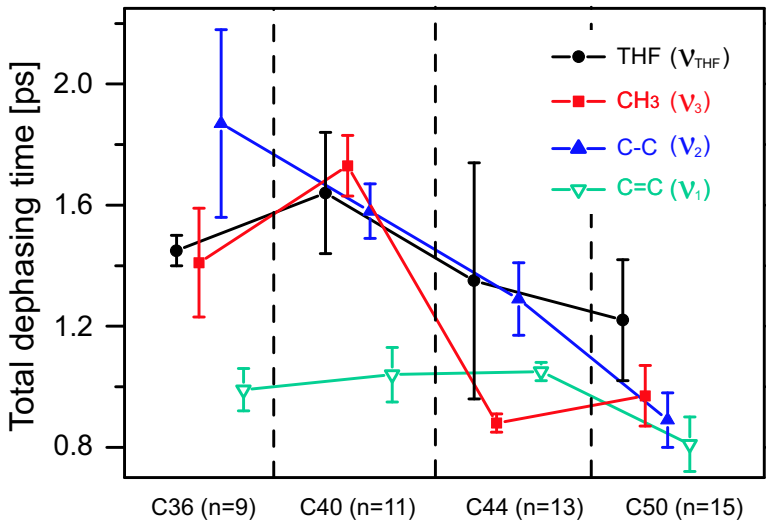

Figure 3.11: (a) The total dephasing times of the four main vibrational modes of the homologues. (b) The correlation diagram of Γ_{Raman} and Γ_{CO} plotted against the number of conjugated C=C double bonds in the homologues. The plot of each mode is slightly translated horizontally for ease of visualization of their error bars.

times that the population-induced dephasing terms in Eq. (3.7) can be ignored. We thus conclude that the dephasing of the ground-state vibrational modes of the β-carotene homologues is mainly caused by system-bath interactions.

The conjugation-length dependence of the total dephasing time of each vibrational mode is very interesting. In particular, the two polyene-backbone central stretching modes, ν_1 and ν_2 show remarkable differences in their chain-length dependence. The dephasing time of the ν_2 mode strongly depends on the conjugation length whereas that of the ν_1 mode does not. Since the ν_1 and ν_2 modes are very important in the processes of energy dissipation and relaxation in carotenoids, on the basis of our results, we can conclude that the energy dissipation occurs mainly through the ν_1 mode in the shorter-chain carotenoids. In contrast the longer-chain carotenoids do not appear to have such a specific dissipation channel.

3.4 Summary

The TG signals from a series of β-carotene homologues, by using sub-20-fs excitation pulses, have been measured in order to investigate the dependence of their ultrafast optical response on the extent of the π-conjugation length. The experimental data were compared to the computational simulations based on a Brownian oscillator model, in order to determine how the solvation effect depends on the length of the π-conjugation. In these simulations the required spectral densities were determined from the resonance Raman spectra. The experimental TG data can be well reproduced in the simulations by using a combination of the spectral densities and the reported population relaxation times of the $S_2 \rightarrow S_1$ and $S_1 \rightarrow S_0$ transitions. The effects of the low-frequency modes, which represent solvation effects, decrease as the number of conjugated C=C bonds increases from 9 to 15. The total dephasing times of the homologues have been determined by applying wavelet transformation analyses to the coherent oscillations, which were observed in the experimental TG traces. It has been determined that the dephasing of ground-state vibrational modes in the β-carotene homologues are mainly caused by system-bath interactions. The dephasing times of the C-C and C=C central stretching modes show remarkable differences in their conjugation-length dependence: The dephasing time of the C-C stretching mode strongly depends on the conjugation length whereas the C=C stretching mode does not. This trend clearly shows that shorter-chain carotenoids have a specific major channel (the ν_1 mode) to the environment, whereas the longer-chain carotenoids do not.

Chapter 4

Large third-order optical nonlinearity of β-carotene homologues

4.1 Introduction

Large optical nonlinearity has attracted much attention for applications in optical devices. The configuration and conformation of carotenoids, which is a typical π-conjugated molecule, are well-characterized compared to π-conjugated polymers, therefore, the mechanism that produces the large optical nonlinearities in carotenoids have been extensively studied [23–25, 126–133]. For example, it has been shown that introduction of polar functional groups into carotenoids is a promising way to enhance their optical nonlinearity [25, 133]. This increase in the magnitude of the optical nonlinearity, however, has the unfortunate side effect of losing optical transparency in the visible wavelength region. The work described here is motivated by finding other strategies that simultaneously improve the magnitude of the optical nonlinearity and such serious side effects of losing transparency.

Here, we show that the third-order optical nonlinearity of carotenoids can be greatly enhanced by merely adding more C=C conjugated double bonds (n) to β-carotene. The optical nonlinearity of the homologues of β-carotene (symmetric nonpolar carotenoids, see Fig. 4.1) can be comprehensively described with a three-state model, including the ground state S_0 ($1^1A_g^-$: classified on the basis of the C_{2h} point symmetry), the one-photon allowed state S_2 ($1^1B_u^+$), and the higher-lying one-photon forbidden state, S_m ($m^1A_g^-$), which is a controversial state that has been claimed to be essential for creating the large optical nonlinearity in carotenoids [25, 128, 130–132]. Our theoretical analyses show that the large optical nonlinearity in the nonpolar symmetric carotenoids can be achieved without the S_m state. Rather the enhancement of the optical nonlinearity in these carotenoids mainly results from the three-photon resonance of the transition from S_0 to S_2. In the case of the asymmetric polar carotenoids the same three-state model are applied

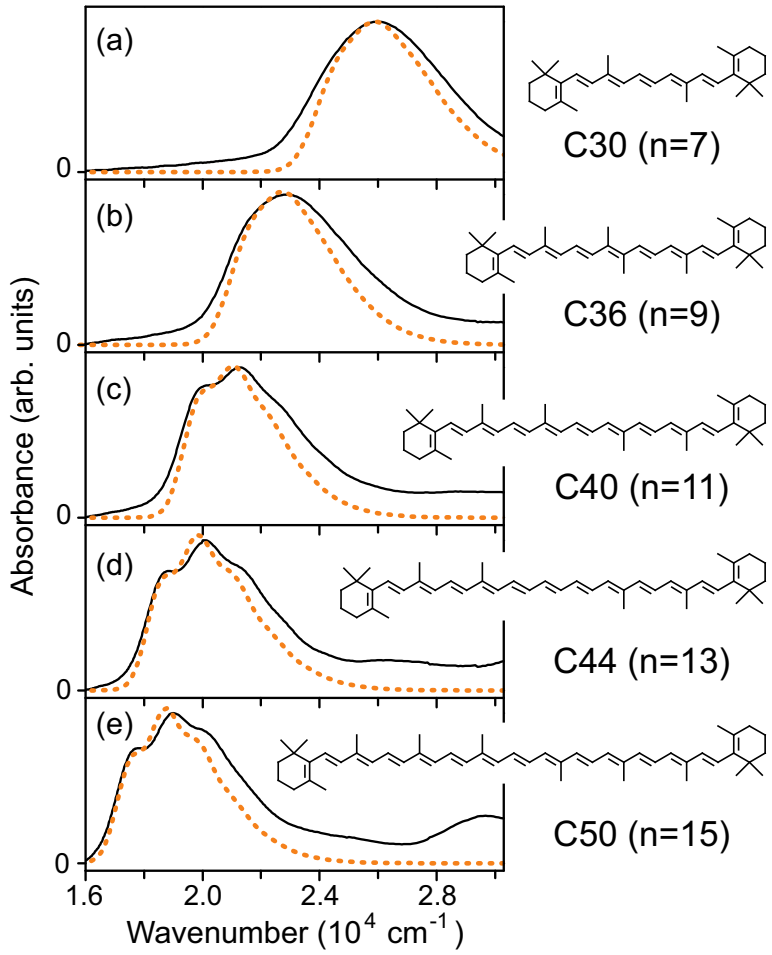

Figure 4.1: The experimental (solid line) and simulated (dotted line) absorption spectra of (a) C30, (b) C36, (c) C40, (d) C44, and (e) C50, respectively. The chemical structure of each homologue is shown in the inset with their respective conjugation lengths *n*.

to account for the third-order optical nonlinearity, but in this case the origin of the enhancement is due to the strong electronic coupling between the S_2 and S_m states [25]. Thus changing *n* gives another way to dramatically enhance the third-order optical nonlinearity in carotenoids without sacrificing optical transparency in the visible region.

4.2 Experimental details

4.2.1 Sample preparation

The β-carotene homologues were synthesized and purified as described in a previous report [103]. They were doped into polystyrene films, which were spin-coated onto a fused silica substrate. The carotenoid's concentration (*i.e.* number density) was determined from its absorption maximum and molar extinction coefficient of

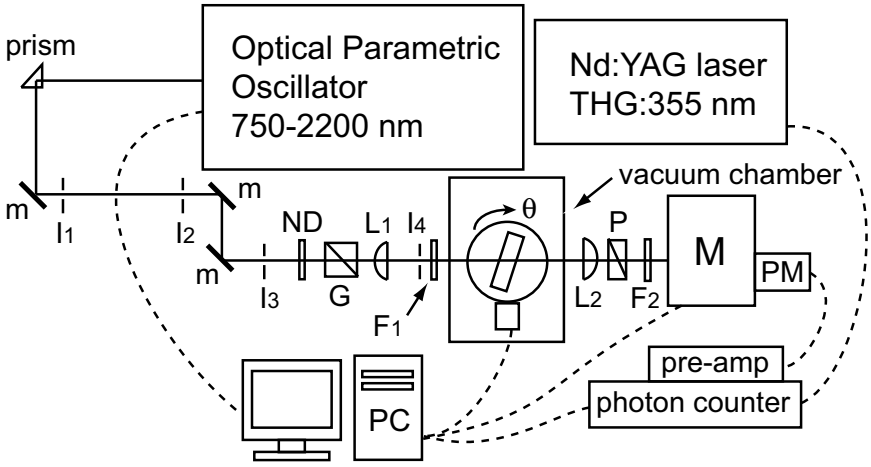

Figure 4.2: Experimental setup of the THG Maker fringe measurement. m: mirror, I_1–I_4: iris, L_1, L_2: lens, F_1, F_2: color-glass filter, ND: neutral density filter, P: polarizing film, G: Glan-laser prism, M: monochromator, PM: photomultiplier tube.

each homologue measured in THF solution [103]. Stylus profilometry showed that the film thickness was typically between 0.04–0.06 μm.

4.2.2 Experimental setup

Shown in Fig. 4.2 is a schematic picture of the experimental setup for the THG Maker fringe measurement. A pulsed Nd:YAG laser pumped, optical parametric oscillator (Spectra-Physics, MOPO-PO, Quanta-Ray Pro 250-10) was used as the light source. The fundamental input had a repetition rate of 10 Hz, together with 60–400 μJ/pulse in energy at the focusing point on the sample. The power of the input beam was controlled with a neutral-density filter. The laser beam was filtered from stray lights using a color-glass filter and was linearly polarized with a Glan-laser prism. The beam was weakly focused (f = 300 mm) into the sample mounted on the rotation stage. A diameter of the beam at the slab was approximately 50–100 μm. The sample was kept in a vacuum chamber in order to avoid the air's destructive contribution to the THG signals [134]. Polarizations of the fundamental wave and of the THG wave were set to the direction parallel to the rotation axis. The THG wave generated in the sample was separated from the fundamental wave using a monochromator (Nikon, G-250). The THG wave was detected and measured using a time-gated photon-counting technique (Hamamatsu, R928P and H7421-50; Stanford, SR400 and SR440). The $\chi^{(3)}$ value of the fused silica substrate was taken as 1.4×10^{-14} esu and used as the reference [135].

4.2.3 Analyzing method of THG Maker fringes

When the fundamental input is incident on the NLO medium, several types of THG waves are generated in the medium and propagate in itself as shown in Fig. 4.3 (b). They make an interference pattern as a function of the incident angle

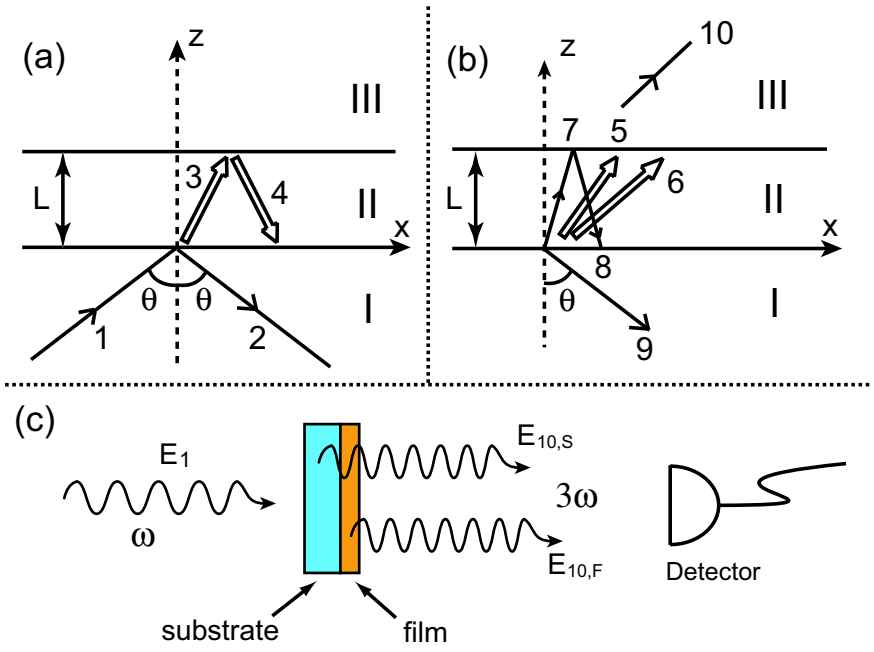

Figure 4.3: The schematic picture of the wave propagation in the media. There are (a) the ω-waves and (b) 3ω-waves. (c) The electric field of 3ω-wave, which we measure using a detector, is a sum of the substrate-origin and the film-origin 3ω-waves.

(θ) of the fundamental input to the medium, *i.e.* Maker fringes. Maker fringes are frequently used for the quantitative determination of the second and third-order NLO susceptibilities [130–132, 136–139]. van Beek *et al.* found the mathematical expressions of this fringing pattern for the case of THG. Here, we briefly review the basic concept of their formulation of the THG Maker fringes [132, 140, 141].

First we assume a case that a fundamental plane wave (ω-wave) propagates through three different isotropic media, I, II, and III [see Fig. 4.3 (a)]. The ω-wave, denoted Wave 1, is reflected back into the medium I (Wave 2) and refracted into the medium II (Wave 3 and 4). Wave 3 and 4 are multiply reflected forwarding and back-warding waves, respectively. Figure 4.3 (b) shows the 3ω-waves (Wave 5–10). There exist two kinds of 3ω-waves in the medium II, *i.e.* bound waves (Wave 5, 6) and free waves (Wave 7, 8). The origin of these two types of waves is found in the wave equations, which are derived from the Maxwell equations, as

$$\mathrm{rot}\,\mathrm{rot}\boldsymbol{E}(3\omega) - (3\omega/c_0)^2\boldsymbol{\varepsilon}(3\omega) : \boldsymbol{E}(3\omega) = 0,$$
$$\mathrm{rot}\,\mathrm{rot}\boldsymbol{E}(3\omega) - (3\omega/c_0)^2\boldsymbol{\varepsilon}(3\omega) : \boldsymbol{E}(3\omega) = \mathcal{P}_{NL}(3\omega) \quad (3\omega\text{-bound wave}),$$

where c_0 and $\boldsymbol{\varepsilon}$ are the speed of light in vacuum and dielectric constant. The bound wave is a 3ω-wave, which is generated by the *source term*, $\mathcal{P}_{NL}$, of the nonlinear polarization. The free wave is the one that already exists when the bound wave is generated. Wave 8 and 9 are reflected 3ω-wave in the media II and I, respectively. Wave 10 is a transmitted 3ω-wave into the medium III.

Multiple reflections are taken into account only in the polystyrene film. The multiple reflections in the fused silica substrate can be ignored because the thick-

ness of the substrate is sufficiently large compared to the wavelength. Wave propagation in the film can be developed in analogy with the theoretical descriptions of the wave propagations in the substrate. We will describe the details in Appendix C.

The THG intensity is proportional to the square of the total THG electric field as $I_{10}^{Total} \propto |E_{10}^{Total}|^2$, Here E_{10}^{Total} is actually a sum of substrate-origin ($E_{10,S}$) and film-origin ($E_{10,F}$) 3ω-wave, hence it can be written as

$$I_{10}^{Total} \propto |E_{10}^{Total}|^2 \quad \text{with} \quad E_{10}^{Total} = \alpha(E_{10,S} + E_{10,F}). \tag{4.2}$$

α is film's absorption correction factor of the 3ω wave, which is given by

$$\alpha = \exp\left[-3i \frac{n_F^{3\omega}\kappa_F}{\sqrt{(n_F^{3\omega})^2 - \sin^2\theta}} k_0 L_F \right]. \tag{4.3}$$

Here n_F, κ_F, k_0 and L_F are refractive index of the film at 3ω, absorption coefficient of the film at 3ω, wavenumber of the ω-wave in vacuum, and the film thickness, respectively. In the present experimental setup, the media are ordered as air-substrate-film-air; hence $E_{10,S}$ can be given by

$$\begin{aligned}
E_{10}^{S} &= \sqrt{A_S}(e^{i(\phi_{5,S}-\phi_{7,S})} - 1)\chi_S^{(3)} T_S^3 E_1^3, \\
A_S &= \frac{2\xi_{7,S}(\xi_{3,S} + \cos\theta)(\xi_{3,S} + \xi_{7,S})}{(\xi_{10,S} + \xi_{7,S})^2(\xi_{7,S} + \cos\theta)(\xi_{3,S}^2 - \xi_{7,S}^2)}, \\
T_S &= \frac{2\cos\theta}{\cos\theta + \xi_{3,S}}, \quad \phi_{5,S} = 3\xi_{3,S} k_0 L_S, \quad \phi_{7,S} = 3\xi_{7,S} k_0 L_S, \\
\xi_{3,S} &= \sqrt{\varepsilon_S^{\omega} - \sin^2\theta}, \quad \xi_{7,S} = \sqrt{\varepsilon_S^{3\omega} - \sin^2\theta}, \quad \xi_{10,S} = \sqrt{\varepsilon_F^{3\omega} - \sin^2\theta},
\end{aligned} \tag{4.4}$$

where $\chi_S^{(3)}$, L_S, ε_S^{Ω}, and ε_F^{Ω} are, respectively, the third-order nonlinear optical susceptibility, thickness of the substrate, dielectric constant of the substrate at frequency Ω, and dielectric constant of the film at frequency Ω. Analogously, $E_{10,F}$ can be described as follows,

$$\begin{aligned}
E_{10}^{F} &= \sqrt{A_{F1}}(e^{i(\phi_{3,F}-\phi_{7,F})} - 1)\chi_F^{(3)} T_F^3 T_S^3 E_1^3 + \sqrt{A_{F2}}(e^{i(\phi_{6,F}-\phi_{7,F})} - 1)\chi_F^{(3)} T_F^2 R_F T_S^3 E_1^3, \\
A_{F1} &= \frac{2\xi_{7,F}(\xi_{3,F} - \xi_{9,F})(\xi_{3,F} + \xi_{7,F})}{(\cos\theta + \xi_{7,F})^2(\xi_{7,F} - \xi_{9,F})(\xi_{3,F}^2 - \xi_{7,F}^2)}, \\
A_{F2} &= \frac{2\xi_{7,F}(\xi_{6,F} - \xi_{9,F})(\xi_{6,F} + \xi_{7,F})}{(\cos\theta + \xi_{7,F})^2(\xi_{7,F} - \xi_{9,F})(\xi_{6,F}^2 - \xi_{7,F}^2)}, \\
T_F &= \frac{t_1}{1 + r_1 r_2 e^{i2\phi_{3,F}}}, \quad R_F = \frac{t_1 r_2 e^{i2\phi_{3,F}}}{1 + r_1 r_2 e^{i2\phi_{3,F}}}, \\
r_1 &= \frac{\xi_{1,F} - \xi_{3,F}}{\xi_{1,F} + \xi_{3,F}}, \quad t_1 = \frac{2\xi_{1,F}}{\xi_{1,F} + \xi_{3,F}}, \quad r_2 = \frac{\xi_{3,F} - \cos\theta}{\xi_{3,F} + \cos\theta}, \quad t_2 = \frac{2\xi_{3,F}}{\xi_{3,F} + \cos\theta},
\end{aligned} \tag{4.5}$$

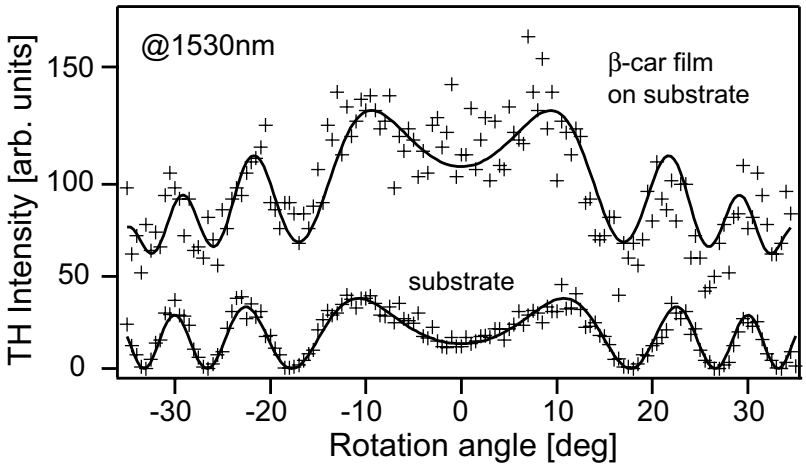

Figure 4.4: Typical fringes observed in the film/substrate (upper) and substrate alone (bottom).

with

$$\phi_{3,F} = \phi_{6,F} = \xi_{3,F} k_0 L_F, \quad \phi_{5,F} = 3\xi_{3,F} k_0 L_F, \quad \phi_{7,F} = 3\xi_{7,F} k_0 L_F,$$
$$\xi_{1,F} = \xi_{3,S} = \sqrt{\varepsilon_S^{\omega} - \sin^2\theta}, \quad \xi_{3,F} = 3\xi_{6,F} = \sqrt{\varepsilon_F^{\omega} - \sin^2\theta},$$
$$\xi_{7,F} = \sqrt{\varepsilon_S^{3\omega} - s^2}, \quad \xi_{9F} = -\sqrt{\varepsilon_S^{3\omega} - s^2}.$$

The dielectric constant ε^{Ω} is given by the square of the refractive index n^{Ω} under the weak absorption limit. The dispersions of the refractive indices of the silica substrate and the polystyrene film are determined from their Sellmeier equations. The Sellmeier equation of the substrate was calculated from a set of the refractive indices at several wavelengths, which is provided by Sigma [142]. It is given by

$$n_S^2(\lambda) = 2.1033 + \frac{0.00886}{\lambda^2 - 0.0109} - 0.00898\lambda^2 - 0.00011\lambda^4, \tag{4.6}$$

where $n_S(\lambda)$ is a refractive index of the fused silica substrate and λ is wavelength in μm unit. The Sellmeier equation of the polystyrene film has been obtained from the reported values of their refractive indices at several wavelengths [143];

$$n_F^2(\lambda) = 2.44519 + \frac{0.02746}{\lambda^2 - 0.02185}. \tag{4.7}$$

The resultant $|\chi_S^{(3)}|$ is converted to the molecular hyperpolarizability, $\gamma(-3\omega;\omega,\omega,\omega)$ through a following equation [132],

$$\gamma(-3\omega;\omega,\omega,\omega) = 5 \times \frac{|\chi^{(3)}(-3\omega;\omega,\omega,\omega)|}{L(3\omega)L^3(\omega)N} \quad \text{with} \quad L(\omega) = \frac{n^2(\omega)+2}{3}. \tag{4.8}$$

Here $L(\omega)$ and N are the local field correction factor at frequency ω and the number density of the homologues in the thin film, respectively.

Figure 4.4 shows two types of typical fringes observed in the β-carotene-film coated substrate and in the substrate alone. One can clearly see that the observed THG intensity is enhanced by the contributions from the β-carotene film. We have successfully made the good fit of our equation to the experimental data. The obtained $\chi^{(3)}$ value at $\lambda_{3\omega}$ =510 nm was consistent with previously reported values [131]. This fact guarantees the validity of our measurements.

4.3 Results and discussion

4.3.1 The γ values of β-carotene homologues

Figures 4.1(a)–(e) show the absorption spectrum of each homologue in the polymer matrix. The main absorption peaks in the spectra are due to the transitions to the S_2 state. The energy of the S_2 state decreases as n increases [145]. Figures 4.5(a)–(e) show the second hyperpolarizability γ and phase spectra of each homologue. One can clearly see the strong enhancement of $\gamma_{\max}$ (the γ measured at the peak) from 1.3×10^{-32} to 31×10^{-32} esu as n increases from 7 to 15. The latter value is 3.4 times higher than that of β-carotene (9.2×10^{-32} esu), which itself shows one of the largest optical nonlinearity ever reported [23, 25]. This is an unexpectedly large increase as a result of just extending the number of conjugated C=C double bonds in a typical nonpolar symmetric carotenoid such as β-carotene. It should be noted that the largest γ value of C50 is actually 34×10^{-32} esu and is located at around 17300 cm^{-1}. This γ value is, however, anomalously enhanced compared with the simulated result. The disagreement is accounted for the effect of the experimental artifact, which has been marked in the phase spectra.[†] For this reason, we consider that the experimental $\gamma_{\max}$ of C50 is located at 18550 cm^{-1} (31×10^{-32} esu), at which the simulated γ spectrum also has its maximum.

Previously such large optical nonlinearity has been generated by the introduction of electron donors and/or acceptors at the ends of the conjugation chain [23, 25, 26, 126, 133]. Marder *et al.* have reported that large enhancement of $\gamma_{\max}$ can be achieved by introducing strong electron acceptors [25]. They prepared several polar carotenoids having different functional groups. Their $\gamma_{\max}$ values increased as the wavelength of the linear absorption maxima ($\lambda_{\max}$) of their derivatives were much more strongly red-shifted, as shown in Fig. 4.6(a), in contrast to the homologues used by us in the present study. Here we have also plotted our results of $\gamma_{\max}$ as a function of the $\lambda_{\max}$. The values of $\gamma_{\max}$ of our homologues are proportional to $(\lambda_{\max})^{10.3}$, while those of Marder *et al.*'s samples are proportional to $(\lambda_{\max})^{6.6}$. Notably the sharper increase of γ provides the transparency over the wide spectral region. Therefore our finding has potential benefits for applications in devices. In fact, the $\gamma_{\max}$ of C50 ($\lambda_{\max}$ = 526 nm) is 2.5 times higher than

[†]In the phase spectra, an experimental artifact is observed at the same energy region in every homologue. The origin of this artifact is not clear. However, we believe that it is an artifact because at the energy at which it is located the homologues do not have any absorption and so the phase angle would be expected to be zero.

that of the equivalent carotenoid derivative described by Marder *et al.* that has its absorption maximum at approximately 540 nm [see Fig. 4.6(a)].

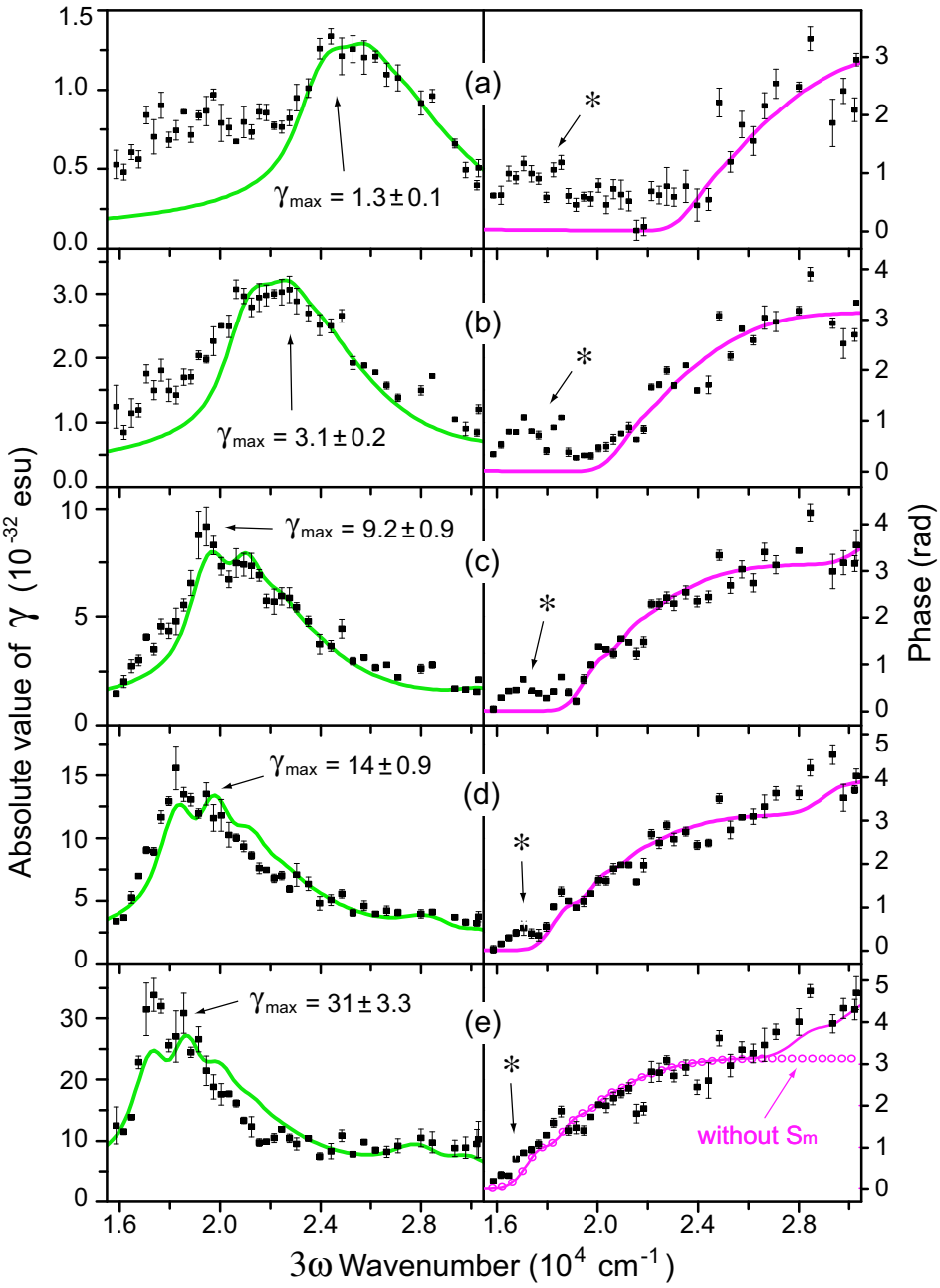

Figure 4.5: The experimental (square dots) and simulated (solid line) γ and phase spectra of (a) C30, (b) C36, (c) C40, (d) C44, and (e) C50, respectively. The left-hand side shows the γ spectrum, while the right-hand side shows the phase spectrum. The symbol ($*$) indicates the experimental artifact (see footnote in page 53). The simulated phase spectrum of C50 without including the S_m state is shown in Fig. (e) by the open circles.

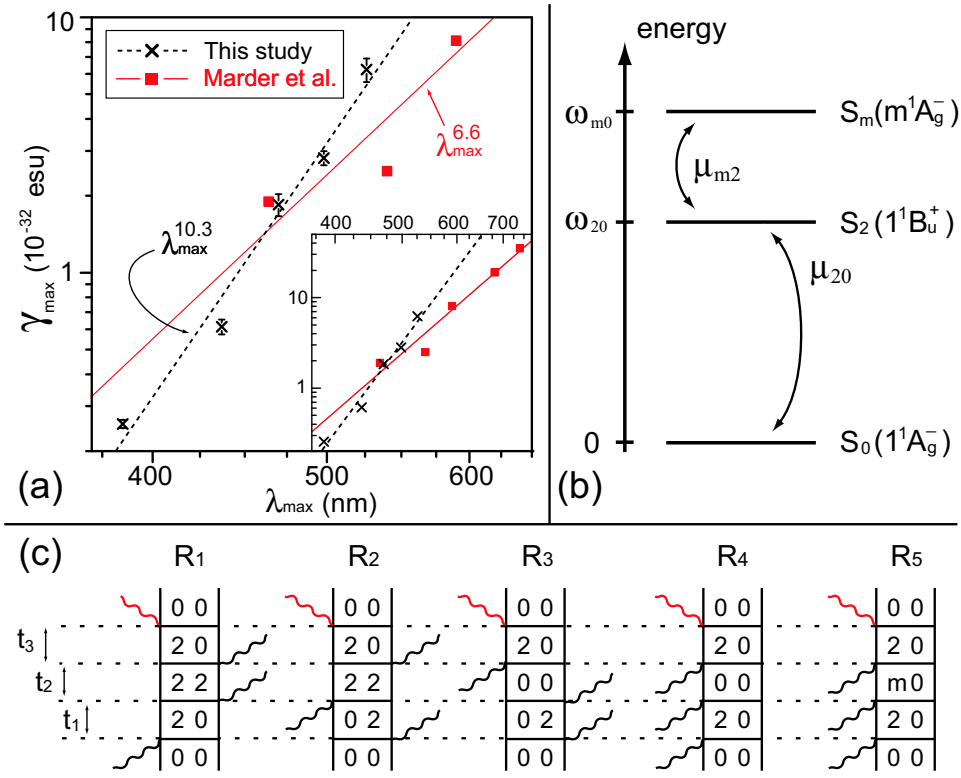

Figure 4.6: (a) Log-log plot of the $\gamma_{\max}$ values of the homologues and of the Marder's asymmetric polar carotenoids [25] as a function of $\lambda_{\max}$. Our values of $\gamma_{\max}$ are rescaled to theirs by taking account of the local field correction factor, which in their paper was taken as unity. The inset shows their data in the range above 600 nm. (b) The energy diagrams of the homologues used in the simulations. ω_{20}, ω_{m0}, μ_{20}, and μ_{m2} are the S_2–S_0 transition frequency, the S_m–S_0 transition frequency, the coupling strength between S_2 and S_0, and the coupling strength between S_2 and S_m, respectively. (c) The double-sided Feynman diagrams of the THG process used in our simulations. Here 0, 2, and m indicate the S_0, S_2, and S_m states, respectively. Black and gray (or red online) wavy lines indicate ω-photon and 3ω-photon, respectively.

Samuel *et al.* reported a similar range of the optical nonlinearity using *m*-phenylene-vinylene type oligomers [146]. In their study, γ values, which were comparable to our results, were realized in quite large oligomers (n = 50–100), in contrast to number of theoretical predictions that the cubic nonlinearity would be more rapidly increased with respect to n. They ascribed this inconsistency to the molecular structure of their sample, *i.e.* a *cis*-linkage, existed in π-conjugated double bonds, diminishes the electron delocalization. Therefore the β-carotene homologues can be regarded as a more idealistic π-conjugated system for studying optical nonlinearity, because they have no bond discontinuities within the π-conjugated double bonds.

4.3.2 Simulations based on time-dependent perturbation theory

In order to clarify the mechanism that gives rise to the large nonlinearity in the present homologues, we have made theoretical simulations based on time-dependent perturbation theory. In this theoretical framework, any time-domain or frequency-domain spectroscopic signal can be calculated using a set of response functions. Since these response functions describe the time evolution of the molecule's polarization, frequency-domain optical spectra can be derived from the half-Fourier transform of the response functions [50]. Thus a correct description of the response functions for the THG process should be sufficient to allow the γ and phase spectra to be calculated.

The total response function of the THG process can be described as

$$S^{(3)}_{\mathrm{THG}}(t_3, t_2, t_1) = \left(\frac{i}{\hbar}\right)^3 \sum_{a,b,c,d} P(a)\mu_{ab}\mu_{bc}\mu_{cd}\mu_{da}\langle \mathscr{G}_{bc}(t_3)\mathscr{G}_{cd}(t_2)\mathscr{G}_{da}(t_1)\rho_g\rangle, \qquad (4.9)$$

where $\mathscr{G}_{ba}(t) = \mathrm{Tr_S}[|a\rangle\langle b|\ G(t)\ |b\rangle\langle a|]$. Here, $P(a)$, μ_{ab}, $\mathscr{G}(t)$, ρ_g, and $\mathrm{Tr_S}$ are, respectively, a thermal population of state a, transition dipole moment between state a and b, Green's superoperator, density matrix of the ground state, and quantum trace over the system degrees of freedom in the framework of the system-bath reduced equation of motion. The superoperator represents a commutator, of which usual Hilbert-space operator acts from left and right, such as $\mathscr{G}A = [G, A] = GA - AG$ where A is an arbitrary Hilbert-space operator. The angular bracket in Eq. (4.9) means taking the ensemble average over the bath. Here, we assume that three excited states are involved in the THG process S_0, S_2, and S_m, therefore the suffices a, b, c, and d may take these three states. It should be noted that S_1 state lying betwee S_2 and S_0 does not involve in the THG process. This can be verified that our three-state model provide good simulations of the experimental data.

Figures 4.6(b) and (c) respectively show an energy diagram of the homologues and double-sided Feynman diagrams of the THG process, which remain under following two conditions: (1) the first photon always makes coherence between the S_2 and S_0 states because only the S_2 state can be accessed from S_0 due to symmetry considerations. (2) the ground state population must always be created

after the final interaction because the emitted 3ω-photon must fulfill the resonance condition.

Based on the density matrix formalisms, after the coherence between the S_0 and S_2 state ($|2\rangle\langle 0|$ or $|0\rangle\langle 2|$) is created by the first interaction, the populations of the S_2 ($|2\rangle\langle 2|$) and the S_0 ($|0\rangle\langle 0|$) states are created by the pathways R_1 to R_4. Those populations then proceed to make again coherence between the S_2 and S_0 states [$|2\rangle\langle 0|$ or $|0\rangle\langle 2|$, see Fig. 4.6(c)]. Then this coherence reaches the S_0 population ($|0\rangle\langle 0|$) by the final interaction. On the other hand, the pathway R_5 is a *population free* process. By this pathway, after the first interaction, the S_2–S_0 coherence ($|2\rangle\langle 0|$) is generated and then the second interaction generates S_m–S_0 coherence ($|m\rangle\langle 0|$). After the third photon has interacted with the system the density matrix will again form coherence between S_2 and S_0 ($|2\rangle\langle 0|$), because the subsequent interaction (emission of 3ω-photon) will then generate the ground state population. Hence, Eq. (4.9) can be written as

$$S^{(3)}_{\mathrm{THG}}(t_3,t_2,t_1) = \left(\frac{i}{\hbar}\right)^3 \Big[\mu_{20}^4 \langle \mathscr{G}_{20}(t_3)\mathscr{G}_{22}(t_2)\mathscr{G}_{20}(t_1)\rho_g\rangle + \sum_j \mu_{20}^4 \langle \mathscr{G}_{20}(t_3)\mathscr{G}_{jj}(t_2)\mathscr{G}_{02}(t_1)\rho_g\rangle + \sum_f \mu_{20}^2\mu_{2f}^2 \langle \mathscr{G}_{20}(t_3)\mathscr{G}_{2f}(t_2)\mathscr{G}_{20}(t_1)\rho_g\rangle\Big]. \quad (4.10)$$

Here the thermal population of the ground state $P(0)$ is taken to be unity before the interaction of the first photon. The suffices 0, 1, 2, and T denote S_0, S_1, S_2, and S_T, respectively. When the bath correlation time is very short compared to inverse linewidth (fast modulation limit [50]), the statistical ensemble of the product of Green functions may be factorized into the product of the averaged Green functions, such as

$$\langle \mathscr{G}_{bc}(t_3)\mathscr{G}_{cd}(t_2)\mathscr{G}_{da}(t_1)\rho_g\rangle \sim \langle \mathscr{G}_{bc}(t_3)\rho_g\rangle\langle \mathscr{G}_{cd}(t_2)\rho_g\rangle\langle \mathscr{G}_{da}(t_1)\rho_g\rangle. \quad (4.11)$$

This factorization approximation is equivalent to ignoring any correlations between the three time durations t_1, t_2, and t_3. The time-ordered three-fold integral in Eq. (4.10) are able to be unfolded to the three independent integrals. This factorization approximation is vitally important for saving a huge amount of computational tasks.

Using a Brownian oscillator model (see Section 2.3 at page 19) [50, 70], the mathematical expressions of the response functions R_1 to R_5 are given by

$$S^{(3)}_{\mathrm{THG}}(t_3,t_2,t_1) = \sum_{i=1}^{5} R_i(t_3,t_2,t_1), \quad (4.12a)$$

$$R_1 = R_4 = |\mu_{20}|^4 \exp[-i\omega_{20}(t_1+t_3)]\exp[-g(t_1)-g(t_3)], \quad (4.12b)$$

$$R_2 = R_3 = |\mu_{20}|^4 \exp[i\omega_{20}(t_1-t_3)]\exp[-g^*(t_1)-g(t_3)], \quad (4.12c)$$

$$R_5 = |\mu_{20}|^2|\mu_{m2}|^2 \exp[-i\omega_{20}(t_1+t_3)-i\omega_{m0}t_2]\exp[-g(t_1)-g(t_2)-g(t_3)]. \quad (4.12d)$$

Here $g(t)$ is a line-broadening function [70]. The parameters in these equations are defined in the caption of Fig. 4.6. The response functions R_1–R_5 assume that

Parameters	C30	C36	C40	C44	C50
ω_{20} ($\times 10^4$cm^{-1})	2.39	2.10	1.94	1.82	1.72
ω_{m0} ($\times 10^4$cm^{-1})	–	2.20	2.03	1.93	1.86
μ_{m2}/μ_{20}	–	0.55	0.55	0.65	0.75
Δ_{in} (cm^{-1})	500	450	300	290	290
λ_B (cm^{-1})	650	550	490	420	370
Γ_{HWHM} (cm^{-1})	5	4	4	7	8

Table 4.1: The parameters used for the theoretical simulations. We have assumed ω_B = 200 cm^{-1} and γ_B = 200 cm^{-1} for every homologue. λ_B, ω_B and γ_B are, the coupling strength, the central frequency, and the linewidth of a lower-frequency Brownian oscillator, respectively. Δ_{in} and Γ_{HWHM} are the inhomogeneous broadening and the linewidth of a higher-frequency Brownian oscillator, respectively. They have been defined in Ref. [70] (We have omitted the solvation reorganization energy described in this reference in order to set ω_{20} to the value of the conventional 0–0 excitation energy.) Note that ω_{m0} and μ_{m2}/μ_{20} of C30 cannot be determined because the two-photon resonance at its S_m state is outside of our experimental frequency range.

the collective nuclear coordinate between any two states can be satisfactorily represented by the coordinate between the S_0 and S_2 states. Therefore the response functions are described with a unique line-broadening function $g(t)$. The mathematical expressions of $g(t)$ of β-carotene homologues have been already described in Chapter 3.

Briefly, we first constructed a spectral density [$\rho(\omega) = \rho_H(\omega) + \rho_L(\omega)$] of each carotenoid based on the Brownian oscillator model [50]. For underdamped high-frequency modes $\rho_H(\omega)$, we assumed three Lorentzian peaks [methyl rock-in-plane (ν_3), C-C central stretching (ν_2), and C=C central stretching mode (ν_1)] whose central frequencies and peak intensities were experimentally determined by stationary Raman measurements. The Lorentzian linewidths of n = 9–15 carotenoids were taken from the data obtained in Chapter 3 (see page 41). The linewidth of n = 7 carotenoid is assumed to be 5 cm^{-1} in analogy with that of the n = 9 carotenoid. For the overdamped low-frequency modes $\rho_L(\omega)$, we assumed a following function,

$$\rho_L(\omega) = \frac{2}{\pi\omega} \frac{\lambda_B \omega_B^2 \gamma_B}{(\omega_B^2 - \omega^2)^2 + \omega^2 \gamma_B^2} \tag{4.13}$$

Here, λ_B, ω_B, and γ_B are the coupling strength, the central frequency, and the linewidth of the overdamped-Brownian oscillator, respectively. We included inhomogeneous contributions (Δ_{in}) because the samples were dispersed in the polymer matrix (see Section 2.3). The graphs of spectral density used for the calculations are shown in Fig. 4.7.

The linear absorption spectra were calculated as described previously [70, 147]. The second hyperpolarizability γ with its phase term $e^{i\psi}$ can be obtained from

$$\gamma e^{i\psi} \propto -\int_0^\infty dt_3 \int_0^\infty dt_2 \int_0^\infty dt_1 [S^{(3)}_{\text{THG}}(t_3, t_2, t_1) - S^{(3)*}_{\text{THG}}(t_3, t_2, t_1)] e^{i3\omega t_3} e^{i2\omega t_2} e^{i\omega t_1}. \tag{4.14}$$

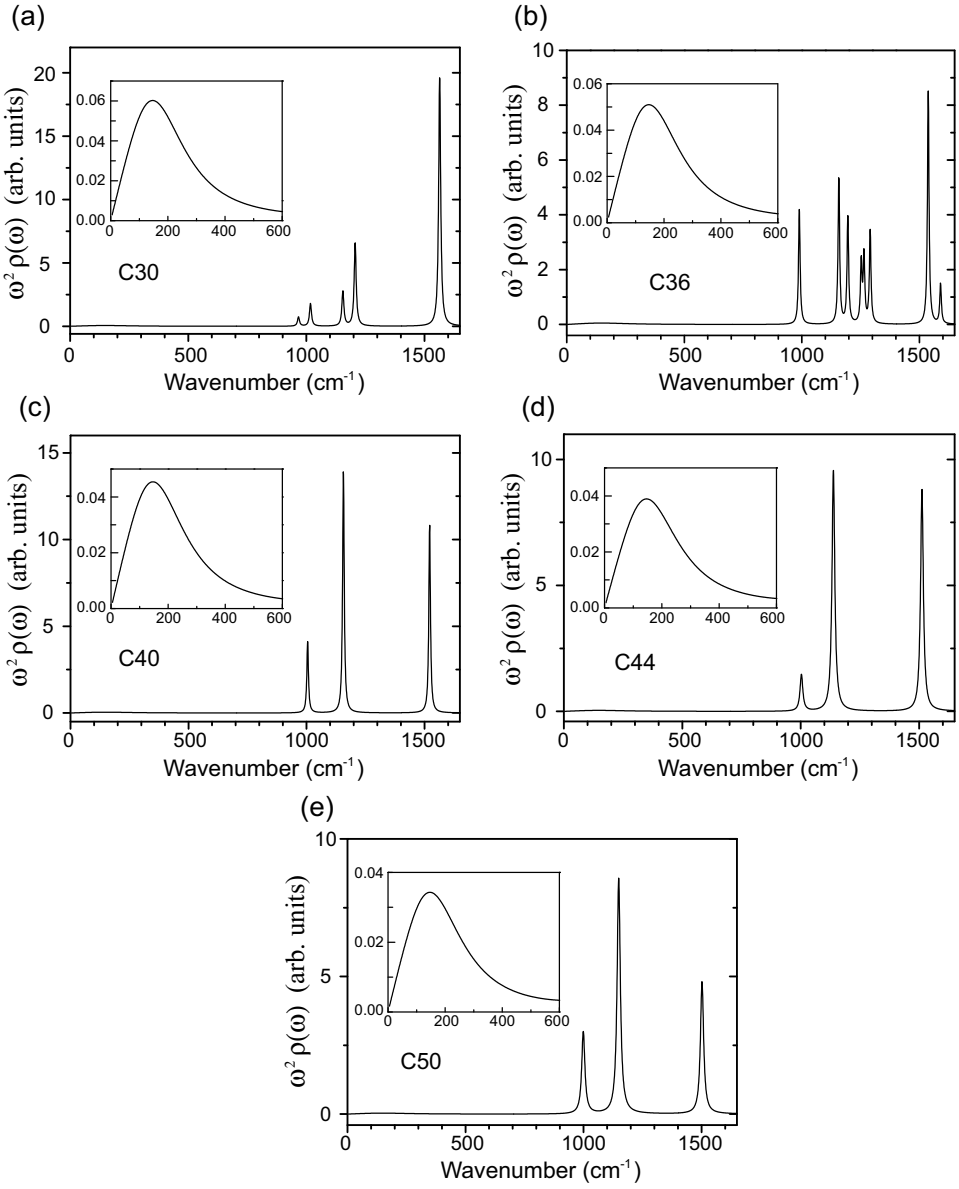

Figure 4.7: The graphs of spectral density used for the calculations of (a) C30, (b) C36, (c) C40, (d) C44, and (e) C50. Here we assume impulsive excitation limiti, *i.e.* $\delta(t)$-function laser pulse. The inset shows the magnification of the spectral density of the low-frequency region. Note that the inhomogeneous contributions are not included in these spectral density. They are directly incorporated into the line-broadening function, $g(t)$.

The results of these simulations are shown in Figs. 4.1 and 4.5. The parameters used in the simulations are summarized in Table 4.1. The simulations of the absorption spectra are in good agreement with the experimental ones (Fig. 4.1). The small discrepancy at the low energy wavelength edge is due to reflections at the surface of the film (A correction for these reflections has not been applied.) [148]

Although another optically allowed excited state appears on the higher energy

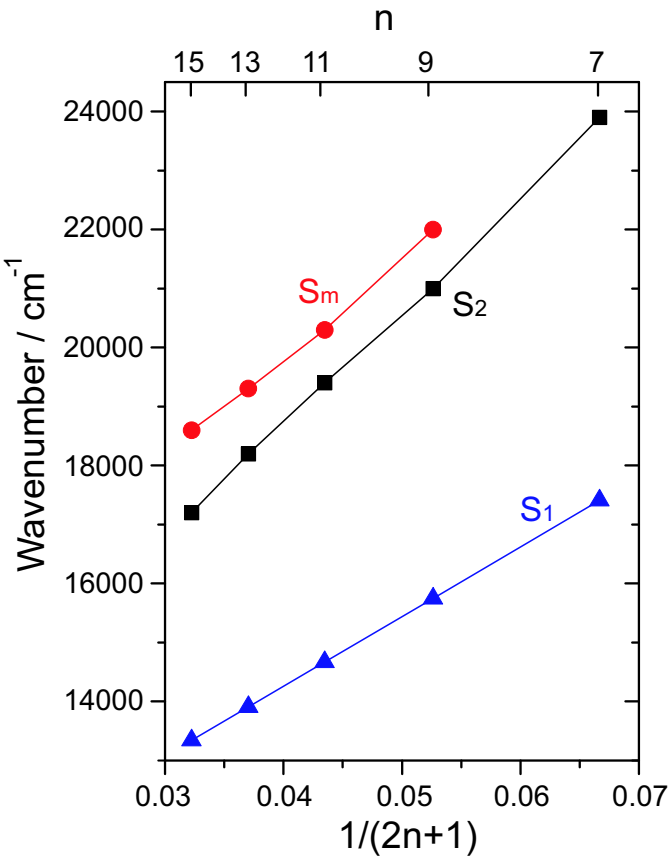

Figure 4.8: The energy location of the essential state S_m as a function of $1/(2n+1)$. The energy locations of the S_2 and S_1 states are also depicted for the reference.

side of the S_2 state in the spectrum of C50 (see the peak around 30000 cm^{-1}), this state can be ignored because of the lack of its contribution to the nonlinear optical response. The simulated γ and phase spectra also show good agreement with the experimental data (see footnote in page 53).

4.3.3 The essential state S_m

We can see the presence of the S_m state in the β-carotene homologues and the dependence of its energy level on n. The energy location of the S_m state listed in Table. 4.1 is visualized in Fig. 4.8. The phase spectra are particularly sensitive to contributions from the S_m state. The phase spectra of C30 and C36 can be reproduced using only two states, *i.e.* the S_0 and S_2 states [see Figs. 4.5(a) and (b)]. In these cases the contribution of the S_m state is quite small in our energy region of interest because the two-photon resonances with the S_m states will occur far above our experimental energy region (*e.g.* 33000 cm^{-1} for C36). In the case of the other three carotenoids, the contributions of the S_m state must be considered [see Figs. 4.5(c)–(e)] because the phase still increases from π in the spectral range of above 26000 cm^{-1}. A simulated phase spectrum of C50 without including the

contribution of the S_m state is shown in the right-hand panel of Fig. 4.5(e).

A similar three-state model can also be used to take account the large optical nonlinearity of the asymmetric polar carotenoids.[‡] In this case the electronic coupling of the S_2–S_m states plays a crucial role in generating the large optical nonlinearity. On the other hand, the strong enhancement of $\gamma_{\max}$ in the present set of carotenoids comes from a simple three-photon resonance to the S_2 state. The contribution of the two-photon resonance to the S_m state to the magnitude of $\gamma_{\max}$ is less than 20% even in C50, in which the largest value of μ_{m2} is observed (see Table 4.1).

Our detailed theoretical analyses have clarified the nature of the S_m state, which has been a controversial issue in the interpretation of the THG spectrum of a π-conjugated molecule [130–132], *e.g.* its energy location and/or the strength of its coupling to the S_2 state. The S_m state is determined to be located slightly (~1000 cm^{-1}) above the S_2 state, and to be weakly coupled (μ_{m2}/μ_{20}~0.6) to the S_2 state. The S_m state accounts for the non-zero small γ values in the high-energy spectral region of the γ spectra, which still remain above the S_2 resonance (above 22000 cm^{-1} in the C50's spectrum, for example). The S_m state does not have a large contribution to the $\gamma_{\max}$ value (less than 20%) as stated above. We thus conclude that the strong enhancement of $\gamma_{\max}$ in the nonpolar carotenoids comes from a simple three-photon resonance of the S_2–S_0 transition. It should be noted that our result is derived from the systematic study on the dispersion of γ with respect to the length of the pure-polyenic conjugated chain. There have been number of studies that claim the importance of the *essential* state [23, 25–27, 126, 128–132], but the effect of the *essential* state on the relationship between the dispersion ofγ and the length of pure-polyenic structure is still uncertain. Our present study provides comprehensive information on the dependence of the character of the *essential* state on the length of pure-polyenic structure and shows that in this case the *essential* state is of minor importance.

This simple mechanism of the three-photon resonance enhancement of γ in the symmetric nonpolar carotenoids, by increasing *n*, has the advantage that it can enlarge the optical nonlinearity dramatically while retaining optical transparency in the visible region. It should be emphasized that our finding does not diminish the importance of introducing polar functional groups to a polyenic chain in order to induce large optical nonlinearity, since this method can also be applied to relatively short carotenoids with low values of *n*. Rather the strong coupling of the S_2 and S_m states seems more suitable to get closer to the fundamental limit of the magnitude of γ described in recent reports. [26, 27] In this context, there may be a possibility in the future that one can realize much larger γ values, together with the same range of wide transparency of the present carotenoids, by increasing μ_{m2}.

[‡]There exists a one-photon forbidden state, S_1, between S_0 and S_2. It does not actually contribute to the THG process. Note that the S_2 and S_m states in the present study are denoted S_1 and S_2, respectively, in Ref. [25].

4.4 Summary

We have shown that a very large enhancement of γ of the nonpolar symmetric carotenoids can be obtained by increasing n a rather small amount. A systematic study about the dependence of the γ and phase spectra of a group of β-carotene homologues on n have led us to the detailed understanding on the THG response of these carotenoids. Our theoretical simulations based on time-dependent perturbation theory have been able to show that a three-state model consisting of S_0, S_2, and S_m is sufficient for accurately describing the THG process in the homologues used in the present study as well as the data previously obtained with some asymmetric polar carotenoids [25]. It has been shown that the controversial higher-lying essential state S_m is not important for generating the large value of $\gamma_{\max}$ in our nonpolar symmetric carotenoids. Moreover the strong enhancement of $\gamma_{\max}$ in the case of β-carotene homologues mainly originates from three-photon resonance of the S_2 state. Thus changing n provides another way to greatly enhance optical nonlinearity in carotenoids without having to introduce polar constituents.

Chapter 5

Large second-order optical nonlinearity of crystalline π-conjugated system

5.1 Introduction

Organic nonlinear optical (NLO) crystals have a better NLO capacity, with lower dielectric constants, than their inorganic counterparts. For this reason, organic NLO crystals have attracted significant attention in terahertz (THz) generation [149–151]. Basic properties required for the applied use of NLO crystals are large optical nonlinearity and sufficient size to be subjected to mechanical processes, such as crystal cutting and polishing at any angle. These two characteristics are in opposition: large optical nonlinearity can easily be achieved in a lower-symmetrical structure, which usually results in a small and fragile crystal. Molecules having large optical nonlinearity are likely to condense into a crystal with a centrosymmetric structure, in which second-order NLO processes are forbidden. This is because the centrosymmetric structure is energetically more stable, when compared to the noncentrosymmetric one. For example, 2-methyl-4-nitroaniline (MNA), a typical organic NLO crystal, has a large optical nonlinearity [152–154], but growth of its large crystal with a good optical quality is extremely difficult due to the morphology and thermal decomposition behavior in the liquid state [152,153]. Such features of MNA are directly related to its lower symmetry, *i.e., monoclinic Cc*. Thus, the development of a highly effective NLO crystal that has a large optical nonlinearity and large dimension is still warranted.

N-benzyl 2-methyl-4-nitroaniline (BNA) is an *N*-derivative of MNA and has been developed to overcome these difficulties. It easily crystallizes and affords a large second-order optical nonlinearity in comparison with MNA [155]. Through the optical rectification process, a strong THz electromagnetic wave was generated. Its intensity was comparable to the leading organic THz emitter, 4-dimethylamino-*N*-methyl-4-stilbazolium tosylate (DAST) [156]. More recently, the intensity of the THz radiation from the BNA crystal has been improved such that it

is two to three folds greater than that observed in ZnTe and GaP crystals [157]. Furthermore, non-hygroscopic property of a BNA crystal makes it feasible to manipulate them with water [155].

So far, the large optical nonlinearity of BNA has been investigated by using the oriented-gas model [155, 156, 158]. This model is an intuitive method that predicts crystal polarization [72, 73] on the basis of a simple geometrical summation of the molecular polarizations where the intermolecular interactions are neglected. The oriented-gas model is an excellent model for the qualitative understanding on the mechanism that gives rise to the observed NLO properties. In fact, the previous studies on the optical nonlinearity of BNA were able to predict that the largest tensorial component of the quadratic optical nonlinearity (*d*-tensor) is d_{333}. Nonetheless the values of the *d*-tensor components of BNA have not been determined yet. Therefore the values of the *d*-tensor components should be determined in order to confirm the applicability of the oriented-gas model to the crystalline phase of BNA.

In this chapter, first, we describe the growth of a BNA single crystal. A large and optically transparent single crystal of BNA was grown with a vertical Bridgman method. For this, we use highly purified BNA that is obtained by applying a zone refining technique. Both zone refining and Bridgman method are well-known, cheap and practical methods, so that high quality BNA single crystals can now be readily produced. The crystal structure and the morphology of the BNA crystal will be investigated by means of X-ray diffraction techniques. Second, polarized reflection spectra of the crystal are measured in order to investigate the linear optical properties. The refractive index dispersion of each crystalline axis is determined by means of minimum deviation method. The precise determination of the refractive index is very important for the subsequent NLO measurements. Third, the magnitudes of all of the *d*-tensor components of the BNA crystal are determined by means of SHG Maker fringe method [136, 159] and phase-matching method. Consequently, the experimental value of d_{333} component is one of the largest value of the crystalline optical nonlinearity ever reported. Moreover the theoretical prediction based on the simple oriented-gas model fails to predict this very large optical nonlinearity. This discrepancy can be satisfactorily accounted for π-electron delocalization caused by the strong intermolecular interactions in the crystal. We show that the NLO properties of BNA are greatly influenced by the intermolecular interactions in the crystal.

5.2 Material preparation and its basic characterizations

5.2.1 Sample purification

Zone refining was applied to a raw BNA in order to further refine its purity. This involved four steps: (i) BNA (which was synthesized from MNA) was recrystallized from hot ethanol solution five times [155], (ii) it was melted and poured into a cleaned Pyrex tube (inner diameter = 6.6 mm, outer diameter = 10 mm, length = 18 cm), (iii) after the tube was evacuated sufficiently with a rotary pump, several freeze-and-thaw cycles were performed to reduce the levels of impurities [160] and the tube sealed, (iv) it was then subjected to zone refining with a horizontal-multizone furnace [161]. It should be noted that the Pyrex tube was cleaned through following processes: cleaned with detergent → rinsed with deionized water (RDIW) → immersed in 50 °C or 15 min→ immersed in methanol for 15 min → RDIW → immersed in 30 % solution of HCl for 30 min → RDIW → immersed in 30 % solution of HNO_3 for 30 min → RDIW → immersed in 30 % solution of Aqua regia for 30 min → RDIW → dried.

The furnace had 4 heaters which were arranged vertically every 4 cm. Each heater affording resistance of ∼ 5 Ω was made of nichrome line (diameter: 0.5 mm). The speed of the mobile heaters was controlled with a stepping motor set at 7 mm/h. Impurities in a sample tend to move into the liquid phase than into the solid one. Hence, impurities in the BNA moved towards the edge of the ampoule after repeated refining. A thermocouple linked to a temperature controller (Omron, E5AK) stabilized the temperature at 115 °C. The ampoule was rotated at 1.2 rpm about its axis to keep the melting parts 1–2 cm in length.

After 30 cycles of the zone refining procedure, yellow impurities were observed around the edge of the ampoule which indicated that impurities had indeed moved to the extremities of the sample. Finally, the sample was recrystallization from hot ethanol solution again. The thermal gradient gas-chromatography analysis (Shimadzu, GC-14B) using a non-polar capillary column (GL Science, TC-1: 15 m × 0.25 mm dia.) showed purity of greater than 99.99%.

5.2.2 Crystal growth

A single crystal of BNA was grown with a vertical Bridgman method. The zone-refined BNA was put in an ampoule, where the capillary was placed at the edge. The inner diameter of the ampoule was 8 mm. Again, as in the zone refining procedure, the ampoule was sealed after it was evacuated. The furnace has been described elsewhere [163]. Briefly, it had an upper heater, a lower heater, and an outer heater. Each heater was made of nichrome-line (diameter: 0.5 mm, upper: 90 Ω, lower: 70 Ω, outer: 90 Ω). The temperatures of the upper, lower, and outer heaters were maintained at 110, 97, and 90 °C, respectively. The speed of descent of the ampoule from the upper furnace to the lower one was 1 mm/h. After the

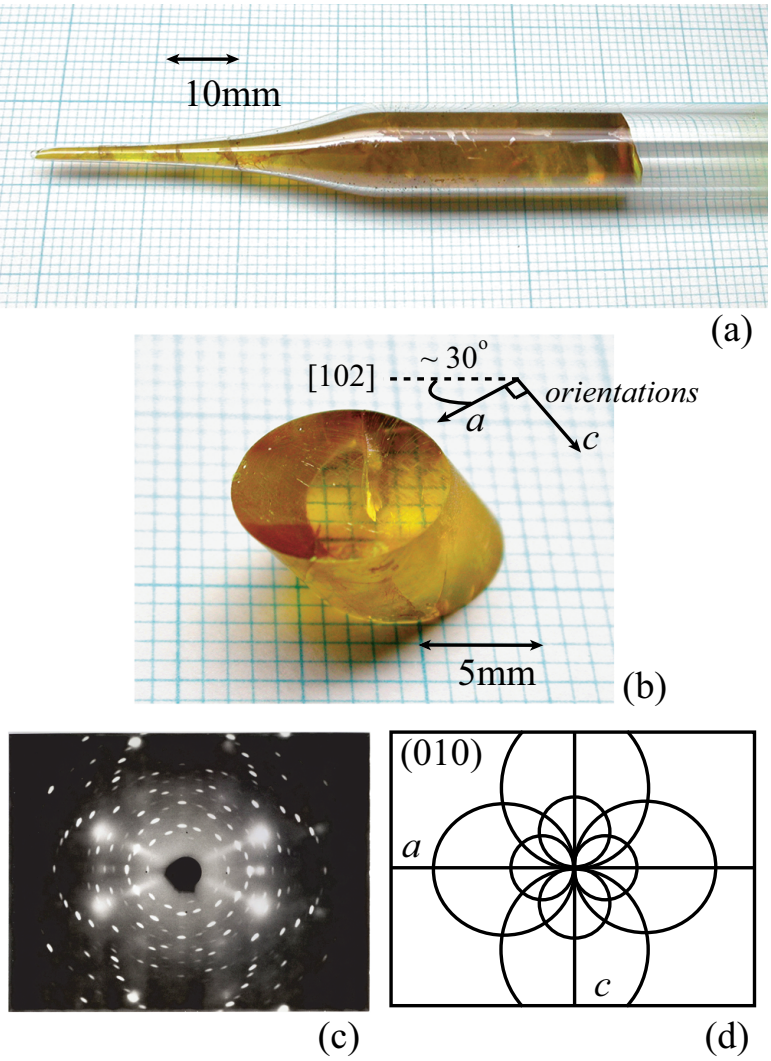

Figure 5.1: Photographs of the single crystal of BNA and its Laue pattern; (a) a view of the entire ampoule, (b) a part of the ingot whose length and diameter are 10 mm and 8 mm that was used for the analysis, (c) a Laue image of the cleavage plane and (d) a calculated Laue pattern derived from the crystalline parameters. The cleavage plane is (010), and the horizontal direction is [102]. The *a*-axis lies making 30° angle from the horizontal direction of the cleavage plane, and the *c*-axis lies 30° from the vertical direction of the cleavage plane. The horizontal direction in (c) and (d) is the *a*-axis and the vertical is the *c*-axis.

crystal growth was completed, the ampoule was slowly cooled to room temperature over a period of 7 days. Finally, a single crystal of 10 mm long by 8 mm in a diameter was obtained. Pictures of the crystal are shown in Figs. 5.1(a) and 5.1(b). A transmission spectrum of a 1-mm-thick plate cleaved from the crystal is shown in Fig. 5.2.

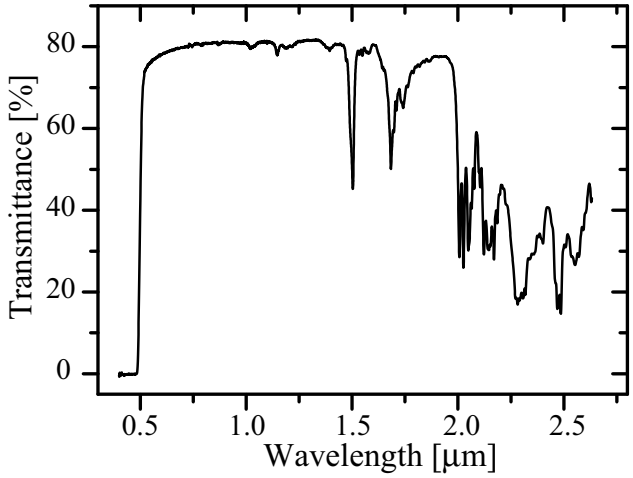

Figure 5.2: A transmission spectrum of a 1-mm-thick cleaved slab of BNA recorded at room temperature with non-polarized light.

5.2.3 Crystal orientations

Lattice orientations of the crystal were determined with the Laue method. A continuous X-ray beam was incident onto a cleavage plane of a thin (~ 0.5 mm) BNA plate sliced from the crystal. The transmitted Laue image was exposed onto a Polaroid film in order to determine the crystal orientations [163]. The Laue image on the film was compared with a Laue pattern calculated from the lattice parameters of BNA (see Table 5.1). The Laue image and the calculated pattern are shown in Figs. 5.1(c) and 5.1(d). The cleavage plane was determined to be the (010) plane. The *a*-axis is placed making ~30° with the horizontal direction of the cleavage plane. The diffraction spots did not show any streak lines, which indicates there are no serious internal structural defects.

5.2.4 Crystal structure determination

The diffraction spots of the BNA crystal was measured by using Rigaku AFC7/CCD Mercury. The crystal structure was solved by direct methods and was expanded using Fourier techniques (SHELX-97 and WinGX) [164]. Non-hydrogen atoms were anisotropically refined, while hydrogen atoms were isotropically refined. The crystal structure of BNA is shown in Fig. 5.3. The details of the crystal structure are as follows: a BNA crystal has *orthorhombic* lattice structure ($\alpha = \beta = \gamma = 90°$). Its space-group symmetry is $Pna2_1$, and the point symmetry is *mm2* (C_{2v}). The lattice parameters are $a = 7.390$, $b = 21.432$, and $c = 8.104$ Å. The molecular chains are formed by hydrogen-bonds between neighboring molecules along the [201] and the $[20\bar{1}]$ directions (hydrogen-bonded chains). The hydrogen bond existed between the amino-H of a molecule at (X, Y, Z) and the nitro-O of its neighbor at $(1/2+X, 1/2-Y, Z-1)$; the length of the hydrogen-bond is 2.487 Å. These molecular chains can be considered as supramolecular clusters that significantly enhance the optical nonlinearity as described in Section 5.4.

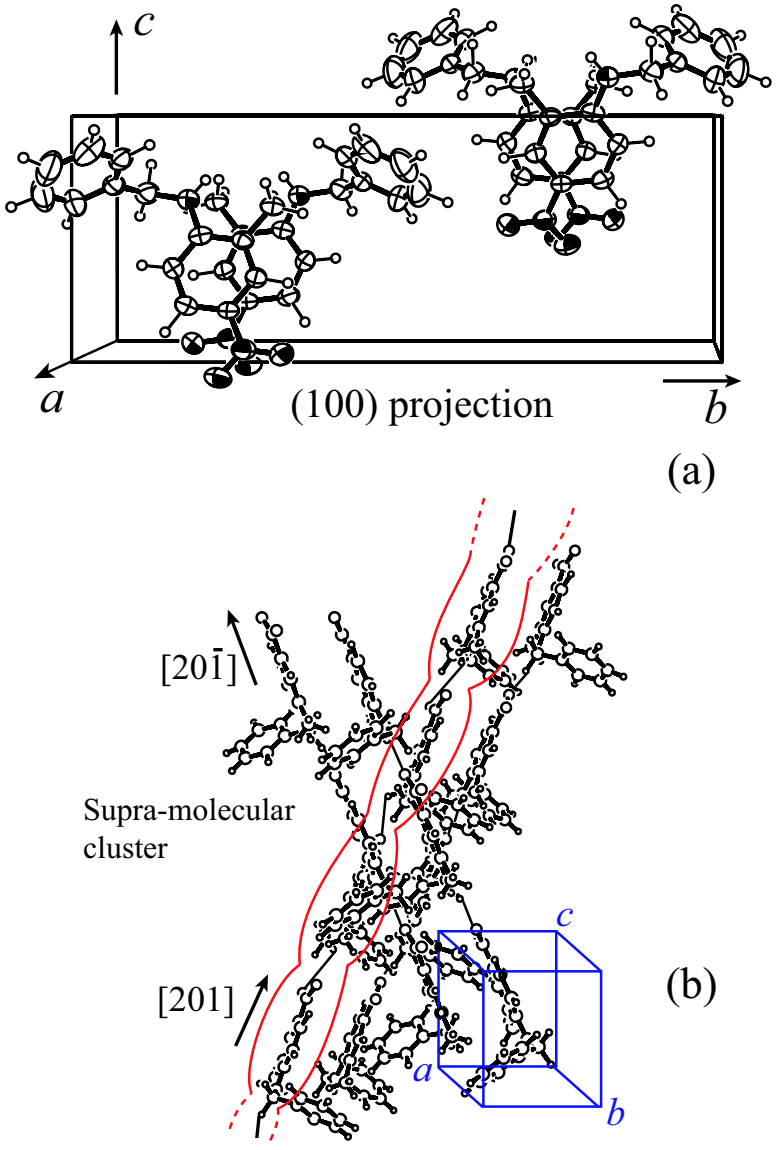

Figure 5.3: (a) An ORTEP view of a unit cell from the [100] direction. (b) Hydrogen-bonded chains along the [201] and the [20$\bar{1}$] directions.

5.2.5 Polarized reflection spectra

Method

Polarized reflection spectra of the cleavage plane of the BNA crystal were measured. Polarized absorption spectra were then obtained using Kramers-Kronig (KK) analysis from the measured reflection spectra. The sample crystal was prepared by cleaving one side of the BNA crystal. The other side was left untouched so that it had still retained the curved surface that corresponded to the inner curvature of the ampoule used for the Bridgman-growth process. The combination of flat and curved surfaces of the front- and back-sides of a crystal can avoid the effects of back- and multiple-reflections during the recording of reflection spectra. The cleavage plane of our BNA crystal is the (010) plane, hence it is possible to determine two polarized reflection spectra that are orientated along the *X*- and *Z*-axes of the crystal.

The collimated light from incandescent light sources was linearly polarized with a Glan-Thomson prism and irradiated onto the flat surface of the crystal with the polarizations parallel to the *X*- and *Z*-axes. For the light sources, we used a tungsten-halogen lamp for the measurements in the 400–1100 nm spectral region and a deuterium lamp for the 300–400 nm spectral region. The reflection spectrum was recorded using a photodiode-array detector (Otsuka Electronics, MCPD-1000). An MgF_2 coated aluminum mirror (Sigma Koki, TFA-20C05-10) was used as a standard of the reflectance. The mean incident angle was 1.86° and a wavelength-resolution of the measurements was ~ 2 nm.

Results

The polarized reflection spectra along the *X*- and *Z*-axes are shown in Fig. 5.4(a). Figure 5.4(b) shows their KK-transformed absorption spectra. The absorption spectrum of BNA molecules in *n*-hexane solution is also shown for comparison. The absorption spectra of the crystalline BNA differ from that of the solution in two ways: there is a large red-shift of the π-π^* transition energy and there is also a strong anisotropy in the absorption coefficients. The magnitude of the red-shift is approximately 0.7 eV. The energy of a Davydov splitting was determined to be 30 meV based on the comparison of the observed maximum absorption energies of the *X*- and *Z*-polarized absorption spectra [171]. A ratio of the intensity at the maximum absorption energy of the *Z*- and *X*-polarized absorption spectra is 4.2.

5.2.6 Determination of the refractive indices using minimum deviation method

Three prisms were prepared from the single crystal in order to determine the refractive indices. They were cut from the crystal, fixed into epoxy resin (Struers, Epofix), and subjected to water-based polishing using lapping films (Sumitomo 3M, 0.3–9 μm) and alumina powder (Struers, AP-D: 0.1 μm). The minimum-deviation method was employed to obtain the values of three refractive indices

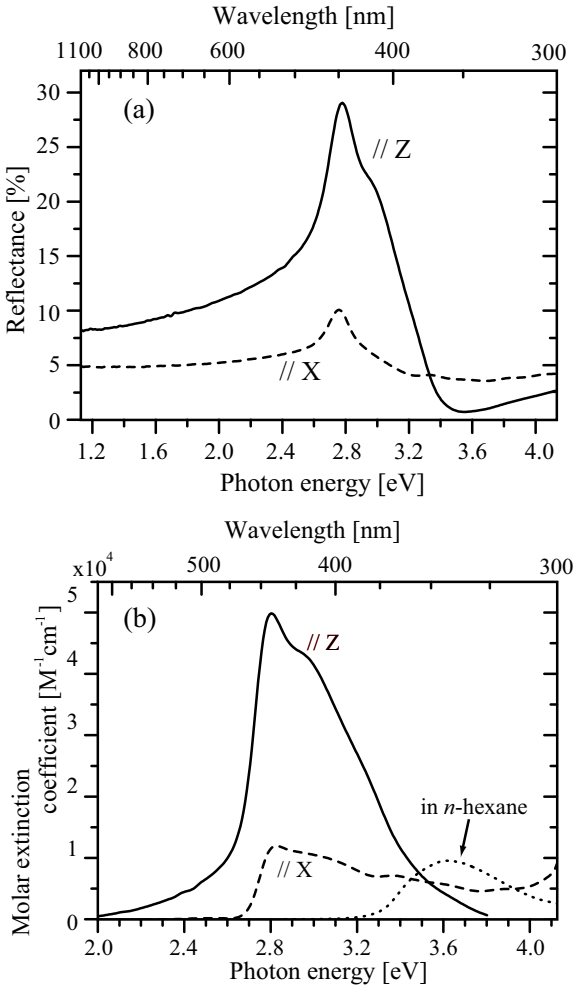

Figure 5.4: (a) Polarized reflection spectra of the single crystal of BNA. (b) Polarized absorption spectra which were obtained through KK analysis. //Z is a spectrum along the *Z*-axis (solid line), and //X along the *X*-axis (dashed line). An absorption spectrum of the BNA solution is also shown for comparison (dotted line).

of BNA. In this experiment, the resolution of the refractive indices was approximately 0.003. It should be noted that the minimum-deviation method gives the best precision of the refractive index in practice, although the dispersion of refractive index can be obtained from polarization reflection spectrum through KK analysis. Table 5.1 summarizes the refractive indices at various wavelengths with coefficients of a Sellmeier equation expressed by

$$n_I^2 = A + \frac{B}{\lambda^2 - C}. \tag{5.1}$$

nm	n_X	n_Y	n_Z
500	1.655	1.867	2.229
532	1.621	1.827	2.081
534.5	1.613	1.804	2.051
560	1.607	1.803	2.011
590	1.595	1.787	1.963
620	1.585	1.777	1.927
1064	1.558	1.717	1.798
Sellmeier coeff.	A	B	C
n_X	2.40481	0.02245	0.18254
n_Y	2.89766	0.05587	0.02245
n_Z	3.10611	0.12089	0.185

Table 5.1: Refractive indices of a single crystal of BNA along each dielectric axis in the visible to near-IR region and the coefficients of the Sellmeier equation expressed by Eq. (5.1).

5.3 Determination of the values of *d*-tensor components

5.3.1 Experimental procedures

Slab preparation

Two slabs, with surfaces corresponding to the (010) and (001) planes respectively, were prepared from the single crystal for the Maker-fringe measurements. The polishing scheme was basically the same as that described in Section 5.2.6, however, the slabs were not fixed into the resin. They were held by hand, which allowed us to prepare much flatter surfaces. The production of an optically flat (010) cleavage plane was required because scattering of the SH wave at the surface ruined the fringes. The (010) and (001) slabs were 273 μm and 225 μm thick, respectively. Transmittances of the slabs along each polarization axis were greater than 70%. The quality of each slab was investigated using the Laue method (crystal quality) and a polarization microscope (optical quality). These preliminary tests confirmed that the slabs were both crystallographically and optically well behaved. A direction normal to the face of the (001) slab makde an angle of 3.3° with the Z-axis. Therefore, the faces of the (001) slab actually corresponded to the (0,2,13) plane ($\theta = 3.3°$, $\phi = 90°$). In addition, we prepared a 750-μm-thick slab that was used for phase-matching measurement. The direction normal to the faces of this slab was $\theta = 72°$, $\phi = -18°$.

SHG Maker fringe method

The experimental setup for the SHG Maker-fringe measurement was basically the same as that used for the THG Maker-fringe measurement (see Fig. 4.2 at

page 49). Briefly, 1064 nm light from a Q-switched Nd:YAG laser (Continuum, Surelite I-20), with a repetition rate of 10 Hz and an energy of 60–400 μJ/pulse, was used for the fundamental input. The power of the light was controlled by neutral-density filters. Stray lights were removed from the laser beam by a color-glass filter. The beam was then linearly polarized using a Glan-laser prism (Sigma, GLP0-10-15AN) and was weakly focused ($f = 300$ mm) into the slab mounted on a rotation stage. The diameter of the beam at the slab was 50–100 μm. Polarization of the SHG was selected with a polarizing film (Sigma, SPF-30C-32) in order to determine a particular component of the *d*-tensor. Then, it was separated from the fundamental input with color-glass filters and a monochromator (Nikon, G-250). The SH wave was detected and measured using a photon-counting system (Hamamatsu; H7421-50, Stanford; SR400 and SR440).

d_{333} was determined using the (010) slab with *s*-*s* polarization configuration, and d_{311} was determined with the (010) and (001) slabs with *s*-*p* polarization. Theoretical formulae described in Ref. [137] (see Appendix D for the details of the derivations of the theoretical formulae) were used for the determination of the value of the *d*-tensor components. The SHG intensity derived from d_{333} can be expressed as

$$I(d_{333}) = A(d_{333})\left(\frac{2\cos\theta}{\cos\theta+\xi_3}\right)^4 \frac{\xi_8(\xi_3+\xi_8)(\cos\theta+\xi_3)}{(\cos\theta+\xi_8)^3(\xi_3^2-\xi_8^2)^2}\sin^2[k_1(\xi_3-\xi_8)L], \quad (5.2a)$$

where

$$\xi_3 = \sqrt{(n_Z^\omega)^2-\sin^2\theta}, \quad \xi_8 = \sqrt{(n_Z^{2\omega})^2-\sin^2\theta}. \quad (5.2b)$$

In the same way the SHG intensity derived from d_{311} can be expressed as

$$\begin{aligned} I(d_{311}) =& A(d_{311})\left(\frac{2\cos\theta}{\cos\theta+\xi_3}\right)^4 \cos^2\theta\sin^2\theta \\ &\times \frac{\varepsilon_Y^{2\omega}}{(\varepsilon_Z^{2\omega})^2}\frac{\xi_9(\xi_3+\xi_9)(\xi_3+\cos\theta\varepsilon_Y^{2\omega})}{(\xi_9+\cos\theta\varepsilon_Y^{2\omega})^3(\xi_3^2-\xi_9^2)^2}\sin^2[k_1(\xi_3-\xi_9)L], \end{aligned} \quad (5.3a)$$

where

$$\xi_3 = \sqrt{\varepsilon_X^\omega-\sin^2\theta}, \quad \xi_9 = \sqrt{\frac{\varepsilon_Y^{2\omega}}{\varepsilon_Z^{2\omega}}(\varepsilon_Z^{2\omega}-\sin^2\theta)}. \quad (5.3b)$$

Here, A, θ, and n_I^ω are proportional coefficient, incident angle, and refractive index of I-axis at frequency ω, respectively. The above equations were fitted to the experimental data. Then the obtained A values of BNA's d_{333} and d_{311} were determined against to A values of standard materials that was independently determined. In order to calibrate these measurements the following standards were used: $d_{333} = 14.6 \pm 0.7$ (pm/V) of Y-cut KTP (thickness: 0.75 mm, Crystech) for the determination of d_{333} and d_{311} [the (010) slab] of BNA [165]; $d_{111} = 0.3$ (pm/V) of Y-cut Quartz (thickness: 2.05 mm, Hikari Kobo) for the determination of d_{311} of BNA in the case of the (001) slab [166]. Since the SHG generated by d_{311} of BNA by using the (010) slab was very weak, it was not possible to compare

it to d_{333} of KTP because the photon-counting was not in the linear range. Therefore, in that case we used d_{111} of Quartz as a standard. Since the phase-matching condition was satisfied in the vicinity of the direction normal to the face of (001) slab, it was not possible to determine d_{322} of BNA with the Maker-fringe method. A phase-matching measurement was therefore used to determine d_{322}.

SHG phase-matching method

The phase-matching method was used in order to determine the value of d_{322} by comparing it to $d_{eff}^{\mathrm{BBO}} = 2.0$ (pm/V) of a BBO crystal (thickness: 13 mm, Crystech) in Type I phase-matching geometry. The experimental setup was basically the same as that used in the SHG Maker-fringe measurements, but a precision-power meter (Advantest, TQ8210 and TQ82014) was used for the detection of the SH power. In addition, a non-focused beam was used to avoid the effects of walk-off mismatch. Following Ref. [136], d_{322}^{BNA} of BNA can be expressed as

$$(d_{322}^{\mathrm{BNA}} \times \sin\theta_{pm}^{\mathrm{BNA}})^2 = \frac{P_{\mathrm{BNA}}^{2\omega}}{P_{2\mathrm{BBO}}^{\omega}} \frac{\left[n_{\mathrm{BNA}}^{\omega}(\theta_{pm}^{\mathrm{BNA}})+1\right]^2 \left[n_{\mathrm{BNA}}^{2\omega}(\theta_{pm}^{\mathrm{BNA}})+1\right]}{\left[n_{\mathrm{BBO}}^{\omega}(\theta_{pm}^{\mathrm{BBO}})+1\right]^2 \left[n_{\mathrm{BBO}}^{2\omega}(\theta_{pm}^{\mathrm{BBO}})+1\right]} \left(\frac{L_{\mathrm{BBO}}}{L_{\mathrm{BNA}}}\right)^2 \left(d_{eff}^{\mathrm{BBO}}\right)^2, \quad (5.4)$$

where $P^{2\omega}$, $n^{\omega}(\theta_{pm})$, and L are SHG output power, refractive index for fundamental wavelength ω at phase-matching angle θ_{pm}, and thickness of slab, respectively.

5.3.2 Results

Figure 5.5 shows typical fringes derived from d_{333} and d_{311}, together with fringes in the reference crystals. The SH intensity arising from d_{333} produced clear interference patterns as shown in Fig. 5.5(a). These were fitted by the theoretical formulae using the parameters of the normal incident angle θ_0 and the d-tensor component. The refractive indices determined in this study were used following parameterization including errors in order to obtain the best fit. This actually does not affect the magnitude of the d-tensor components in the region far from the phase-matching angle. The experimentally determined d-tensor values are summarized in Table 5.2. In Fig. 5.5(a), the fringes have nonzero-minima. This is mainly caused by the two faces of the slab not being perfectly parallel to each other. Since the coherence lengths in BNA crystals are very short, even small deviations from parallel of the surfaces will result in destructive effects on the interference patterns. At present, it is impossible to obtain zero minima due to difficulty in crystal polishing. The SH intensity arising from d_{311} did not produce an interference pattern in either of the two slabs, as shown in Fig. 5.5(b). They also showed no dependence on the rotation angle. The origin of this lack of angular dependence is not fully understood, but may be due to the strain-induced scatterings of the SH arising from d_{333}. The SH arising from d_{311} cannot be detected even when an intense pump field is applied. If the SH intensities were generated by d_{311}, then the observed SH intensities give an inconsistent result: namely the SH

Maker-fringe method	
d_{333}	234 ± 31 (pm/V)
d_{311}	negligible
Phase-matching method	
d_{322}	15.6 ± 0.9 (pm/V)
Phase-matching angle	
$\varphi = 0°$,	$\theta = 26.9°$ experimental
$\varphi = 0°$,	$\theta = 32°$ calculated

Table 5.2: The values of *d*-tensor components of a BNA single crystal. The experimental and calculated phase-matching angles are also listed.

intensity observed from the (010) slab corresponds to $d_{311} = 159$ (pm/V), whereas that from the (001) slab corresponds to $d_{311} = 53$ (pm/V). Therefore, we conclude that the magnitude of d_{311} is very small and so the *flat* SHG has a different origin.

Figure 5.5(c) shows the SH intensity derived from d_{322} as a function of rotation angle in the phase-matching condition. We measured the SH power at its peak position and compared that to the phase-matched SH power produced by a BBO crystal using the equation described in Ref. [136]. The results of the phase-matching measurement are summarized in Table 5.2. One can estimate the experimental error of the measured refractive indices from the deviation between $\theta_{\rm pm}$ determined by experiment and its value calculated from the refractive indices determined here. This deviation of $\Delta\theta_{\rm pm} = 5.1°$ corresponds to an error in the refractive index at the phase-matched angle of $\Delta n = 0.028$.

The value of d_{333} is very large as a yellow-colored NLO material. It is 1.27 times larger than $d_{111} = 184$ (pm/V) of 2-methyl-4-nitroaniline (MNA), and is the *highest value* so far determined for any yellow-colored material [136, 168]. It should be noted that Levine *et al.* reported $d_{111}(\text{MNA}) = 500 \times d_{111}(\text{Quartz})$ and $d_{111}(\text{MNA}) = 40 \times d_{311}(\text{LN})$ in Ref. [167]. Here, LN denotes Lithium Niobate. We adopted the latter expression $d_{111}(\text{MNA}) = 40 \times d_{311}(\text{LN})$ and the updated value $d_{311}(\text{LN}) = 4.6$ (pm/V) [165], so that we can make more accurate comparison of the *d* values.

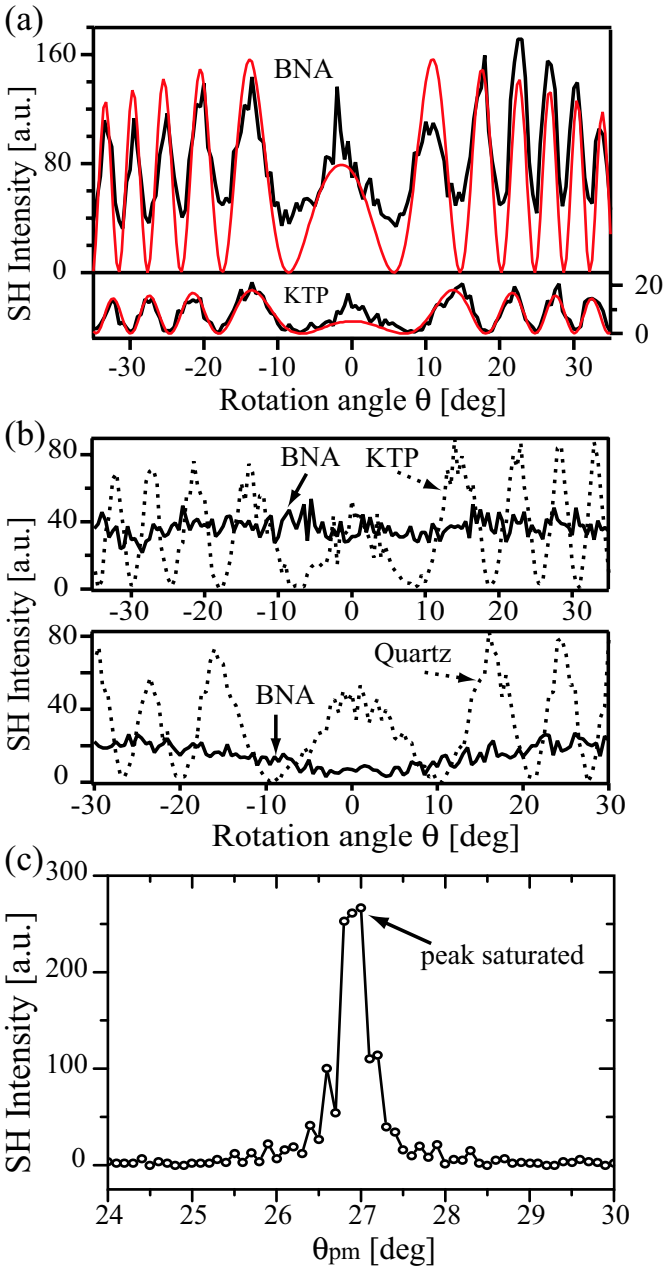

Figure 5.5: (a) Maker-fringes observed for the (010) slab of BNA (upper panel) and those from KTP crystal (lower panel). Black solid lines show experimental results and red solid lines show the results of fitting. These fringes of BNA are arisen from the d_{333} tensor component of the crystal. (b) SHG observed by using the (010) slab [upper] and the (001) slab [lower] of BNA. In these optical configuration SH arisen from the d_{311} tensor component of the BNA crystal should be observed. Dotted line in the upper panel shows the fringes obtained using KTP, while that in the lower panel using Quartz. SHG observed using the BNA slabs are shown by solid lines. (c) SHG angle tuning curve of the type I phase-matched BNA crystal. Note that signal from this detector (photon counter) was saturated at the peak.

5.4 Discussion: Theoretical predictions of the *d*-tensor components based on the oriented-gas model

5.4.1 Orientation of a BNA molecule in the crystal

Theoretical predictions of the *d*-tensor components based on the oriented-gas model have been performed with incorporating intermolecular interactions in the crystal. Before that, we first express the orientation of a BNA molecule in the crystalline axis coordinate.

Supposing that a molecule of BNA has a two-dimensional structure, the orientation of the molecule can be fully expressed using following three parameters, α, Φ, and θ as shown in Fig. 5.6. The parameter θ is calculated using an electric-dipole vector of the molecule ($\boldsymbol{\mu}$) with its 2-fold symmetric neighbor ($\boldsymbol{\mu}_{\mathbf{symm}}$). The other two parameters (α and Φ) are obtained from following equations,

$$\begin{aligned} \cos 2\theta &= \frac{\boldsymbol{\mu}\cdot\boldsymbol{\mu}_{\mathbf{symm}}}{|\boldsymbol{\mu}|^2},\ \cos\alpha = \frac{\mu_Z}{|\boldsymbol{\mu}|\cos\theta}, \\ \sin\Phi &= \frac{1}{|\boldsymbol{\mu}|}\frac{\mu_X\sin\alpha\cos\theta - \mu_Y\sin\theta}{(\sin\alpha\cos\theta)^2 + \sin^2\theta}, \end{aligned} \tag{5.5}$$

where μ_X, μ_Y, and μ_Z are described with Cartesian coordinates located within the unit cell. Analysis of the crystallographic data of BNA reveals that $\alpha = 21.9°$, $\Phi = 90°$, and $\theta = 22.5°$.

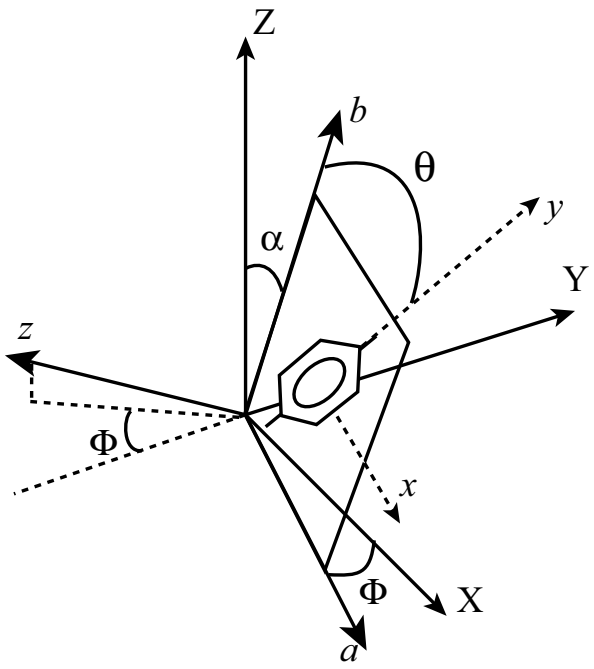

Figure 5.6: A schematic view of a molecule in the crystal and the definitions of the parameters α, θ, and Φ.

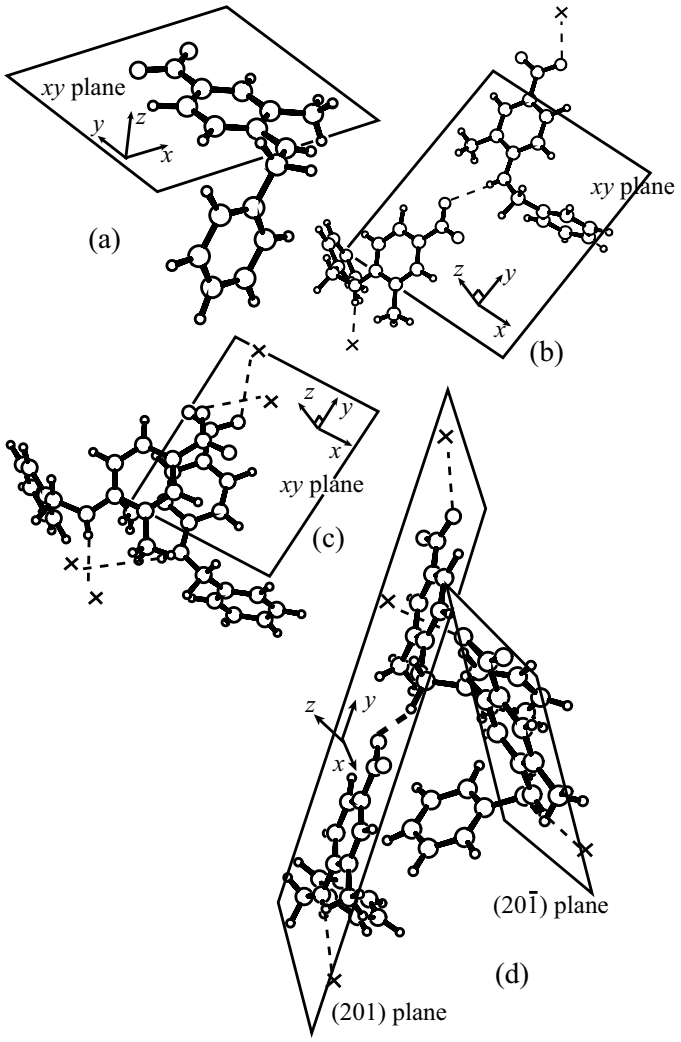

Figure 5.7: Arrangement of the molecular axes of (a) the monomer, (b) h-dimer, (c) p-dimer, and (d) trimer.

5.4.2 Intermolecular interactions and supramolecular approach

The values of the *d*-tensor components predicted with the simple oriented-gas model are summarized in Table 5.3 (this is the case of *Monomer*). We clearly see the large discrepancy of the d_{333} value between the prediction and the experiment. This large discrepancy can be accounted for the electron delocalization spreading over several molecules, which is caused by strong intermolecular interactions in the BNA crystal. In particular, we focus on the effect of hydrogen bonds that exist in the crystal because several papers reported that hydrogen bonds enhance the optical nonlinearity of organic NLO crystals [42–47].

Figure 5.2 (b) shows hydrogen-bonded chains as solid lines connecting two neighboring BNA molecules. In order to include intermolecular interactions (particularly hydrogen-bond interactions), these chains are regarded as quasi-one-dimensional supramolecular clusters (such a chain can be also envisaged as a

three-dimensional network in crystals of MNA [172]). We assume that π-electrons spread over several molecules, therefore, these molecules are regarded as a supramolecular cluster. The range of electron delocalization can be limited within several molecules due to the intrinsic nature of molecular crystals that π-electrons are basically localized at each molecule. The intermolecular interactions included in the calculations were along the three orthonormal directions: (i) along the axis of the hydrogen-bonded molecular chain, (ii) between the π-π stacked chain and (iii) between the chains along the [201] and the [20$\bar{1}$] directions, which were separated by at least 10 Å. The different molecular interactions of the BNA molecules within the crystal lattice resulted in three oligomeric states termed h-dimer, p-dimer and trimer (Fig. 5.7).

The hyperpolarizabilities of these oligomers were used in the subsequent *d*-tensor calculations. The semiempirical computing method INDO/S-CI was applied to the three oligomers in order to calculate their first hyperpolarizabilities, β. These calculations were operated by using the MOS-F program (Fujitsu). It is well-known that the INDO/S-CI method predict the optical properties of organic molecules quantitatively [173]. In fact, the theoretically predicted absorption spectrum of BNA is in excellent agreement with the experimental one [see Fig. 5.8 (a)]a. In the calculations we used standard parameters and weighting factors for the orbital overlap of $f_\sigma = 1.267$ and $f_\pi = 0.585$ [174]. The configuration interactions were calculated with the 10 lower-lying occupied orbitals from the highest occupied molecular orbital (HOMO) and with the 10 higher-lying virtual orbitals from the lowest unoccupied molecular orbital (LUMO). The mathematical expressions of the hyperpolarizabilities in frequency domain expression is described elsewhere [138,175] (Note that the time-domain expressions are described in Section 2.1.) The molecular axes of the oligomers were taken to be those as shown in Fig. 5.7; the molecular *x*-axes of the oligomers are along the crystalline *Y*-axis of BNA and the *y*-axes are set at 24.5° with the *Z*-axis. Hence we have $\alpha = 24.5°$ and $\Phi = \theta = 0°$. These oligomers have nearly no molecular symmetry (point group: C_1), therefore, the *b*-tensor (*b-tensor is quadratic nonlinearity of the unit cell per molecule* [73]) is expressed by

$$\begin{aligned} b_{333} &= \beta_{yyy}\cos^3\alpha + 3\beta_{yzz}\sin^2\alpha\cos\alpha \\ &\quad + 3\beta_{zyy}\cos^2\alpha\sin\alpha + \beta_{zzz}\sin^3\alpha, \\ b_{311} &= \beta_{yyy}\sin^2\alpha\cos\alpha - 3\beta_{yzz}\sin^2\alpha\cos\alpha \\ &\quad - 3\beta_{zyy}\cos^2\alpha\sin\alpha + \beta_{zzz}\cos^2\alpha\sin\alpha, \\ b_{322} &= \beta_{yxx}\cos\alpha + \beta_{zxx}\sin\alpha, \end{aligned} \tag{5.6}$$

where $\boldsymbol{d} = f \cdot N_{\text{oligomer}}\,\boldsymbol{b}$, and the crystal *X*-, *Y*-, and *Z*-axes are simply denoted 1, 2, and 3, respectively. $N_{oligomer}$ is the number density of the oligomers, which are listed in Table 5.3. The term f is a local field correction factor, however, it can be neglected as the intermolecular interactions are included into β.

The calculated absorption line spectra of the oligomers are shown in Fig. 5.8. The energies of the π-π^* transitions of the oligomers look similar to that of monomer

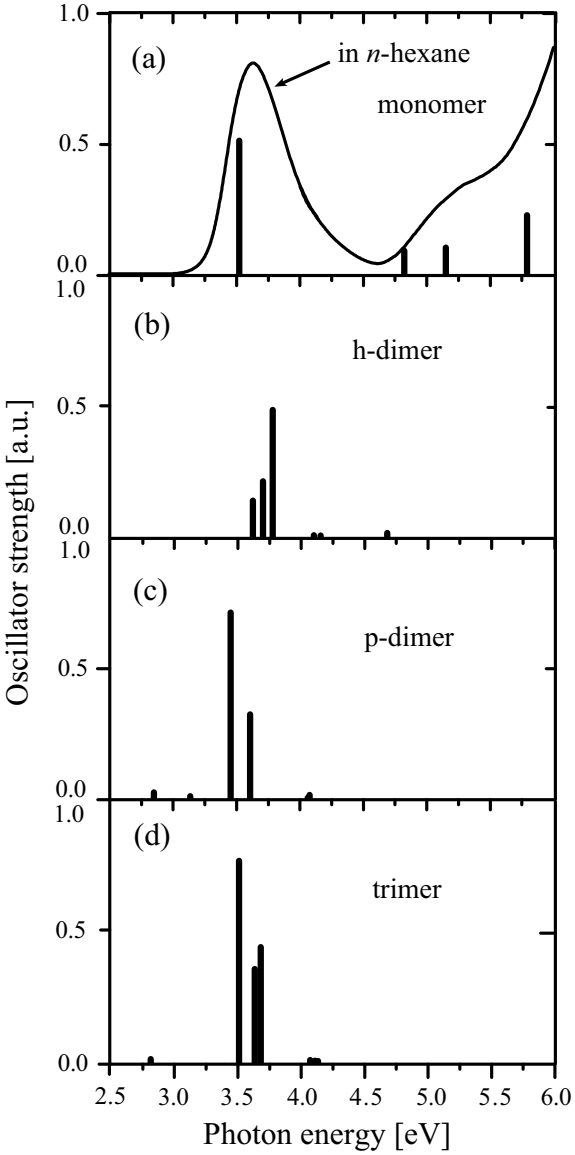

Figure 5.8: (a) The absorption spectrum of the monomeric BNA calculated with INDO/S-CI method (histograms) and the normalized absorption spectrum of BNA in *n*-hexane solution (solid line). The calculated absorption spectra of (b) h-dimer, (c) p-dimer, and (d) trimer of BNA are also shown with histograms.

and do not correspond to those experimentally determined in the crystal [Fig. 5.4(b)]. The energy of the π-π^* transition in the crystalline phase is red-shifted by 0.7 eV in comparison with those calculated for the oligomers using the INDO/CI method. Taking into account the molecular exciton theory this is interpreted as an on-site energy (site-shift) which is caused by an excited molecule in the crystal interacting with the surrounding steady-state molecules [171]. The large site-shift energy (0.7 eV) clearly shows that the effect of intermolecular interactions in a BNA crystal is significant.

Component	Monomer	H-dimer	P-dimer	Trimer	Experimental
β_{xxx}	0.67	-0.41	-4.00	-0.11	
β_{yyy}	-37.04	-70.36	-39.56	-78.65	
β_{zzz}	—	0.33	-0.182	-10.97	
β_{xyy}	-1.53	0.82	-3.78	-6.40	
β_{yxx}	2.90	-12.00	-7.52	-15.75	
β_{xzz}	—	0.03	-0.01	-6.94	
β_{yzz}	—	0.22	-0.24	-10.76	
β_{zxx}	—	-0.36	0.14	-3.01	
β_{zyy}	—	-4.15	-0.15	-13.76	
$\|\|\beta\|\|$	37.10	70.02	39.29	78.34	
$N_{\text{oligomer}} \times 10^{21}$	3.116	1.558	1.558	1.039	
d_{333}	99.72	134.78	70.70	124.16	234 ± 31
d_{322}	16.06	15.30	14.04	4.93	15.6 ± 0.9
d_{311}	20.30	21.28	12.38	19.98	~ 0

Table 5.3: The hyperpolarizabilities β (10^{-30} esu $\cdot$ cm^{-5}) of the monomer, h-dimer, p-dimer and trimer, together with the resulting d-tensor components (pm/V). Each calculated value is at the energy of the fundamental input of 1064 nm. The numbers of the molecules used in the calculations of the d-tensor components are normalized ($N_{\text{monomer}} = 3.116 \times 10^{21}$, $N_{\text{dimer}} = N_{\text{monomer}}/2$, and $N_{\text{trimer}} = N_{\text{monomer}}/3$). Note that the resonance-correction factor was applied to the d-tensor following Eq. (5.8), but not to β-tensor.

Theoretical prediction of the on-site energy is a difficult task because all the electrons in the system are required to be incorporated into the calculations [171]. The on-site energy is usually treated as a phenomenological parameter even in the relatively simple case, such as anthrathene [171]. Therefore, we incorporated this effect into the calculations of the hyperpolarizability of the oligomers by introducing a resonance-correction factor. The introduction of the resonance-correction factor, which uniformly affects all possible transitions, is justified by the fact that the optical nonlinearity of the BNA crystal can be accounted for only the lowest optically allowed π-π^* transition, in practice. For this reason, it is sufficient to take account of simple one factor that corresponds to the correction factor for one of four terms in the SHG nonlinear process (see Fig. 2.2 in page 15).

$$C = \frac{(\omega_{\text{p}} - \omega_{\text{calc}})(2\omega_{\text{p}} - \omega_{\text{calc}})}{(\omega_{\text{p}} - \omega_{\text{exp}})(2\omega_{\text{p}} - \omega_{\text{exp}})}, \tag{5.7}$$

where ω_{p}, ω_{calc}, and ω_{exp} are, the frequency of pump light (1064 nm wavelength), the calculated π-π^* transition frequency, and the experimentally determined π-π^* transition frequency, respectively. Here, the correction factor C was calculated to be 3.6. The values of $\hbar\omega_{\text{p}} = 1.1644$ eV, $\hbar\omega_{\text{calc}} = 3.5$ eV, and $\hbar\omega_{\text{exp}} = 2.8$ eV were used for the resonance-correction. The final form to determine the values of the individual d-tensor components can be expressed by

$$\boldsymbol{d} = C \cdot f \cdot N_{\text{oligomer}}\, \boldsymbol{b}. \tag{5.8}$$

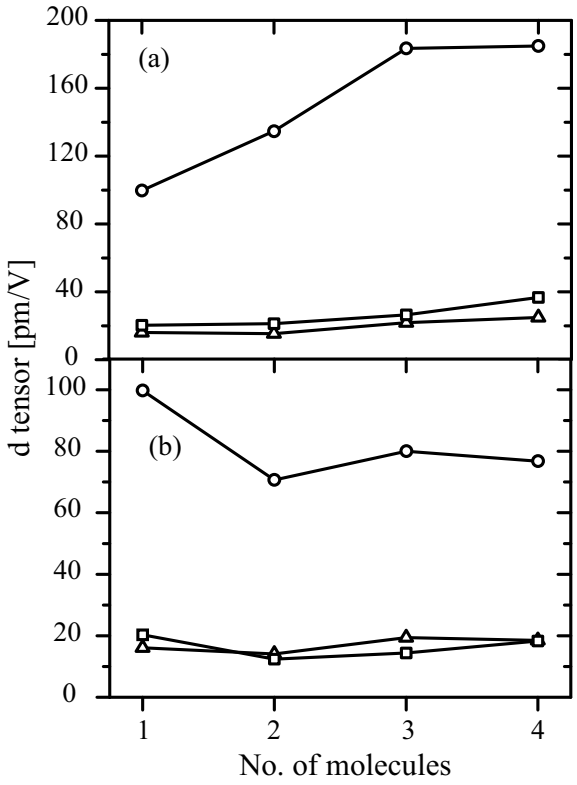

Figure 5.9: The dependencies of the magnitudes of the *d*-tensor components as function of the number of constituent molecules in the (a) h- and (b) p-oligomeric states. The symbols ∘, □, and △ represent the d_{333}, d_{322}, and d_{311} components, respectively.

Table 5.3 summarizes the results of the calculations of the molecular hyperpolarizabilities and the *d*-tensors of the supramolecules (oligomers). The values of the *d*-tensor components of the h-dimer, p-dimer and trimer supramolecules are significantly different, compared to those of the monomeric molecule. In the h-dimer, d_{333} increases while d_{311} decreases, whereas in the p-dimer the values of all the components are reduced somewhat. In the trimer d_{311} decreases despite the fact that the molecules along the [201] and the [20$\bar{1}$] directions are separated by at least 10 Å.

The absolute values of β_{yxx} and β_{zyy} in the h-dimer are enhanced compared to those observed in the monomer. According to Eq. (5.6), β_{yxx} mainly contributes to d_{322} and β_{zyy} increases d_{333} but diminishes d_{311}. The increase of $\|\beta_{yxx}\|$ derives from the dipoles of the two constituent molecules that do not align along the same direction (staggered configuration [176]). The enhancement of $\|\beta_{zyy}\|$ originates from the fact that the molecules are connected to each other by hydrogen-bonds. In the p-dimer the staggered configuration also induces perturbations of all of the components of the β-tensor (β_{xxx}, β_{yyy}, β_{xyy}, and β_{yxx}). The intermolecular interactions in the trimer obviously enhance the components of the β-tensor where the suffix z is denoted. In particular, β_{zyy} and β_{zxx} increase d_{333} and reduce d_{311}. In contrast, d_{322} is not affected as it does not depend on either β_{zyy} or β_{zxx}.

In order to further characterize the three d-tensor components in the h- and p-oligomeric states the number of correlated molecules in the supramolecules was varied in the calculations described above. Figure 5.9(a) shows that the magnitude of d_{333} increases up to 200 pm/V in the h-oligomeric state as the number of constituent molecules increases. Such behavior can be explained by the fact that the oscillator strength of the π-π^* transition is increased as the number of molecules increases [see Fig. 5.8(b) for the case of h-dimer] [45]. In contrast, interactions in the p-oligomeric state does not greatly affect the magnitude of the d-tensor components, except at the first dip of d_{333} when changing from a monomer to a dimer [Fig. 5.9(b)]. This indicates that the intermolecular interactions along the π-stacking direction are sufficiently incorporated with a dimeric state. Thus our supramolecular model have successfully accounted for the large enhancement of the optical nonlinearity of the BNA crystals.

From the above modeling studies we conclude that (i) the interactions in the h-oligomeric and trimer supramolecular clusters greatly enhance the d_{333} component, (ii) the interactions between π-stacked molecules very slightly affects the magnitude of the d-tensor components.

5.5 Summary

A single large crystal (8 mm diameter $\times$ 10 mm long) of BNA with good optical transparency has been grown with the Bridgman method. The morphology and the structure of the crystal were analyzed by the X-ray diffraction analyses. The basic optical properties of the crystal, including the polarized reflection spectra and the dispersion of the refractive indices, were determined. Three d-tensor components of the crystal have been determined for the first time by means of a combination of the Maker-fringe technique and the phase-matched method. These were $d_{333} = 234 \pm 31$, $d_{322} = 15.6 \pm 0.9$, and $d_{311} \sim 0$ (pm/V). We have found that the value of d_{333} is the highest value so far determined for any yellow-colored NLO material. The theoretical predictions of the values of the d-tensor components were performed on the basis of the oriented-gas model, where the strong hydrogen-bond intermolecular interactions are incorporated. The theoretical predictions were in good agreement with the experimental values, when we further included the resonance effect that came from the 0.7 eV red-shift of the π-π^* transition in the crystalline phase. We thus propose that the very large enhancement of d_{333} is due to the significant interactions along the hydrogen bonds and its consequent resonance enhancement.

Chapter 6

Conclusions

This dissertation have intensively focused on how the optical response of the artificial π-conjugated systems are affected by the systematic change of their structure. In particular, we have shown how one can describe the optical polarization of any types of π-conjugated molecular systems with a unified manner of physics. Now, we are ready to show the general overview of this particular issue.

1. The works of TG and THG spectroscopy on β-carotene homologues have demonstrated that any types of the third-order NLO responses of the π-conjugated molecules can be satisfactorily described with the unified manner of the time-dependent perturbation theory and the multimode Brownian oscillator model. Furthermore, we have found the characteristic optical response of π-conjugated molecules, which varies depending on the extent of π-electron delocalization. One is that the photoexcitation energy in the π-conjugated molecules is selectively dissipated through the specific molecular vibrations (the C=C stretching mode), as the size of the molecular system decreases. Another is that the third-order optical nonlinearity for the THG process is greatly enhanced as the range of the π-electron delocalization is enlarged.

2. The work of BNA have first determined the magnitude of the optical nonlinearity of the BNA crystal and clarified the mechanism of that large second-order optical nonlinearity. The value of d_{333} was determined to be 234 ± 31 (pm/V), which is one of the largest values of second-order optical nonlinearity ever reported. We have proposed that the very large enhancement of d_{333} is caused by the significant interactions along the hydrogen bonds and its consequent resonance enhancement. The most important point of this work is that the supramolecular approach is proved to be very effective in predictions of second-order NLO π-conjugated molecular crystals.

Finally, we would like to close this dissertation with a brief summary on the unified theoretical descriptions of the optical response, which we have demonstrated through this book. The essence of the physics that describes optical response of matter can be understood by considering the linear optical response

function [see Eq. (2.50) on page 21], which is given by

$$J(t_1) = |\mu_{eg}|^2 \exp\left(-i\omega_{eg}t_1\right) \exp\left[\left(-\frac{i}{\hbar}\right)^2 \int_0^{t_1} d\tau_2 \int_0^{t_2} d\tau_1 \langle U(\tau_2)U(\tau_1)\rho_g\rangle_c\right].$$

The second exponential part in this equation is the one that we have intensively discussed in this dissertation, which shows the environmental contributions to the optical transition. These environmental contributions are able to be described by means of displaced harmonic oscillator Hamiltonian, *i.e.* multimode Brownian oscillators. The environmental contributions include molecular vibrations, chromophore-solvent interactions, and stochastic Gaussian (static) interactions. Evaluation of μ_{eg}, and ω_{eg} of carotenoids have not fully described in this dissertation because the effect of strong electron correlation (or configuration interaction) should be taken into account in order to properly predict the values of μ_{eg} and ω_{eg}. The strong electron correlation (or configuration interaction) in π-conjugated system is a current hot topic in the condensed matter physics [178–180]. It is beyond the scope of the present dissertation. However, the supra-molecular approach used in Chapter 5 is one possible method that predicts the proper values of μ_{eg} and ω_{eg} in case that several molecules form a supra-molecular cluster in the crystal. The supra-molecular approach indeed has succeeded in incorporating the environmental effects into the predictions of the value of μ_{eg}.

Appendix A

Mathematical techniques frequently used in this book

A.1 Liouville-space notation

Wavefunction plays a central role in quantum mechanics in Hilbert space. On the other hand, it is density matrix that has the same role in Liouville space. The density matrix formalism simplifies the theoretical formalism of the light-matter interaction processes, so that the density matrix formalism has been frequently used

Object	Hilbert space	Liouville space
State of system (ket)	$\|\psi\rangle$	$\|\rho\rangle\rangle$
Hermitian conjugated (bra)	$\langle\psi\| \equiv (\|\psi\rangle)^\dagger$	$\langle\langle\rho\| \equiv (\|\rho\rangle\rangle)^\dagger$
Basis set	$\|n\rangle$	$\|nm\rangle\rangle$
Orthogonality	$\langle n\|m\rangle = \delta_{nm}$	$\langle\langle jk\|nm\rangle\rangle = \delta_{kn}\delta_{jm}$
Unit operator	$1 = \sum_n \|n\rangle\langle n\|$	$I = \sum_{n,m} \|nm\rangle\rangle\langle\langle nm\|$
Scalar product	$\langle\psi\|\phi\rangle$	$\langle\langle A\|B\rangle\rangle$
Expansion of a vector	$\|\psi\rangle = \sum_n \|n\rangle\langle n\|\phi\rangle$	$\|A\rangle\rangle = \sum_{n,m} \|nm\rangle\rangle\langle\langle nm\|A\rangle\rangle$
Linear equation	$\sum_m A_{nm}\psi_m = \phi_n$	$\sum_{j,k} \mathscr{L}_{nm,jk}A_{jk} = B_{nm}$
Equation of motion	$\|\dot{\psi}\rangle = -\frac{i}{\hbar}H\|\psi\rangle$	$\|\dot{\rho}\rangle\rangle = -\frac{i}{\hbar}\mathscr{L}\|\rho\rangle\rangle$
Matrix element	H_{nm}	$\mathscr{L}_{nm,jk} = H_{nj}\delta_{nj} - H^*_{mk}\delta_{mk}$
The time evolution operator*	$\|\psi(t)\rangle = U(t,t_0)\|\psi(t_0)\rangle$	$\|\rho(t)\rangle\rangle = \mathscr{U}(t,t_0)\|\rho(t_0)\rangle\rangle$
Green functions (Time domain)	$G(t-t_0) =$	$\mathscr{G}(t-t_0) =$
	$\theta(t-t_0)\exp[-\frac{i}{\hbar}H(t-t_0)]$	$\theta(t-t_0)\exp[-\frac{i}{\hbar}\mathscr{L}(t-t_0)]$

Table A.1: Comparison of the Liouville and the Hilbert space notations. Cited from Ref. [50]. * The time evolution operator is defined in Section A.2.

in Chapter 2. We will summarize the Liouville-space notation. One can change the Hilbert-space notation to the Liouville-space notation by simply referring to Table A.1.

A.2 Time-ordered expansion technique

The state of the density matrix after n times photon interactions are well understood using time-ordered expansion technique. First, we define the Liouville-space propagator as

$$\rho(t) \equiv \mathscr{U}(t, t_0)\rho(t_0). \tag{A.1}$$

The quantum Liouville equation in Eq. (2.5) on page 12 is expressed using Eq. (A.1),

$$\frac{\partial \mathscr{U}(t, t_0)}{\partial t} = -\frac{i}{\hbar}\mathscr{L}(t)\mathscr{U}(t, t_0), \tag{A.2}$$

with the initial condition

$$\mathscr{U}(t, t_0) = 1. \tag{A.3}$$

In case that the Hamiltonian is independent of time, the propagator simply reads

$$\mathscr{U}(t, t_0) = \theta(t - t_0) \exp\left[-\frac{i}{\hbar}\mathscr{L}(t - t_0)\right]. \tag{A.4}$$

Contrastingly, in case of time-dependent Hamiltonian, we need time-ordered expansion technique in order to obtain the mathematical expressions of the Liouville-space propagator. By integrating both sides of Eq. (A.2) from time t_0 to t, we can write

$$\mathscr{U}(t, t_0) = 1 - \frac{i}{\hbar}\int_{t_0}^{t} d\tau \mathscr{L}(\tau)\mathscr{U}(\tau, t_0). \tag{A.5}$$

Equation (A.5) can be solved iteratively by replacing $\mathscr{U}(\tau, t_0)$ with Eq. (A.5) itself,

$$\mathscr{U}(t, t_0) = 1 - \frac{i}{\hbar}\int_{t_0}^{t} d\tau \mathscr{L}(\tau) + \left(-\frac{i}{\hbar}\right)^2 \int_{t_0}^{t} d\tau \int_{t_0}^{\tau} d\tau' \mathscr{L}(\tau)\mathscr{L}(\tau')\mathscr{U}(\tau', t_0), \tag{A.6}$$

$$= 1 + \sum_{n=1}^{\infty}\left(-\frac{i}{\hbar}\right)^n \int_{t_0}^{t} d\tau_n \int_{t_0}^{\tau_n} d\tau_{n-1} \cdots \int_{t_0}^{\tau_2} d\tau_1 \mathscr{L}(\tau_n)\mathscr{L}(\tau_{n-1}) \cdots \mathscr{L}(\tau_1). \tag{A.7}$$

When this propagator acts on $\rho(t_0)$, we have

$$\rho(t_0)\mathscr{U}(t, t_0) = \rho(t_0) + \sum_{n=1}^{\infty}\left(-\frac{i}{\hbar}\right)^n \int_{t_0}^{t} d\tau_n \int_{t_0}^{\tau_n} d\tau_{n-1} \cdots \int_{t_0}^{\tau_2} d\tau_1 \mathscr{L}(\tau_n)\mathscr{L}(\tau_{n-1}) \cdots \mathscr{L}(\tau_1)\rho(t_0). \tag{A.8}$$

In the *n*th-order NLO processes, the state of the density matrix propagates through the Green function after the interaction of photon. Hence, we finally obtain

$$\rho^{(n)}(t) = \sum_{n=1}^{\infty}\left(-\frac{i}{\hbar}\right)^n \int_{t_0}^{t} d\tau_n \int_{t_0}^{\tau_n} d\tau_{n-1} \cdots \int_{t_0}^{\tau_2} d\tau_1 \\ \mathscr{G}(t-\tau_n)\mathscr{L}_{int}(\tau_n)\mathscr{G}(\tau_n-\tau_{n-1})\mathscr{L}_{int}(\tau_{n-1})\cdots\mathscr{G}(\tau_2-\tau_1)\mathscr{L}_{int}(\tau_1)\mathscr{G}(\tau_1-t_0)\rho(t_0). \tag{A.9}$$

Here the time variables $\{\tau_n \cdots \tau_1\}$ are defined in Fig. 2.1 (see page 12). By changing the time variables from $\{\tau_1, \cdots, \tau_n\}$ to $\{t_1, \cdots, t_n\}$, we will have Eq. (2.7) on page 12.

A.3 Coherence Green function

The linear response function is given by (see page 19)

$$J(t_1) = \langle\langle V_{eg}|\mathscr{G}_{eg}(t_1)|V_{eg}\rho_g\rangle\rangle. \tag{A.10}$$

$\mathscr{G}_{eg}(t_1)$ is called coherence Green function that describes the time evolution of the optical coherence. The coherence Green function is defined as

$$\mathscr{G}_{nm}(t) \equiv \exp\left(-\frac{i}{\hbar}H_n t\right) A \exp\left(\frac{i}{\hbar}H_m t\right). \tag{A.11}$$

By taking an arbitrary reference Hamiltonian H_j, we can write

$$H_n \equiv H_j + \bar{W}_j, \tag{A.12}$$

where $\bar{W}_j \equiv W_n - W_j$ is the difference of the potential functions of the actual and the reference Hamiltonians. By applying the time-ordered expansion technique, which was described in the former section, we have

$$\exp\left(-\frac{i}{\hbar}H_n t\right) \equiv \exp\left(-\frac{i}{\hbar}H_j t\right)\exp_+\left[-\frac{i}{\hbar}\int_0^t d\tau \bar{W}_j(\tau)\right], \tag{A.13a}$$

where

$$\exp_+\left[-\frac{i}{\hbar}\int_{t_0}^{t_1} d\tau \bar{W}_j(\tau)\right] \\ \equiv 1 + \sum_{n=1}^{\infty}\left(-\frac{i}{\hbar}\right)^n \int_{t_0}^{t} d\tau_n \int_{t_0}^{\tau_n} d\tau_{n-1} \cdots \int_{t_0}^{\tau_2} d\tau_1 \bar{W}_j(\tau_n)\bar{W}_j(\tau_{n-1})\cdots\bar{W}_j(\tau_1), \tag{A.13b}$$

with

$$\bar{W}_j(\tau) \equiv \exp\left(\frac{i}{\hbar}H_j\tau\right)\bar{W}_j \exp\left(-\frac{i}{\hbar}H_j\tau\right). \tag{A.13c}$$

In the same way, the following expressions concerning suffix m can be obtained by assuming $H_m \equiv H_j + W'_j$ and $W'_j \equiv W_m - W_j$,

$$\exp\left(\frac{i}{\hbar}H_m t\right) \equiv \exp\left(\frac{i}{\hbar}H_j t\right)\exp_-\left[\frac{i}{\hbar}\int_0^t d\tau W'_j(\tau)\right], \tag{A.14a}$$

where

$$\exp_-\left[-\frac{i}{\hbar}\int_{t_0}^{t_1} d\tau W'_j(\tau)\right] \equiv 1 + \sum_{n=1}^{\infty}\left(\frac{i}{\hbar}\right)^n \int_{t_0}^{t} d\tau_n \int_{t_0}^{\tau_n} d\tau_{n-1}\cdots\int_{t_0}^{\tau_2} d\tau_1 W'_j(\tau_n)W'_j(\tau_{n-1})\cdots W'_j(\tau_1), \tag{A.14b}$$

with

$$W'_j(\tau) \equiv \exp\left(\frac{i}{\hbar}H_j\tau\right)W'_j\exp\left(-\frac{i}{\hbar}H_j\tau\right). \tag{A.14c}$$

Hence, Eq. (A.11) can be recast as

$$\mathscr{G}_{nm}(t) = \mathscr{G}_{jj}(t)\exp_+\left[-\frac{i}{\hbar}\int_0^t d\tau \overline{W}_j(\tau)\right]A\exp_-\left[\frac{i}{\hbar}\int_0^t d\tau W'_j(\tau)\right]. \tag{A.15}$$

Using Eq. (A.15), Eq. (A.10) is now to be written

$$J(t_1) = \exp(-i\omega_{eg}t_1)\left\langle\left\langle V_{eg}\left|\mathscr{G}_{gg}(t_1)\exp_+\left[-\frac{i}{\hbar}\int_{t_0}^{t_1} d\tau U(\tau)\right]\right|V_{eg}\rho_g\right\rangle\right\rangle, \tag{A.16}$$

by setting (see Fig. 2.3 in page 20)

$$U \equiv H_e - H_g - \hbar\omega_{eg}. \tag{A.17}$$

We then have

$$J(t_1) = \exp(-i\omega_{eg}t_1)\left\langle V_{ge}(t_1)\exp_+\left[-\frac{i}{\hbar}\int_{t_0}^{t_1} d\tau U(\tau)\right]V_{eg}\rho_g\right\rangle, \tag{A.18}$$

where the time evolution of $V_{ge}(t_1)$ is defined with respect to the ground state Hamiltonian,

$$V_{ge}(t_1) \equiv \exp\left(\frac{i}{\hbar}H_g t_1\right)V_{ge}\exp\left(-\frac{i}{\hbar}H_g t_1\right), \tag{A.19}$$

and

$$U(\tau) \equiv \exp\left(\frac{i}{\hbar}H_g\tau\right)U\exp\left(-\frac{i}{\hbar}H_g\tau\right). \tag{A.20}$$

Appendix B

Photon echo and transient grating

Photon echo is one of the third-order NLO processes, in which four photons are involved. Photon echo measurements are usually performed in the folded boxcars geometry as shown in Fig. B.1 (a). The pulse sequence is schematically shown in Fig. B.1 (b). We have measured the four-wave mixing (FWM) signals along the three phase-matching directions, *i.e.*, $-\boldsymbol{k}_1 + \boldsymbol{k}_2 + \boldsymbol{k}_3$, $\boldsymbol{k}_1 - \boldsymbol{k}_2 + \boldsymbol{k}_3$, and $\boldsymbol{k}_1 + \boldsymbol{k}_2 - \boldsymbol{k}_3$, where the momentum vector of the ith pulse (i = 1, 2, and 3) is denoted by $\boldsymbol{k}_i$. In

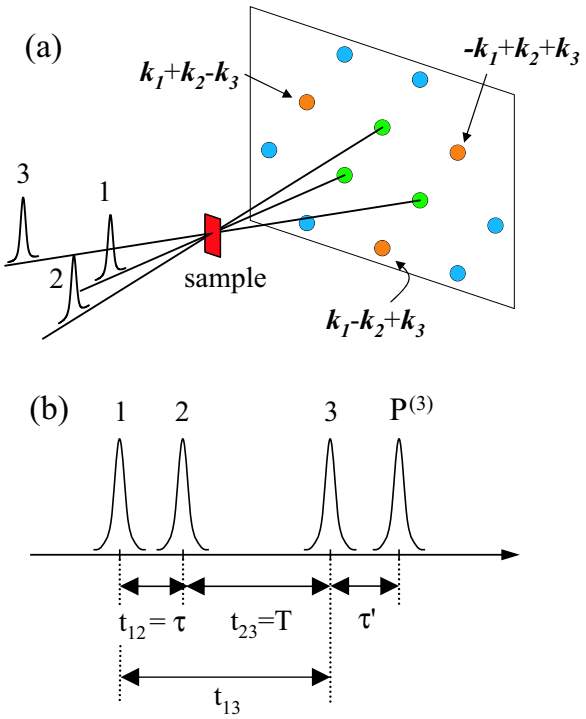

Figure B.1: (a) Spatial configuration of the FWM experiment. Three consecutive pulses with wave vectors $\boldsymbol{k}_1$, $\boldsymbol{k}_2$, and $\boldsymbol{k}_3$ are focused into the sample. (b) Time ordering of pulse sequences and notations of time intervals. τ and T denote the center-to-center distances between the pulse pairs (1, 2) and (2, 3), respectively. τ' denotes the delay of the signal from pulse 3.

the following, only the results observed along the $-\boldsymbol{k}_1 + \boldsymbol{k}_2 + \boldsymbol{k}_3$ direction will be analyzed, but all the results can be well accounted for using the same theoretical framework.

B.1 Correlated third-order response functions and cumulant expansion

In section 2.3, we have expressed only the linear response function with the line-broadening function $g(t)$ by means of cumulant expansion. This expression can be used for calculating the linear absorption spectrum. It is also used for the descriptions of the third-order response functions for the THG process under the approximation that we ignore any correlations between the three time durations t_1, t_2, and t_3, *i.e.* fast modulation limit (see page 57). Contrastingly, the correlations of the three time durations are very important in time-resolved photon echo or TG spectroscopy, so that we will introduce rigorous expressions of the third-order response functions by using cumulant expansion technique.

First we begin with Eqs. (2.24) and (2.26) on page 16. Equation (2.26) can be expressed in the style of Eq. (2.24) as

$$\begin{cases} R_1(t_3,t_2,t_1) &= \langle\langle V_{dc}|\mathscr{G}_{dc}(t_3)\mathscr{V}_{dc,\,db}\mathscr{G}_{db}(t_2)\mathscr{V}_{db,\,da}\mathscr{G}_{da}(t_1)\mathscr{V}_{da,\,aa}|\rho_{aa}\rangle\rangle, \\ R_2(t_3,t_2,t_1) &= \langle\langle V_{dc}|\mathscr{G}_{dc}(t_3)\mathscr{V}_{dc,\,db}\mathscr{G}_{db}(t_2)\mathscr{V}_{db,\,ab}\mathscr{G}_{ab}(t_1)\mathscr{V}_{ab,\,aa}|\rho_{aa}\rangle\rangle, \\ R_3(t_3,t_2,t_1) &= \langle\langle V_{dc}|\mathscr{G}_{dc}(t_3)\mathscr{V}_{dc,\,ac}\mathscr{G}_{ac}(t_2)\mathscr{V}_{ac,\,ab}\mathscr{G}_{ab}(t_1)\mathscr{V}_{ab,\,aa}|\rho_{aa}\rangle\rangle, \\ R_4(t_3,t_2,t_1) &= \langle\langle V_{ba}|\mathscr{G}_{ba}(t_3)\mathscr{V}_{ba,\,ca}\mathscr{G}_{ca}(t_2)\mathscr{V}_{ca,\,da}\mathscr{G}_{da}(t_1)\mathscr{V}_{da,\,aa}|\rho_{aa}\rangle\rangle, \end{cases} \tag{B.1}$$

where we have omitted the coefficient term $(i/\hbar)^3$ for simplicity. It should be noted that double brackets in these equations are the results of the system-bath reduced picture. The suffix indicates *one of the eigenstates of the system*, and the trace of the remaining degrees of freedom are taken by the double brackets. These mathematical expressions do not depend on the energy structure of the system. In other words, they are usable in 2-level, 3-level, ..., and in n-level systems. The corresponding double-sided Feynman diagrams of these four response functions are shown in Fig. B.2. We will switch the notation of the response functions from the Liouville-space to the Hilbert space by using these diagrams. The response functions R_1–R_4 are then recast as

$$\begin{cases} R_1(t_3,t_2,t_1) &= \langle V_{dc}(t_1+t_2+t_3)V_{da}(0)\rho_{aa}V_{ba}(t_1)V_{cb}(t_1+t_2)\rangle \\ &= F(t_1,\ t_1+t_2,\ t_1+t_2+t_3,\ 0), \\ R_2(t_3,t_2,t_1) &= \langle V_{cd}(t_1+t_2+t_3)V_{da}(t_1)\rho_{aa}V_{ba}(0)V_{cb}(t_1+t_2)\rangle \\ &= F(0,\ t_1+t_2,\ t_1+t_2+t_3,\ t_1), \\ R_3(t_3,t_2,t_1) &= \langle V_{cd}(t_1+t_2+t_3)V_{da}(t_1+t_2)\rho_{aa}V_{ba}(0)V_{cb}(t_1)\rangle \\ &= F(0,\ t_1,\ t_1+t_2+t_3,\ t_1+t_2), \\ R_4(t_3,t_2,t_1) &= \langle V_{ab}(t_1+t_2+t_3)V_{bc}(t_1+t_2)V_{cd}(t_1)V_{da}(0)\rho_{aa}\rangle \\ &= F(t_1+t_2+t_3,\ t_1+t_2,\ t_1,\ 0), \end{cases} \tag{B.2}$$

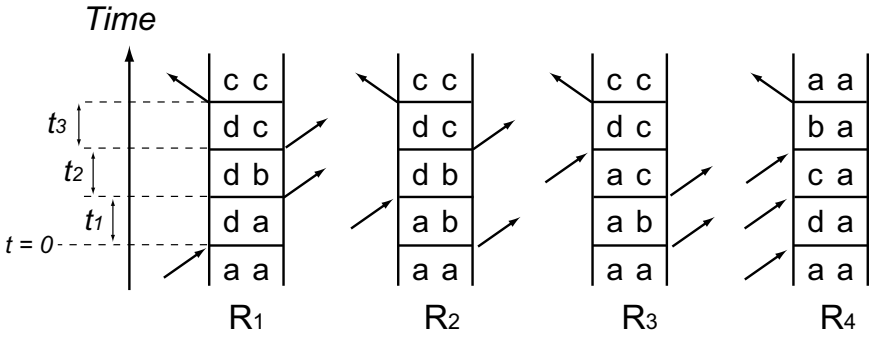

Figure B.2: The double-sided Feynman diagrams of the response functions R_1–R_4. The suffices *a*, *b*, *c*, and *d* denote arbitrary eigenstates. The origin of the time is located at the point at which the first photon interacts the system. The time intervals t_1, t_2 and t_3 are defined in the figure.

where

$$F(\tau_1, \tau_2, \tau_3, \tau_4) \equiv \langle V_{ab}(\tau_1) V_{bc}(\tau_2) V_{cd}(\tau_3) V_{da}(\tau_4) \rangle. \tag{B.3}$$

It should be noted that the Hilbert space dipole operator can act one of the two sides of the double-sided Feynman diagram. For example, when the photon is interacted from the left at time $t_1 + t_2$, it should be written $\langle V(t_1 + t_2)\rho_{aa} \rangle$ (see Refs. [181–184] for the details).

$F(\tau_1, \tau_2, \tau_3, \tau_4)$ is called four-point correlation function. The four-point correlation function facilitates the calculations of the response functions to a great extent. Hereafter we assume a two-state model comprising the ground and excited states. In addition, we use Franck-Condon approximation and time-ordered expansion technique as described in section 2.3. By truncating the cumulant expansion at the second-order term, we obtain

$$\begin{aligned} F(\tau_1, \tau_2, \tau_3, \tau_4) \approx & \exp\left[-i\omega_{eg}(\tau_1 - \tau_2 + \tau_3 - \tau_4)\right] \\ & \times [1 - X(\tau_1) - g(\tau_1)] \times [1 + X(\tau_2) - g^*(\tau_2)] \\ & \times [1 - X(\tau_3) - g(\tau_3)] \times [1 + X(\tau_4) - g^*(\tau_4)], \end{aligned} \tag{B.4}$$

where

$$X(\tau) \equiv \frac{i}{\hbar} \int_0^\tau d\tau' U(\tau'), \quad g(\tau) \equiv \left(-\frac{i}{\hbar}\right)^2 \int_0^\tau d\tau' \int_0^{\tau'} d\tau'' U(\tau') U(\tau''). \tag{B.5}$$

$X(\tau)$ vanishes when we take the ensemble average, *i.e.* $\langle X(\tau) \rangle \sim 0$. Equation (B.4) can be further approximated, by gathering until second-order terms of U:

$$\begin{aligned} F(\tau_1, \tau_2, \tau_3, \tau_4) \sim & \exp\left[-i\omega_{eg}(\tau_1 - \tau_2 + \tau_3 - \tau_4)\right] \\ & \times [1 - g(\tau_1) - g^*(\tau_2) - g(\tau_3) - g^*(\tau_4) \\ & + h(\tau_1, \tau_2) - h(\tau_1, \tau_3) + h(\tau_2, \tau_3) \\ & + h(\tau_1, \tau_4) - h(\tau_2, \tau_4) + h(\tau_3, \tau_4)], \end{aligned} \tag{B.6}$$

where

$$h(\tau_1, \tau_2) \equiv -X(\tau_1) X(\tau_2). \tag{B.7}$$

As stated in Ref. [50], we have following relations concerning $h(\tau_1, \tau_2)$ and $g(\tau)$:

$$h(\tau_1, \tau_2) = g(\tau_1) - g(\tau_1 - \tau_2) + g(-\tau_2), \tag{B.8}$$

and

$$g(-\tau) = g^*(\tau). \tag{B.9}$$

Hence Eq. (B.6) can be recast as

$$\begin{aligned} F(\tau_1, \tau_2, \tau_3, \tau_4) \sim & \exp\left[-i\omega_{eg}(\tau_1 - \tau_2 + \tau_3 - \tau_4)\right] \\ & \times [1 - g(\tau_1 - \tau_2) + g(\tau_1 - \tau_3) - g(\tau_2 - \tau_3) \\ & - g(\tau_1 - \tau_4) + g(\tau_2 - \tau_4) - g(\tau_3 - \tau_4)]. \end{aligned} \tag{B.10}$$

Consequently, the response functions R_1–R_4 in Eq. (B.2) can be expressed in terms of the line-broadening function $g(t)$ as

$$\begin{aligned} R_1(t_3, t_2, t_1) &= \exp\left(-i\omega_{eg}t_1 - i\omega_{eg}t_3\right) \\ &\quad \times \exp\left[-g^*(t_3) - g(t_1) - f_+(t_3, t_2, t_1)\right], && \text{(B.11a)} \\ R_2(t_3, t_2, t_1) &= \exp\left(i\omega_{eg}t_1 - i\omega_{eg}t_3\right) \\ &\quad \times \exp\left[-g^*(t_3) - g^*(t_1) + f_+^*(t_3, t_2, t_1)\right], && \text{(B.11b)} \\ R_3(t_3, t_2, t_1) &= \exp\left(i\omega_{eg}t_1 - i\omega_{eg}t_3\right) \\ &\quad \times \exp\left[-g(t_3) - g^*(t_1) + f_-^*(t_3, t_2, t_1)\right], && \text{(B.11c)} \\ R_4(t_3, t_2, t_1) &= \exp\left(-i\omega_{eg}t_1 - i\omega_{eg}t_3\right) \\ &\quad \times \exp\left[-g(t_3) - g(t_1) - f_-(t_3, t_2, t_1)\right], && \text{(B.11d)} \end{aligned}$$

where

$$f_-(t_3, t_2, t_1) \equiv g(t_2) - g(t_2 + t_3) - g(t_1 + t_2) + g(t_1 + t_2 + t_3), \tag{B.11e}$$

$$f_+(t_3, t_2, t_1) \equiv g^*(t_2) - g^*(t_2 + t_3) - g(t_1 + t_2) + g(t_1 + t_2 + t_3). \tag{B.11f}$$

B.2 Third-order response functions for the photon-echo process

Transient grating (TG), which we have measured in chapter 3, is one possible case of those that can be realized in the photon echo pulse sequence, *i.e.* $\tau = \tau' = 0$. By assuming the four-state model that comprises S_0, S_1, S_2, and S_T (see Fig. 3.6 in page 37), the mathematical expressions of the possible response functions for

the photon echo process (R_1–R_5) are given by

$$R_1 = |\mu_{20}|^4 \exp[-g^*(\tau) + g^*(T) - g(\tau') - g^*(\tau + T) - g^*(T + \tau') + g^*(\tau + T + \tau')], \tag{B.12a}$$

$$R_2 = |\mu_{20}|^4 n_2(t) \exp[-g^*(\tau) + g(T) - g^*(\tau') - g^*(\tau + T) - g(T + \tau') + g^*(\tau + T + \tau')], \tag{B.12b}$$

$$R_3 = |\mu_{20}|^4 r(t) \exp[-g^*(\tau) - g(\tau')], \tag{B.12c}$$

$$R_4 = |\mu_{20}|^2 |\mu_{T2}|^2 n_2(t) \exp[-g^*(\tau) - g(\tau')], \tag{B.12d}$$

$$R_5 = |\mu_{20}|^4 [n_0(t) - r(t)] \exp[-g^*(\tau) - g(\tau')], \tag{B.12e}$$

where, by introducing $\Gamma \equiv \Gamma_{20} + \Gamma_{21}$,

$$n_2(t) = e^{-\Gamma t}, \tag{B.12f}$$

$$n_1(t) = \frac{\Gamma_{21}}{\Gamma_{10} - \Gamma}(e^{-\Gamma t} - e^{-\Gamma_{10} t}), \tag{B.12g}$$

$$n_0(t) = \frac{1}{\Gamma_{10} - \Gamma}[(\Gamma_{10} - \Gamma)(1 - e^{-\Gamma t}) + \Gamma_{21}(e^{-\Gamma_{10} t} - e^{-\Gamma t})], \tag{B.12h}$$

$$r(t) = (1 - \Gamma_{21})/\Gamma(1 - e^{-\Gamma t}). \tag{B.12i}$$

It should be noted that R_1–R_4 in Eq. (B.12) do not correspond to those introduced in the last section. Rather R_1 and R_2 in Eq. (B.12) correspond to R_3 and R_2 in Eq. (B.11), respectively. The response functions R_3–R_5 in Eq. (B.12) do not contain terms of the line-broadening function that include time duration T, *i.e.* $g(T)$. This means that the correlation is lost during the population relaxation from the S_2 state, therefore we have omitted $g(T)$ and $g^*(T)$ from R_3–R_5. This assumption is verified by the fact that the calculation with conserving the correlations always failed to reproduce the experimental data. We believe that this correlation loss is caused by the difference of the characteristic vibrational frequency between that of the S_2 state and of the S_1 state. The theoretical simulations of photon-echo signals have never been well reproduced, unless we assumed the conservation of the correlation during the population relaxation between the electronic states [70].

In the homodyne detection scheme, the photon echo signal S_{PE} is given by the time-integrated signal along the $\boldsymbol{k}$ direction,

$$S_{\mathrm{PE}}(\tau, T) = \int_0^\infty dt |P^{(3)}(\boldsymbol{k}, t)|^2, \tag{B.13}$$

with

$$P^{(3)}(\boldsymbol{k}, t) \propto \int_0^\infty dt_3 \int_0^\infty dt_2 \int_0^\infty dt_1 R(t_3, t_2, t_1) \exp[-\Delta_{in}^2 (t_3 - t_1)^2/2] \times E_3(t - t_3) E_2(t + T - t_3 - t_2) E_1^*(t + T + \tau - t_3 - t_2 - t_1) \times \exp[i(\omega_2 - \omega_1)t_2 - i\omega_1 t_1], \tag{B.14}$$

where $E_j(t)$ denotes the temporal envelope of the jth incident pulse with its mean frequency ω_j. Next we consider two approximations for the simplification of

Eq. (B.14): (1) impulsive excitation pulses $E_j(t) \sim \delta(t)$, (2) the infinitely large inhomogeneous broadening $\exp[-\Delta_{in}^2(t_3 - t_1)^2/2] \sim \delta(t_3 - t_1)$. Under these conditions, we finally get

$$S_{\mathrm{PE}}(\tau, T) \sim |R_{total}(\tau, T, \tau')|^2, \tag{B.15}$$

where $R_{total} = \sum_i^5 R_i(\tau, T, \tau')$ and $\tau = \tau' = 0$ for the case of TG. Thus we are ready to calculate the TG signals of the β-carotene homologues.

Appendix C

THG Maker fringes in isotropic media

C.1 Simple case of Maker fringes in isotropic media

For the sake of simplicity, we first describe a simple case of THG Maker fringes, in which any complicated phenomena such as multiple reflections or absorption in media are not incorporated. This simple theory will be extended to the case that includes the multiple reflections and the absorptions in the media. Our theory described here is conceptually based on the report of van Beek *et. al.* [132, 141, 185]. But our notation and logical steps are mostly based on the generalized theory of Maker fringes developed by Pavlides *et. al.* [137].

C.1.1 Solving the wave equations in NLO media

First we consider a case that a fundamental plane wave (ω-wave) propagates through three different isotropic media, I, II, and III [see Fig. 4.3 (a) at page 50]. The ω-wave, denoted Wave 1, is reflected back into the medium I (Wave 2) and refracted into the medium II (Wave 3 and 4). Wave 3 and 4 are multiply reflected forwarding and back-warding waves, respectively. Figure 4.3 (b) (see page 50) shows the 3ω-waves (Wave 5–10). There exist two kinds of 3ω-waves in the medium II, *i.e.* bound waves (Wave 5, 6) and free waves (Wave 7, 8). The origin of these two types of waves can be clearly seen in the Maxwell equations. The bound wave is a 3ω-wave, which is generated by the *source term* of the nonlinear polarization. The free wave is the one that already exists when the bound wave is generated. Wave 8 and 9 are reflected 3ω-wave in the media II and I, respectively. Wave 10 is a transmitted 3ω-wave into the medium III. Wave 4 and 6 is not necessary in the present simple case, but they must be considered under the presence of multiple reflections.

The wave equations for the ω-, 3ω-free, and 3ω-bound waves in the media can

be described as follows,

$$\text{rot rot}\boldsymbol{E}(\omega) - \left(\frac{\omega}{c_0}\right)^2 \boldsymbol{\varepsilon}(\omega) : \boldsymbol{E}(\omega) = 0 \quad (\omega\text{-wave}), \tag{C.1a}$$

$$\text{rot rot}\boldsymbol{E}(3\omega) - \left(\frac{3\omega}{c_0}\right)^2 \boldsymbol{\varepsilon}(3\omega) : \boldsymbol{E}(3\omega) = 0 \quad (3\omega\text{-free wave}), \tag{C.1b}$$

$$\text{rot rot}\boldsymbol{E}(3\omega) - \left(\frac{3\omega}{c_0}\right)^2 \boldsymbol{\varepsilon}(3\omega) : \boldsymbol{E}(3\omega) = \mathcal{P}_{NL}(3\omega) \quad (3\omega\text{-bound wave}), \tag{C.1c}$$

where

$$\mathcal{P}_{NL}(3\omega) = \left(\frac{3\omega}{c_0}\right)^2 \boldsymbol{\chi}^{(3)}(-3\omega;\omega,\omega,\omega) : \boldsymbol{E}(\omega)\boldsymbol{E}(\omega)\boldsymbol{E}(\omega). \tag{C.1d}$$

Magnitude of the wavevectors are expressed as follows:

$$k_{\text{vac}}(\omega) = \frac{\omega}{c_0} = k_0, \tag{C.2}$$

$$k_{\text{vac}}(3\omega) = \frac{3\omega}{c_0} = 3k_0. \tag{C.3}$$

Here, we define a dimensionless value ξ_I that characterizes the z-component of the wave I:

$$\xi_I = \frac{k_{Iz}}{k_{\text{vac}}(\Omega_I)}. \tag{C.4}$$

We will define an operator,

$$\hat{\boldsymbol{F}}(\Omega)\mathcal{A} = [k_{\text{vac}}(\Omega_I)]^{-2}\left[\text{rot rot}\mathcal{A} - \left(\frac{\Omega}{c_0}\right)^2 \varepsilon^{\Omega} : \mathcal{A}\right], \tag{C.5}$$

where $\mathcal{A}$, ε^{Ω}, and c_0 are an arbitrary vector, the dielectric constant of the crystalline axis I at frequency Ω, and the speed of light in vacuum, respectively. Then, Eqs. (C.1a) and (C.1b) can be written in the following form,

$$\hat{\boldsymbol{F}}(\Omega)\boldsymbol{E}_I(\Omega) = 0. \tag{C.6}$$

Only non-trivial solutions are obtained if

$$|\boldsymbol{F}(\xi,\varepsilon)| = 0. \tag{C.7}$$

Since all of the media considered here are isotropic, the left-hand side of Eq. (C.7) can be simplified to

$$|\boldsymbol{F}(\xi,\varepsilon)| = \begin{vmatrix} \xi^2 - \varepsilon & 0 & -s\xi \\ 0 & \xi^2 + s^2 - \varepsilon & 0 \\ -s\xi & 0 & s^2 - \varepsilon \end{vmatrix}. \tag{C.8}$$

Hereafter, $\sin\theta$ and $\cos\theta$ are simply denoted s and c, respectively. Equation (C.7) can be solved by using Eq. (C.8). Consequently the value of ξ for wave I is expressed as a function of ε_I and s:

$$\xi_1 = -\xi_2 = \sqrt{\varepsilon_I^{\omega} - s^2}, \tag{C.9a}$$

$$\xi_9 = -\sqrt{\varepsilon_I^{3\omega} - s^2}, \tag{C.9b}$$

$$\xi_{10} = \sqrt{\varepsilon_{III}^{3\omega} - s^2}, \tag{C.9c}$$

$$\xi_3 = \xi_5 = \sqrt{\varepsilon_{II}^{\omega} - s^2}, \tag{C.9d}$$

$$\xi_7 = -\xi_8 = \sqrt{\varepsilon_{II}^{3\omega} - s^2}. \tag{C.9e}$$

These are the cases of the free waves.

In case of the bound wave, Eq. (C.1c) must be solved explicitly. Equation (C.1c) can be rewritten using the operator defined in Eq. (C.5):

$$\begin{aligned}\hat{\boldsymbol{F}}(3\omega)\boldsymbol{E}(3\omega) &= (k_{\mathrm{vac}}(3\omega))^{-2}\mathcal{P}_{NL}(3\omega),\\ &= \chi^{(3)}(-3\omega;\omega,\omega,\omega) : |\boldsymbol{E}_3(\omega)|^3.\end{aligned} \tag{C.10}$$

When the right-hand side of Eq. (C.10) is defined as $\boldsymbol{P}(3\omega)$, its y-component is written as

$$P_y(3\omega) = \chi^{(3)}_{yyyy} t_5 e^{3i\xi_5 k_0 z}. \tag{C.11}$$

Here, t_5 is the transmission factor for Wave 5 [see Eq. (C.19)]. In addition, the right-hand side of Eq. (C.10) is proportional to $\left(T_{I-II}E_1 e^{i\xi_3 k_0 z}\right)^3$, where T_{I-II} is the transmittance at the I-II surface. Therefore, $\xi_3 = \xi_5$ and $t_5 = T_{I-II}^3$ are obtained. Since Wave 5 is the bound wave, it can be calculated by solving Eq. (C.10):

$$\begin{aligned}\frac{\boldsymbol{E}_5}{E_1^3} &= |\boldsymbol{F}(\xi_5,\boldsymbol{\varepsilon})|^{-1} F_{yy}^A(\xi_5,\boldsymbol{\varepsilon})\boldsymbol{P}_5,\\ E_5 &= E_1^3[-\varepsilon_{II}^{3\omega}(\xi_5^2 + s^2 - \varepsilon_{II}^{3\omega})]^{-1} F_E \chi^{(3)}_{yyyy} t_5 e^{3i\xi_3 k_0 z},\end{aligned} \tag{C.12}$$

where $F_{yy}^A = F_E = (\xi^2 - \varepsilon)(s^2 - \varepsilon) - s^2\xi^2$ was used. Hence, Eq. (C.12) can be reduced to a simpler form:

$$E_5 = \frac{\chi^{(3)}_{yyyy}}{\xi_3^2 - \xi_7^2} t_5 E_1^3 e^{3i\xi_3 k_0 z}. \tag{C.13}$$

C.1.2 Boundary conditions

Boundary conditions at the surface of the two media should be considered in order to calculate the mathematical expressions of our observed THG, *i.e.* E_{10}. The boundary conditions are equivalent to the fact that the tangential components of

the electric and magnetic fields must be continuous at the surfaces ($z = 0,\ L$) [48]. This can be derived from the Maxwell equations,

$$\oint \boldsymbol{E} \cdot d\boldsymbol{l} = 0, \tag{C.14}$$

$$\oint \boldsymbol{H} \cdot d\boldsymbol{l} = 0 \quad \leftrightarrow \quad \oint (\mathrm{rot}\ \boldsymbol{E}) \cdot d\boldsymbol{l} = 0, \tag{C.15}$$

where

$$(\mathrm{rot}\ \boldsymbol{E})_x = \xi_I E_I. \tag{C.16}$$

In our case the polarizations of all of the electric fields are parallel to the Y-axis, and the polarizations of all of the magnetic fields lie in the XZ-plane, so that boundary conditions of E_{Iy} and $H_{Ix} \propto \xi_I E_I$ are sufficient to know the actual expressions of E_{10}.

(1) Boundary conditions for ω-wave at $z = 0$.

$$\begin{cases} E_1 + E_2 = E_3 & \text{(a)} \\ \xi_1 E_1 + \xi_2 E_2 = \xi_3 E_3 & \text{(b)} \end{cases} \tag{C.17}$$

By solving these equations, we have

$$E_3 = \frac{2\xi_1}{\xi_1 + \xi_3} E_1, \tag{C.18}$$

$$t_5 = \left(\frac{E_3}{E_1} \right)^3. \tag{C.19}$$

(2) Boundary conditions for 3ω-wave at $z = 0$.

$$\begin{cases} E_9 = E_5 + E_7 & \text{(a)} \\ \xi_9 E_9 = \xi_7 E_7 + \xi_5 E_5 & \text{(b)} \end{cases} \tag{C.20}$$

By eliminating E_9, E_7 can be given by

$$E_7 = \frac{\xi_5 - \xi_9}{\xi_9 - \xi_7} E_5. \tag{C.21}$$

(3) Boundary conditions for 3ω-wave at $z = L$.

$$\begin{cases} f_{10} E_{10} = f_5 E_5 + f_7 E_7 + f_8 E_8 & \text{(a)} \\ \xi_{10} E_{10} f_{10} = \xi_5 E_5 f_5 + \xi_7 E_7 f_7 + \xi_8 E_8 f_8 & \text{(b)} \end{cases} \tag{C.22}$$

By eliminating E_8 and omitting f_{10}, E_{10} can be expressed as follows:

$$E_{10} = \frac{\xi_8 - \xi_7}{\xi_8 - \xi_{10}} f_7 E_7 + \frac{\xi_8 - \xi_5}{\xi_8 - \xi_{10}} f_5 E_5. \tag{C.23}$$

Here, f_I is a phase factor of wave I, which is given by $f_I = e^{3i\xi_I k_0 L}$. It should be noted that the phase factor is a result of phase shift between $z = 0$ and $z = L$. Therefore f_{10} is not important, hence it was omitted. The derivation of E_{10} from Eq. (C.23) is straightforward. It can be expressed as a function of the fundamental input E_5 by using the relations, $\xi_5 = \xi_3$ and $\xi_7 = -\xi_8$:

$$E_{10} = \left[\frac{2\xi_7(\xi_3 - \xi_9)}{(\xi_{10} + \xi_7)(\xi_9 - \xi_7)} f_7 + \frac{\xi_3 + \xi_7}{\xi_{10} + \xi_7} f_5 \right] E_5. \tag{C.24}$$

If we define

$$A = \frac{2\xi_7(\xi_3 - \xi_9)}{(\xi_{10} + \xi_7)(\xi_7 - \xi_9)} \text{ and } B = \frac{\xi_3 + \xi_7}{\xi_{10} + \xi_7},$$

the intensity of the observed THG ($I = |E_{10}|^2$) is calculated as

$$\begin{aligned} I = |E_{10}|^2 &= (-Af_7 + Bf_5)(-Af_7^* + Bf_5^*)E_5^2, \\ &= A^2 + B^2 - AB(f_5 f_7^* + f_7 f_5^*)E_5^2, \\ &\approx -2AB(1 + \cos\Delta\phi)E_5^2, \\ &= -4AB\cos^2\frac{\Delta\phi}{2}E_5^2, \\ &\approx 4AB\sin^2\frac{\Delta\phi}{2}E_5^2, \end{aligned} \tag{C.25}$$

where $\Delta\phi = \phi_5 - \phi_7$. Hence, it is convenient to rewrite Eq. (C.24) as

$$E_{10} = \sqrt{AB}(e^{i\Delta\phi} - 1)E_5^2. \tag{C.26}$$

This equation is essentially equivalent to the expressions described in Refs. [132, 141].

C.2 Multiple-reflections correction

Almost of all of organic materials, including carotenoids that we are studying now, are dispersed in a polymer film deposited on the fused-silica substrate in order to be subjected to the Maker fringe measurement. Thickness of the film is typically $\sim 0.1\ \mu$m. The difference of the refractive indices between the substrate and the film is less than 0.1, while the difference between the substrate and the air (or the film and the air) is approximately 0.5. Therefore, the multiple reflections in the film significantly affect the results of the measurements. In particular, the multiple-reflections correction needs to be incorporated into the theory when the measurement is done with "back-side" configuration, where the film is located on the near side to the detector. We will develop the extended Maker fringe theory that incorporates the effect of multiple reflections.

C.2.1 Multiple reflections of the fundamental input

When the multiple reflections in the film are considered, Wave 3 and 4 become sums of the forwarding and backwarding ω-wave, respectively [see Fig. 4.3 (a) at page 50]. The effect of the multiple reflections should be considered in Wave 3 and 4. We suppose that the reflectance and transmittance for the propagation from I→II are denoted r_1 and t_1, respectively (also r_2 and t_2 for the II→III propagation). In the same way, the corresponding coefficients for the opposite propagation from II→I are r_1' and t_1', respectively (also r_2' and t_2' for the III→II propagation). Hence $r_1' = -r_1$ [186]. By defining t_5 in Eq. (C.13) as T_S^3, E_3 and E_4 can be written as TT_SE_1 and RT_SE_1, respectively, where

$$\begin{aligned} T &= t_1 + t_1 r_1' r_2 f_3^2 + \cdots, \\ &= t_1 \left(\sum_{n=1}^{\infty} (-1)^{n-1} r_1^{n-1} r_2^{n-1} f_3^{2n-2} \right), \\ &= \frac{t_1}{1 + r_1 r_2 f_3^2}, \end{aligned} \tag{C.27}$$

(C.28)

and

$$\begin{aligned} R &= t_1 r_2 f_3^2 + t_1 r_1' r_2^2 f_3^4 + \cdots, \\ &= t_1 \left(\sum_{n=1}^{\infty} (-1)^{n-1} r_1^{n-1} r_2^{n} f_3^{2n} \right), \\ &= \frac{t_1 r_2 f_3^2}{1 + r_1 r_2 f_3^2}. \end{aligned} \tag{C.29}$$

Here, f_3 is the phase factor defined in the last section.

We then solve the inhomogeneous wave equation:

$$\hat{\boldsymbol{F}}(3\omega)\boldsymbol{E}(3\omega) = \boldsymbol{\chi}^{(3)} : (\boldsymbol{E}_3 + \boldsymbol{E}_4)^3 . \tag{C.30}$$

The right-hand side of Eq. (C.30) is proportional to the cubic of the sum of E_3 and E_4. By using the relation $\xi_4 = -\xi_3$, this can be expressed as

$$\begin{aligned} &(TT_SE_1 e^{i\xi_3 k_0 z} + RT_SE_1 e^{-i\xi_3 k_0 z})^3 \\ =&T_S^3 (TTTe^{3i\xi_3 k_0 z} + 3TTRe^{i\xi_3 k_0 z} + 3TRRe^{-i\xi_3 k_0 z} + RRRe^{-3i\xi_3 k_0 z}). \end{aligned} \tag{C.31}$$

Here we only take into account the forwarding ω-waves TTT and TTR, *i.e* ignoring the backwarding waves. The remaining terms of Eq. (C.31) TTT and TTR are denoted Wave 5 and 6, respectively. These are schematically shown in Fig. 4.3 (b) on page 50. Hence, the expressions of E_5 and E_6 can be obtained by solving

Eq. (C.30):

$$\frac{\boldsymbol{E}_I}{E_1^3} = |\boldsymbol{F}(\xi_I, \boldsymbol{\varepsilon})|^{-1} F_{yy}^A(\xi_I, \boldsymbol{\varepsilon}) \boldsymbol{P}_I,$$
$$E_I = \begin{cases} \frac{\chi_{yyyy}^{(3)}}{\xi_5^2 - \xi_8^2} T_S^3 TTT e^{3i\xi_5 k_0 z}, & I = 5, \\ \frac{\chi_{yyyy}^{(3)}}{\xi_6^2 - \xi_8^2} T_S^3 TTR e^{3i\xi_6 k_0 z}, & I = 6, \end{cases} \tag{C.32}$$

where

$$\xi_5 = \xi_3, \quad 3\xi_6 = \xi_3. \tag{C.33}$$

C.2.2 Boundary conditions under the presence of the multiply reflected waves

(1) Boundary conditions for 3ω-wave at $z = 0$.

$$\begin{cases} E_9 = E_5 + E_6 + E_7 & \text{(a)} \\ \xi_9 E_9 = \xi_5 E_5 + \xi_6 E_6 + \xi_7 E_7 & \text{(b)} \end{cases} \tag{C.34}$$

Eliminating E_9, E_7 can be expressed as follows:

$$E_7 = \frac{\xi_5 - \xi_9}{\xi_9 - \xi_7} E_5 + \frac{\xi_6 - \xi_9}{\xi_9 - \xi_7} E_6. \tag{C.35}$$

(2) Boundary conditions for 3ω-wave at $z = L$.

$$\begin{cases} f_{10} E_{10} = f_5 E_5 + f_6 E_6 + f_7 E_7 + f_8 E_8 & \text{(a)} \\ \xi_{10} E_{10} f_{10} = \xi_5 E_5 f_5 + \xi_6 f_6 E_6 + \xi_7 E_7 f_7 + \xi_8 E_8 f_8 & \text{(b)} \end{cases} \tag{C.36}$$

By eliminating E_8 and ignoring f_{10}, E_{10} can be expressed as follows:

$$E_{10} = \frac{\xi_8 - \xi_7}{\xi_8 - \xi_{10}} f_7 E_7 + \frac{\xi_8 - \xi_5}{\xi_8 - \xi_{10}} f_5 E_5 + \frac{\xi_6 - \xi_{10}}{\xi_8 - \xi_{10}} f_6 E_6. \tag{C.37}$$

By inserting Eq. (C.35) into Eq. (C.37) and using the relations $\xi_5 = \xi_3$, $\xi_7 = -\xi_8$, we then obtain the final expression of E_{10}:

$$E_{10} = \left[\frac{2\xi_7(\xi_3 - \xi_9)}{(\xi_{10} + \xi_7)(\xi_9 - \xi_7)} f_7 + \frac{\xi_3 + \xi_7}{\xi_{10} + \xi_7} f_5 \right] E_5 + \left[\frac{2\xi_7(\xi_6 - \xi_9)}{(\xi_{10} + \xi_7)(\xi_9 - \xi_7)} f_7 + \frac{\xi_6 + \xi_7}{\xi_{10} + \xi_7} f_6 \right] E_6. \tag{C.38}$$

This can be written in the same manner as Eq. (C.26) as

$$E_{10} = \sqrt{A_1}(e^{i(\phi_5 - \phi_7)} - 1) E_5 + \sqrt{A_2}(e^{i(\phi_6 - \phi_7)} - 1) E_6, \tag{C.39}$$

where

$$A_1 = \frac{2\xi_7(\xi_3 - \xi_9)(\xi_3 + \xi_7)}{(\xi_{10} + \xi_7)^2(\xi_7 - \xi_9)} \quad \text{and} \quad A_2 = \frac{2\xi_7(\xi_6 - \xi_9)(\xi_6 + \xi_7)}{(\xi_{10} + \xi_7)^2(\xi_7 - \xi_9)}. \tag{C.40}$$

C.2.3 Correction factors for the absorption of the THG in the film

The observed THG waves are absorbed in the film by carotenoids to a certain extent. This absorption causes a phase shift and the decrease of the THG intensity, which result in the changes of the positions of the fringe's minima and the underestimation of the modulus of the film's $\chi^{(3)}$. Thus, correction factors for the film absorption should be considered.

Under the presence of absorption (extinction coefficient κ), the refractive index of the film becomes a complex number that is defined as

$$n \to n + i\kappa. \tag{C.41}$$

Hence, $\xi = \sqrt{n^2 - \sin^2\theta}$ can be recast as

$$\begin{aligned} \xi &= \sqrt{(n+i\kappa)^2 - s^2} \\ &= \sqrt{n^2 - \kappa^2 - s^2 + 2in\kappa} \\ &= \sqrt{n^2 - \kappa^2 - s^2}\left(1 + i\frac{2n\kappa}{\sqrt{n^2 - \kappa^2 - s^2}}\right)^{\frac{1}{2}}. \end{aligned} \tag{C.42}$$

Under the weak absorption limit we then have

$$\frac{n\kappa}{\sqrt{n^2 - \kappa^2 - s^2}} = \frac{n\kappa}{\sqrt{n^2 - \kappa^2}} \quad (\text{at } \theta = 0) \sim \frac{\kappa}{n} \ll 1. \tag{C.43}$$

Hence Eq. (C.42) can be expanded into the polynomial series

$$\sqrt{1+ix} = 1 + \frac{ix}{2} + \frac{x^2}{8} - \frac{ix^3}{16} + \cdots, \tag{C.44}$$

where

$$x = \frac{n\kappa}{\sqrt{n^2 - \kappa^2 - s^2}}.$$

In practice, the phase shift caused by the higher-order terms in Eq. (C.44) is so small that the first-order approximation is enough for the quantitative evaluation. Moreover, this approximation makes the curve-fitting analysis much easier. Therefore, we will ignore the phase shift caused by the absorption of the film, and the intensity of the THG is considered to be affected . Finally, we assume that the film has refractive index dispersion the same as that of the host polymer. With these approximations, we can introduce the absorption correction factor:

$$\alpha = \exp\left[-3i\frac{n\kappa}{\sqrt{n^2 - s^2}}k_0 L\right]. \tag{C.45}$$

C.3 Theoretical formulae with multiply reflected waves

As a summary of this appendix, the final theoretical formulae and their parameters are defined as follows. The observed THG intensity is given by

$$I_{\mathrm{THG}} \propto |E_{10}|^2. \tag{C.46a}$$

E_{10} is given by

$$E_{10} = \alpha(E_{10}^S + E_{10}^F) \tag{C.46b}$$

where

$$\begin{aligned}
E_{10}^S &= \sqrt{A_S}(e^{i(\phi_{5S}-\phi_{7S})}-1)\chi_S^{(3)}T_S^3E_1^3,\\
A_S &= \frac{2\xi_{7S}(\xi_{3S}+c)(\xi_{3S}+\xi_{7S})}{(\xi_{10S}+\xi_{7S})^2(\xi_{7S}+c)(\xi_{3S}^2-\xi_{7S}^2)},\\
T_S &= \frac{2c}{c+\xi_{3S}},\quad \alpha = \exp\left[-3i\frac{n_{IF}\kappa}{\sqrt{n_{IF}^2-s^2}}k_0L_F\right],\\
\xi_{3S} &= \sqrt{\varepsilon_S^{\omega}-s^2},\quad \xi_{7S} = \sqrt{\varepsilon_S^{3\omega}-s^2},\quad \xi_{10S} = \sqrt{\varepsilon_F^{3\omega}-s^2},\\
\phi_{5S} &= 3\xi_{3S}k_0L_S,\quad \phi_{7S} = 3\xi_{7S}k_0L_S,
\end{aligned} \tag{C.46c}$$

and

$$\begin{aligned}
E_{10}^F &= \sqrt{A_{F1}}(e^{i(\phi_{3F}-\phi_{7F})}-1)\chi_F^{(3)}T_F^3T_S^3E_1^3 + \sqrt{A_{F2}}(e^{i(\phi_{6F}-\phi_{7F})}-1)\chi_F^{(3)}T_F^2R_FT_S^3E_1^3,\\
A_{F1} &= \frac{2\xi_{7F}(\xi_{3F}-\xi_{9F})(\xi_{3F}+\xi_{7F})}{(c+\xi_{7F})^2(\xi_{7F}-\xi_{9F})(\xi_{3F}^2-\xi_{7F}^2)},\\
A_{F2} &= \frac{2\xi_{7F}(\xi_{6F}-\xi_{9F})(\xi_{6F}+\xi_{7F})}{(c+\xi_{7F})^2(\xi_{7F}-\xi_{9F})(\xi_{6F}^2-\xi_{7F}^2)},\\
T_F &= \frac{t_1}{1+r_1r_2e^{i2\phi_{3F}}},\quad R_F = \frac{t_1r_2e^{i2\phi_{3F}}}{1+r_1r_2e^{i2\phi_{3F}}},\\
r_1 &= \frac{\xi_{1F}-\xi_{3F}}{\xi_{1F}+\xi_{3F}},\quad t_1 = \frac{2\xi_{1F}}{\xi_{1F}+\xi_{3F}},\quad r_2 = \frac{\xi_{3F}-c}{\xi_{3F}+c},\quad t_2 = \frac{2\xi_{3F}}{\xi_{3F}+c},\\
\xi_{1F} &= \sqrt{\varepsilon_S^{\omega}-s^2},\quad \xi_{3F} = 3\xi_{6F} = \sqrt{\varepsilon_F^{\omega}-s^2},\\
\xi_{7F} &= \sqrt{\varepsilon_S^{3\omega}-s^2},\quad \xi_{9F} = -\sqrt{\varepsilon_S^{3\omega}-s^2},\\
\phi_{3F} &= \xi_{3F}k_0L_F,\quad \phi_{5F} = 3\xi_{3F}k_0L_F,\quad \phi_{6F} = 3\xi_{6F}k_0L_F,\quad \phi_{7F} = 3\xi_{7F}k_0L_F.
\end{aligned} \tag{C.46d}$$

Here the suffices S and F in these equations denote the substrate and the film, respectively.

Appendix D

SHG Maker fringes in a biaxial crystal

D.1 Parameters describing waves in the media

The basic concept and logical structure of the theoretical descriptions of Maker fringes in a biaxial crystal are the same as those used for the isotropic media, *i.e.* solving the Maxwell equations under proper boundary conditions. Nevertheless, the theory in a biaxial crystal (the most generalized case) is very complicated. It is worth that we derive these theoretical descriptions as appendix. Here we consider a case of SHG Maker fringes in a biaxial crystal. Multiple-reflections correction is not necessary, because the thickness of BNA crystal is on the order of 100 μm, much larger than the wavelength.

We assume that fundamental laser light that has an arbitrary polarization and it is incident on the slab of a biaxial NLO crystal. Figure D.1 shows definition of the coordinate axes and schematic diagrams of waves at frequency ω and 2ω that exist in the media. In general, plane waves that go through the anisotropic crystal can be classified into two types, namely ordinary and extraordinary waves. Specifically, Wave 3 and 4 in Fig. D.1 (b) are ordinary and extraordinary ω-waves, respectively. In the same way, Wave 8 and 9 in Fig. D.1 (c) are ordinary and extraordinary 2ω-free waves, respectively. Wave 5, 6, and 7 indicate ordinary, extraordinary, and *ordinary-extraordinary* 2ω-bound wave, respectively. The *ordinary-extraordinary* 2ω-bound wave will be mentioned in detail later. Hereafter we assume that Wave I is described as a plane wave:

$$\boldsymbol{E}_I(\boldsymbol{k}_I, \boldsymbol{r}) = \boldsymbol{E}_I\, \hat{\boldsymbol{e}}_I\, e^{i\boldsymbol{k}_I \cdot \boldsymbol{r}}. \tag{D.1}$$

The unit polarization vector $\hat{\boldsymbol{e}}_I$ has components e_{Ii} ($i = x,\ y,\ z$), and the alternative notation E_{Ii} ($i = x,\ y,\ z$) is sometimes used for the components of the field in order to avoid cumbersome normalization algebra.

The wavevectors $\boldsymbol{k}_I$ remain in the plane of incidence, so that $\boldsymbol{k}_{Iy} = 0$ for all I. Furthermore, to satisfy the boundary conditions over the whole entry and exit

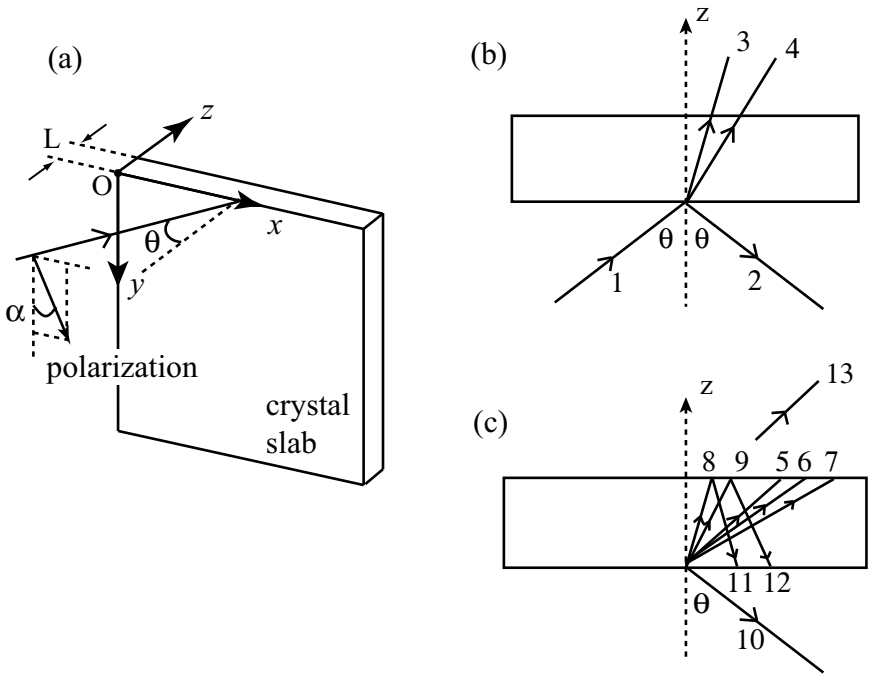

Figure D.1: (a) The definition of the coordinate axes and of the polarization. The schematic diagrams that represent the wave propagation of (b) the ω-waves and of (b) the 2ω-waves.

faces,

$$\begin{aligned} k_{Ix} &= k_{1x} \quad \text{when} \quad \Omega_I = \omega, \\ k_{Ix} &= 2k_{1x} \quad \text{when} \quad \Omega_I = 2\omega. \end{aligned} \tag{D.2}$$

The problem of determining the wavevectors of the free waves in the crystal, therefore, reduces to that of finding the $\boldsymbol{k}_{Iz}$ values. For the convenience, we will define dimensionless variables ξ_I, such that

$$\xi_I = \frac{k_{Iz}}{k_{vac}(\Omega_I)},$$

where

$$\begin{aligned} k_{vac}(\omega) &= \frac{\omega}{c_0} = k_1, \\ k_{vac}(2\omega) &= \frac{2\omega}{c_0} = 2k_1. \end{aligned} \tag{D.3}$$

In addition, parameters, which are used when boundary conditions are applied, are defined as

$$\gamma_I = -[k_{vac}(\Omega_I)]^{-1}(\boldsymbol{k}_I \times \hat{\boldsymbol{e}}_I)_y = se_{Iz} - \xi_I e_{Ix}. \tag{D.4}$$

Parameters that describe the waves in vacuum are summarized in Table D.1. It should be noted that $\sin\theta$ and $\cos\theta$ are respectively written as s and c hereafter.

Incident wave: I = 1	
$k_{1x} = k_1 s,\ k_{1z} = k_1 c$	$e_{1x} = c\sqrt{1 - e_{1y}^2},\ e_{1z} = -(s/c)e_{1x}$
$\xi_1 = c$	$\gamma_1 = -(e_{1x}/c)$
Reflected incident wave: I = 2	
$k_{2x} = k_1 s,\ k_{2z} = -k_1 c$	$e_{2x} = c\sqrt{1 - e_{2y}^2},\ e_{2z} = (s/c)e_{2x}$
$\xi_2 = -c$	$\gamma_2 = -(e_{2x}/c)$
Reflected SH wave: I = 10	
$k_{10x} = 2k_1 s,\ k_{10z} = -2k_1 c$	$e_{10x} = c\sqrt{1 - e_{10y}^2},\ e_{10z} = (s/c)e_{10x}$
$\xi_{10} = -c$	$\gamma_{10} = (e_{10x}/c)$
Transmitted SH wave: I = 13	
$k_{13x} = 2k_1 s,\ k_{13z} = 2k_1 c$	$e_{13x} = c\sqrt{1 - e_{13y}^2},\ e_{13z} = -(s/c)e_{13x}$
$\xi_{13} = c$	$\gamma_{13} = -(e_{13x}/c)$

Table D.1: Parameters of the external waves (I = 1, 2, 10, 13).

D.2 Solving the wave equations

In Appendix C, we defined the operator $\hat{\boldsymbol{F}}(\Omega)$ (see page 96), such that

$$\hat{\boldsymbol{F}}(\Omega)\mathcal{A} = [k_{\text{vac}}(\Omega_I)]^{-2}\left[\text{rot rot}\mathcal{A} - \left(\frac{\Omega}{c_0}\right)^2 \boldsymbol{\varepsilon}^{\Omega} : \mathcal{A}\right]. \tag{D.5}$$

By using this operator in analogy with Eq. (C.1) on page 96, the wave equations for the ω-, 2ω-free, and 2ω-bound waves in the media can be described as follows:

$$\begin{aligned}
\hat{\boldsymbol{F}}(\Omega)\boldsymbol{E}_I(\Omega) &= \hat{\boldsymbol{F}}(\Omega)\boldsymbol{E}_I\,\hat{\boldsymbol{e}}_I\,e^{i\boldsymbol{k}_I\cdot\boldsymbol{r}},\\
&= [k_{vac}(\Omega)]^{-2}\left[\frac{\partial^2}{\partial \boldsymbol{r}^2}(\boldsymbol{E}_I\,\hat{\boldsymbol{e}}_I\,e^{i\boldsymbol{k}_I\cdot\boldsymbol{r}}) - \left(\frac{\Omega}{c}\right)^2 \boldsymbol{\varepsilon}^{\Omega}\boldsymbol{E}_I(\Omega)\right],\\
&= [k_{vac}(\Omega)]^{-2}\left[\boldsymbol{k}_I^2\boldsymbol{E}_I(\Omega) - \left(\frac{\Omega}{c}\right)^2 \boldsymbol{\varepsilon}^{\Omega}\boldsymbol{E}_I(\Omega)\right],\\
&= \boldsymbol{F}(\xi_I, \boldsymbol{\varepsilon}^{\Omega})\boldsymbol{E}_I(\Omega),
\end{aligned} \tag{D.6}$$

where

$$\boldsymbol{F}(\xi_I, \boldsymbol{\varepsilon}^{\Omega}) = [k_{vac}(\Omega)]^{-2}\left[\boldsymbol{k}_I^2 - \left(\frac{\Omega}{c}\right)^2 \boldsymbol{\varepsilon}^{\Omega}\right]. \tag{D.7}$$

Now we express $\boldsymbol{F}(\xi_I, \boldsymbol{\varepsilon}^{\Omega})$ in a more useful form. For this purpose, (rot rot$\boldsymbol{E}$) can be expressed as

$$\text{rot rot}\boldsymbol{E} = \begin{bmatrix} k_{Iz}^2 E_x - k_{Iz}k_{Ix}E_x \\ k_{Iz}^2 E_y + k_{Ix}^2 E_y \\ -k_{Iz}k_{Ix}E_x + k_{Ix}^2 E_z \end{bmatrix}. \tag{D.8}$$

By dividing it by k_{vac}^2, we then obtain

$$\frac{1}{k_{vac}^2}\text{rot rot}\boldsymbol{E} = \begin{bmatrix} \xi^2 E_x - s\xi E_z \\ \xi^2 E_y + k_{Ix}^2 E_y \\ -s\xi E_x + s^2 E_z \end{bmatrix}. \tag{D.9}$$

Noting

$$\boldsymbol{\varepsilon} = \begin{bmatrix} \varepsilon_{xx} & \varepsilon_{xy} & \varepsilon_{xz} \\ \varepsilon_{yx} & \varepsilon_{yy} & \varepsilon_{yz} \\ \varepsilon_{zx} & \varepsilon_{zy} & \varepsilon_{zz} \end{bmatrix}, \tag{D.10}$$

$\hat{\boldsymbol{F}}\boldsymbol{E}$ can be recast as

$$\hat{\boldsymbol{F}}\boldsymbol{E} = \begin{bmatrix} \xi^2 - \varepsilon_{xx} & -\varepsilon_{xy} & -(\varepsilon_{xz} + \xi s) \\ -\varepsilon_{yx} & \xi^2 + s^2 - \varepsilon_{yy} & -\varepsilon_{yz} \\ -(\varepsilon_{xz} + \xi s) & -\varepsilon_{zy} & s^2 - \varepsilon_{zz} \end{bmatrix} \begin{bmatrix} E_x \\ E_y \\ E_z \end{bmatrix}. \tag{D.11}$$

Hence, $\boldsymbol{F}(\xi_I, \boldsymbol{\varepsilon}^{\Omega})$ is given by

$$\boldsymbol{F}(\xi, \boldsymbol{\varepsilon}) = \begin{bmatrix} \xi^2 - \varepsilon_{xx} & -\varepsilon_{xy} & -(\varepsilon_{xz} + \xi s) \\ -\varepsilon_{yx} & \xi^2 + s^2 - \varepsilon_{yy} & -\varepsilon_{yz} \\ -(\varepsilon_{xz} + \xi s) & -\varepsilon_{zy} & s^2 - \varepsilon_{zz} \end{bmatrix}. \tag{D.12}$$

Next the polarization vectors of Wave 3 and 4 satisfy Eq(D.7) in the form

$$\boldsymbol{F}(\xi_I, \boldsymbol{\varepsilon}^{\omega}) \cdot \hat{\boldsymbol{e}}_I = 0, \tag{D.13}$$

if

$$\det \boldsymbol{F}(\xi_I, \boldsymbol{\varepsilon}^{\omega}) = 0. \tag{D.14}$$

Equation (D.14) is Fresnel's equation of wave normals, which is expressed in the laboratory coordinate. Analogously, the free SH waves 8, 9, 11, and 12 are obtained from

$$\boldsymbol{F}(\xi_I, \varepsilon^{2\omega}) \cdot \hat{\boldsymbol{e}}_I = 0, \tag{D.15}$$

if

$$\det \boldsymbol{F}(\xi_I, \boldsymbol{\varepsilon}^{2\omega}) = 0. \tag{D.16}$$

The two positive roots of the associated determinant give ξ_8 and ξ_9 and the two negative roots ξ_{11} and ξ_{12}. Consequently, the corresponding wave equation is given by

$$\begin{aligned} \hat{\boldsymbol{F}}(2\omega)\boldsymbol{E}(2\omega) &= (2k_1)^{-1}\boldsymbol{P}^{+}(2\omega), \\ &= \boldsymbol{P}(2\omega), \\ &= \boldsymbol{\chi} : (\boldsymbol{E}_3 + \boldsymbol{E}_4)(\boldsymbol{E}_3 + \boldsymbol{E}_4), \end{aligned} \tag{D.17}$$

where

$$\begin{aligned} P_i(2\omega) &= \sum \chi_{ijk}(E_{3j} + E_{4k})(E_{3k} + E_{4j}), \\ &= \chi_{ijk}(E_{3j}E_{3k} + E_{4j}E_{4k} + E_{3k}E_{4j} + E_{3j}E_{4k}), \\ &= \sum_{I=5}^{7} p_{Ii} e^{2i\xi_I k_{1z}} E_1^2, \end{aligned} \tag{D.18}$$

and

$$\xi_5 = \xi_3, \quad \xi_6 = \xi_4, \quad \xi_7 = \frac{1}{2}(\xi_3 + \xi_4). \tag{D.19}$$

Here p_{Ii} in Eq. (D.18) is given by

$$p_{Ii} = \chi_{ijk}\pi_{Ijk}t_I. \tag{D.20}$$

π and t_I are projection factor and transmission coefficients, respectively. It should be noted that ξ_7 is the wavevector of *ordinary-extraordinary*, which was mentioned above. This type of wave is a special case, and it is usually ignored by setting the angle α to be 0 or 90°. Equation (D.17) is finally expressed as

$$\boldsymbol{F}(2\omega)\boldsymbol{E}(2\omega) = \sum_{I=5}^{7} \boldsymbol{p}_I e^{2i\xi_I k_{1z}} E_1^2. \tag{D.21}$$

By solving Eq. D.21 separately for each polarization wave, we have

$$\boldsymbol{F}(2\omega)\boldsymbol{E}(2\omega) = \boldsymbol{p}_I e^{2i\xi_I k_{1z}} E_1^2, \quad I = 5 - 7, \tag{D.22}$$

or

$$\boldsymbol{F}(\xi_I, \boldsymbol{\varepsilon}^{2\omega})\boldsymbol{E}_I = \boldsymbol{p}_I E_1^2, \tag{D.23}$$

$$\frac{\boldsymbol{E}_I}{E_1^2} = \boldsymbol{F}^{-1} \cdot \boldsymbol{p}_I = (\det \boldsymbol{F})^{-1}\boldsymbol{F}^A\boldsymbol{p}_I, \tag{D.24}$$

where $\boldsymbol{F}^A$ is the adjoint matrix of $\boldsymbol{F}$. It is given by

$$\boldsymbol{F}^A = \begin{bmatrix} e & b & c \\ b & f & d \\ c & d & g \end{bmatrix}, \tag{D.25}$$

$$\begin{aligned} b &= \varepsilon_{yz}(s\xi + \varepsilon_{xz}) + \varepsilon_{xy}(s^2 - \varepsilon_{zz}), & c &= \varepsilon_{xy}\varepsilon_{yz} + F_O(s\xi + \varepsilon_{xz}), \\ d &= \varepsilon_{xy}(s\xi + \varepsilon_{xz}) + \varepsilon_{yz}(\xi^2 - \varepsilon_{xx}), & e &= F_O(s^2 - \varepsilon_{zz}) - \varepsilon_{yz}^2, \\ f &= F_E - 2s\xi\varepsilon_{xz} - \varepsilon_{xz}^2, & g &= F_O(\xi^2 - \varepsilon_{xx}) - \varepsilon_{xy}^2, \end{aligned}$$

where

$$F_O = \xi^2 + s^2 - \varepsilon_{yy}, \tag{D.26}$$

$$F_E = (\xi^2 - \varepsilon_{xx})(s^2 - \varepsilon_{zz}) - (s\xi)^2. \tag{D.27}$$

D.3 Boundary conditions

The concept of boundary conditions that will be used here is the same as that used in the case of isotropic media, which is described in Appendix C. We have three boundary conditions (i) for ω-wave at $z = 0$, (ii) for 2ω-wave at $z = 0$, and (iii) for 2ω-wave at $z = L$.

(i) Boundary conditions for ω-wave at $z = 0$.

$$\begin{cases} E_1 e_{1x} + E_2 e_{2x} = E_3 e_{3x} + E_4 e_{4x} & \text{(a)} \\ E_1 e_{1y} + E_2 e_{2y} = E_3 e_{3y} + E_4 e_{4y} & \text{(b)} \\ \xi_1 E_1 e_{1y} + \xi_2 E_2 e_{2y} = \xi_3 E_3 e_{3y} + \xi_4 E_4 e_{4y} & \text{(c)} \\ \gamma_1 E_1 + \gamma_2 E_2 = \gamma_3 E_3 + \gamma_4 E_4 & \text{(d)} \end{cases} \tag{D.28}$$

These equations give two equations,

$$\begin{bmatrix} 2ce_{1y} \\ 2e_{1x} \end{bmatrix} = \begin{bmatrix} (\xi_3 + c)e_{3y} & (\xi_4 + c)e_{4y} \\ e_{3x} - c\gamma_3 & e_{4x} - c\gamma_4 \end{bmatrix} \cdot \begin{bmatrix} E_3/E_1 \\ E_4/E_1 \end{bmatrix}. \tag{D.29}$$

Here, we will utilize following relations: if we have

$$\begin{bmatrix} M_{11} & M_{12} \\ M_{21} & M_{22} \end{bmatrix} \cdot \begin{bmatrix} x_1 \\ x_2 \end{bmatrix} = \begin{bmatrix} m_1 \\ m_2 \end{bmatrix}, \tag{D.30}$$

the solutions can be given by

$$\begin{aligned} \begin{bmatrix} m_1 \\ m_2 \end{bmatrix} &= \frac{1}{\det M} \begin{bmatrix} M_{22} & -M_{12} \\ -M_{21} & M_{11} \end{bmatrix} \cdot \begin{bmatrix} y_1 \\ y_2 \end{bmatrix}, \\ &= \frac{1}{\det M} \begin{bmatrix} \begin{vmatrix} y_1 & M_{12} \\ y_2 & M_{22} \end{vmatrix} \\ \begin{vmatrix} M_{11} & y_1 \\ M_{21} & y_2 \end{vmatrix} \end{bmatrix}, \\ &= \frac{1}{\det M} \begin{bmatrix} M_1 \\ M_2 \end{bmatrix}, \end{aligned} \tag{D.31}$$

where

$$\begin{aligned} \begin{bmatrix} m_1 \\ m_2 \end{bmatrix} &= \sum_I \begin{bmatrix} m_{1I} \\ m_{2I} \end{bmatrix}, \\ &= \sum_I \frac{1}{\det M} \begin{bmatrix} M_{1I} \\ M_{2I} \end{bmatrix}, \end{aligned} \tag{D.32}$$

and

$$M_{1I} = \begin{vmatrix} m_{1I} & M_{12} \\ m_{2I} & M_{22} \end{vmatrix}, \quad M_{2I} = \begin{vmatrix} M_{11} & m_{1I} \\ M_{21} & m_{2I} \end{vmatrix}. \tag{D.33}$$

By using these relations, Eq. (D.29) can be recast as

$$\begin{bmatrix} E_3/E_1 \\ E_4/E_1 \end{bmatrix} = \frac{1}{U}\begin{bmatrix} U_1 \\ U_2 \end{bmatrix}, \tag{D.34}$$

where

$$\begin{aligned} U_1 &= \begin{vmatrix} 2ce_{1y} & (\xi_4 + c)e_{4y} \\ 2e_{1x} & e_{4x} - c\gamma_4 \end{vmatrix}, \quad U_2 = \begin{vmatrix} (\xi_3 + c)e_{3y} & 2ce_{1y} \\ (e_{3x} - c\gamma_3 & 2e_{1x} \end{vmatrix}, \\ U &= \begin{vmatrix} (\xi_3 + c)e_{3y} & (\xi_4 + c)e_{4y} \\ (e_{3x} - c\gamma_3 & e_{4x} - c\gamma_4 \end{vmatrix}, \quad \boldsymbol{u} = \begin{bmatrix} 2ce_{1y} \\ 2e_{1x} \end{bmatrix}. \end{aligned} \tag{D.35}$$

The transmission coefficients t_I ($I = 5, 7$) are given by

$$t_5 = \left(\frac{U_1}{U}\right)^2, \quad t_6 = \left(\frac{U_2}{U}\right)^2, \quad t_7 = \left(\frac{U_1 U_2}{U^2}\right). \tag{D.36}$$

(ii) Boundary conditions for 2ω-wave at $z = 0$.

$$\begin{cases} E_{10}e_{10x} = E_8 e_{8x} + E_9 e_{9x} + \sum_{I=5}^{7}(E_{Ix}/E_1^2)E_1^2 & \text{(a)} \\ E_{10}e_{10y} = E_8 e_{8y} + E_9 e_{9y} + \sum_{I=5}^{7}(E_{Iy}/E_1^2)E_1^2 & \text{(b)} \\ \xi_{10}E_{10}e_{10y} = \xi_8 E_8 e_{8y} + \xi_9 E_9 e_{9y} + \sum_{I=5}^{7}\xi_I(E_{Iy}/E_1^2)E_1^2 & \text{(c)} \\ \gamma_{10}E_{10} = \gamma_8 E_8 + \gamma_9 E_9 + \sum_{I=5}^{7}[s(E_{Iz}/E_1^2) - \xi_I(E_{Ix}/E_1^2)]E_1^2 & \text{(d)} \end{cases} \tag{D.37}$$

In the same way of case (i), we have

$$\begin{bmatrix} E_8/E_1^2 \\ E_9/E_1^2 \end{bmatrix} = \frac{1}{V}\begin{bmatrix} \sum_{I=5}^{7}\frac{V_{1I}}{V} \\ \sum_{I=5}^{7}\frac{V_{2I}}{V} \end{bmatrix}, \tag{D.38}$$

(D.39)

where

$$\begin{aligned} V_{1I} &= \begin{vmatrix} v_{1I} & (\xi_9 + c)e_{9y} \\ v_{2I} & e_{9x} - c\gamma_9 \end{vmatrix}, \quad V_{2I} = \begin{vmatrix} (\xi_8 + c)e_{8y} & v_{1I} \\ e_{8x} - c\gamma_8 & v_{2I} \end{vmatrix}, \\ V &= \begin{vmatrix} (\xi_8 + c)e_{8y} & (\xi_9 + c)e_{9y} \\ e_{8x} - c\gamma_8 & e_{9x} - c\gamma_9 \end{vmatrix}, \\ \boldsymbol{v}_I &= -\begin{bmatrix} (\xi_I + c)E_{Iy}/E_1^2 \\ (1 + c\xi_I)E_{Ix}/E_1^2 - csE_{Iz}/E_1^2 \end{bmatrix} = \begin{bmatrix} v_{1I} \\ v_{2I} \end{bmatrix}. \end{aligned} \tag{D.40}$$

(iii) Boundary conditions for 3ω-wave at $z = L$.

This case can also be solved in analogy with Eq. (D.37), except that we need to take account of phase shift $f_I = \exp(2ik_I\xi_I k_z L)$. We then have

$$\begin{cases} E_{13}e_{13x}f_{13} - E_{11}e_{11x}f_{11} - E_{12}e_{12x}f_{12} = \sum_{I=5}^{9} f_I(E_{Ix}/E_1^2)E_1^2 & \text{(a)} \\ E_{13}e_{13y}f_{13} - E_{11}e_{11y}f_{11} - E_{12}e_{12y}f_{12} = \sum_{I=5}^{9} f_I(E_{Iy}/E_1^2)E_1^2 & \text{(b)} \\ \xi_{13}E_{13}e_{13y}f_{13} - \xi_{11}E_{11}e_{11y}f_{11} - \xi_{12}E_{12}e_{12y}f_{12} = \sum_{I=5}^{9}\xi_I f_I(E_{Iy}/E_1^2)E_1^2 & \text{(c)} \\ \gamma_{13}E_{13}f_{13} - \gamma_{11}E_{11}f_{11} - \gamma_{12}E_{12}f_{12} = \sum_{I=5}^{9} f_I[s(E_{Iz}/E_1^2) - \xi_I(E_{Ix}/E_1^2)]E_1^2 & \text{(d)} \end{cases} \tag{D.41}$$

Hence we obtain

$$\begin{bmatrix} E_1 1/E_1^2 \\ E_1 2/E_1^2 \end{bmatrix} = \frac{1}{V} \begin{bmatrix} \sum_{I=5}^{7} \frac{V_{1I}}{V} \\ \sum_{I=5}^{7} \frac{V_{2I}}{V} \end{bmatrix}, \tag{D.42}$$

where

$$\begin{aligned} W_{1I} &= \begin{vmatrix} w_{1I} & (c-\xi_{12})e_{12y} \\ w_{2I} & e_{12x}+c\gamma_{12} \end{vmatrix}, \quad W_{2I} = \begin{vmatrix} (c-\xi_{11})e_{11y} & w_{1I} \\ e_{11x}+c\gamma_{11} & w_{2I} \end{vmatrix}, \\ W &= \begin{vmatrix} (c-\xi_{11})e_{11y} & (c-\xi_{12})e_{12y} \\ e_{11x}+c\gamma_{11} & e_{12x}+c\gamma_{12} \end{vmatrix}, \\ \boldsymbol{w}_I &= -\begin{bmatrix} (c-\xi_I)E_{Iy}/E_1^2 \\ (1-c\xi_I)E_{Ix}/E_1^2 + csE_{Iz}/E_1^2 \end{bmatrix} = \begin{bmatrix} w_{1I} \\ w_{2I} \end{bmatrix}. \end{aligned} \tag{D.43}$$

Now we are ready to calculate E_{13i} using Eq. (D.41) (a) and (b). It is given by

$$\begin{aligned} E_{13i}e_{13i}f_{13} &= E_1^2 \sum_{I=5}^{9} f_I \left(\frac{W_{1I}}{W} e_{11i} + \frac{W_{2I}}{W} e_{12i} + \frac{E_{Ii}}{E_1^2} \right), \\ &= E_1^2 \sum_{I=5}^{9} f_I Q_{Ii}, \end{aligned} \tag{D.44}$$

where

$$Q_{Ii} = \left(\frac{W_{1I}}{W} e_{11i} + \frac{W_{2I}}{W} e_{12i} + \frac{E_{Ii}}{E_1^2} \right), \quad i = x,\ y\,. \tag{D.45}$$

Hereafter, the repeated index summation convention is implied over the coordinate indices ($i,\ j,\ k,\ etc$) but not over the indices I and α that label different waves.

Next, Wave 8 and 9 are expanded with $I = 5$–7:

$$E_\alpha = \sum_{I=5}^{7} A_{\alpha Ij} E_{Ij}. \tag{D.46}$$

Then E_{13i} is given by the superposition of Waves 5–9:

$$\begin{aligned} E_{13i} &= \sum_{I=5}^{9} f_I B_{Iij} E_{Ij}, \\ &= \sum_{I=5}^{7} f_I B_{Iij} E_{Ij} + \sum_{I=8}^{9} f_\alpha B_{\alpha ij} E_{\alpha j}, \\ &= \sum_{I=5}^{7} f_I B_{Iij} E_{Ij} + \sum_{I=8}^{9} f_\alpha B_{\alpha ij} \left(\sum_{I=5}^{7} A_{\alpha Ik} E_{Ik} e_{\alpha k} \right), \\ &= \sum_{I=5}^{7} \left(f_I B_{Iij} + f_8 B_{8ik} A_{8Ik} e_{8k} + f_9 B_{9ik} A_{9Ik} e_{9k} \right) E_{Ik}, \end{aligned} \tag{D.47}$$

where we have introduced

$$C_{\alpha i} = B_{\alpha ik} e_{\alpha k}. \tag{D.48}$$

In addition, E_{Ik} , by using Eqs. (D.20) and (D.24), is given by

$$E_{Ik} = E_1^2 F_I^{-1} F_{Ijk}^A \chi_{klm} \pi_{Ilm} t_I. \tag{D.49}$$

Thus E_{13i} is expressed in terms of the bound waves:

$$E_{13i} = \sum_{I=5}^{7} \left(f_I B_{Iij} + f_8 B_{8ik} A_{8Ik} e_{8k} + f_9 B_{9ik} A_{9Ik} e_{9k} \right) E_1^2 F_I^{-1} F_{Ijk}^A \chi_{klm} \pi_{Ilm} t_I, \tag{D.50}$$

where

$$F_I = \mathrm{det}\mathbf{F}(\xi_\mathrm{I}, \varepsilon^{2\omega}), \quad \mathrm{F}_{\mathrm{Ijk}}^{\mathrm{A}} = \mathrm{F}_{\mathrm{jk}}(\xi_\mathrm{I}, \varepsilon^{2\omega}). \tag{D.51}$$

We finally obtain

$$E_{13i} = E_1^2 \sum_{I=5}^{7} \left(f_I S_{iIk} + f_8 C_{8ik} T_{8Ik} + f_9 C_{9i} T_{9Ik} \right) F_I^{-1} X_{Ik} t_I, \tag{D.52}$$

where

$$S_{iIk} = B_{Iij} F_{Ijk}^A, \tag{D.53}$$

$$T_{\alpha Ik} = A_{\alpha Ij} F_{Ijk}^A, \tag{D.54}$$

$$C_{\alpha i} = B_{\alpha ik} e_{\alpha k}, \tag{D.55}$$

$$X_{Ik} = \pi_{Ilm} \chi_{klm}. \tag{D.56}$$

Practical expressions of respective coefficients are summarized in Table D.2. The experimental physical quantity that we observe is the intensity of the transmitted SH wave I_{SHG}, therefore

$$I_{\mathrm{SHG}} = |E_{13i}|^2. \tag{D.57}$$

D.4 Theoretical formulae in the real experimental setup

A crystal of BNA has *orthorhombic* lattice structure, so that all of the non-diagonal components of the dielectric tensor vanish in this case:

$$\varepsilon_{ij}^{\Omega} = \varepsilon_i^{\Omega} \delta_{ij}. \tag{D.58}$$

Consequently, E_{13i} is given by

$$E_{13x} = E_1^2 \sum_{I=5}^{7} \Big[\left(S_{xIx} X_{Ix} + S_{xIz} X_{Iz} \right) f_I + f_9 C_{9x} \left(T_{9Ix} X_{Ix} + T_{9Iz} X_{IZ} \right) \Big] F_I^{-1} t_I, \tag{D.59}$$

$$E_{13y} = E_1^2 \sum_{I=5}^{7} \left(S_{yIy} f_I + f_8 C_{8y} T_{8Iy} \right) F_I^{-1} X_{Iy} t_I. \tag{D.60}$$

$$U = (c+\xi_3)e_{3y}(e_{4x}-c\gamma_4) - (c+\xi_4)e_{4y}(e_{3x}-c\gamma_3)$$
$$U_1 = 2[ce_{1y}(e_{4x}-c\gamma_4) - e_{1x}(c+\xi_4)e_{4y}]$$
$$U_2 = 2[e_{1x}(c+\xi_3)e_{3y} - ce_{1y}(e_{3x}-c\gamma_3)]$$
$$t_5 = (U_1/U)^2,\ t_6 = (U_2/U)^2,\ t_7 = U_1U_2/U^2$$
$$\pi_{5jk} = e_{3j}e_{3k},\ \pi_{6jk} = e_{4j}e_{4k},\ \pi_{7jk} = e_{3j}e_{4k} + e_{4j}e_{3k}$$

$$V = (c+\xi_8)e_{8y}(e_{9x}-c\gamma_9) - (c+\xi_9)e_{9y}(e_{8x}-c\gamma_8)$$

$$A_{8Ix} = (1/V)(c+\xi_9)e_{9y}(+c\xi_I)$$
$$A_{8Iy} = -(1/V)(c+\xi_I)(e_{9x}-c\gamma_9)$$
$$A_{8Iz} = -(1/V)(c+\xi_9)e_{9y}sc$$

$$A_{9Ix} = -(1/V)(c+\xi_8)e_{8y}(+c\xi_I)$$
$$A_{9Iy} = (1/V)(c+\xi_I)(e_{8x}-c\gamma_8)$$
$$A_{9Iz} = (1/V)(c+\xi_8)e_{8y}sc$$

$$W = e_{11y}(c-\xi_{11})(e_{12x}+c\gamma_{12}) - (c-\xi_{12})e_{12y}(e_{11x}+c\gamma_{11})$$

Let
$$g_{1i} = e_{11i}(c-\xi_{12})e_{12y} - e_{12i}(c-\xi_{11})e_{11y}$$
$$g_{2i} = e_{11i}(e_{12x}+c\gamma_{12}) - e_{12i}(e_{11x}+c\gamma_{11})$$

then

$$B_{Iix} = \delta_{ix} + (1/W)g_{1i}(1-c\xi_I),\ B_{Iiy} = \delta_{iy} - (1/W)g_{2i}(c-\xi_I),\ B_{Iiz} = (sc/W)g_{1i}$$

$$C_{\alpha i} = e_{\alpha x}\delta_{ix} + e_{\alpha y}\delta_{iy} + (1/W)[g_{1i}(1-c\xi_\alpha)e_{\alpha x} - g_{2i}(c-\xi_\alpha)e_{\alpha y} + g_{1i}sce_{\alpha z}]$$

Table D.2: Practical expressions of the coefficients in Eqs. (D.52)–(D.56)

Case 1: the fundamental wave is ordinary

In this case, we are able to set $I = 5$ in Eqs. (D.59) and (D.60):

$$E_{13x} = E_1^2 \sum_{I=5}^{7}\left[\left(S_{x5x}\chi_{xyy} + S_{x5z}\chi_{zyy}\right) f_5 + f_9C_{9x}\left(T_{95x}\chi_{xyy} + T_{95z}\chi_{zyy}\right)\right]F_5^{-1}t_5, \tag{D.61}$$

$$E_{13y} = E_1^2 \sum_{I=5}^{7}\left(S_{y5y}f_5 + f_8C_{8y}T_{85y}\right)F_5^{-1}\chi_{yyy}t_5, \tag{D.62}$$

where

$$X_{5i} = \pi_{5lm}\chi_{ilm} = e_{3l}e_{3m}\chi_{ilm} = \delta_{ly}\delta_{my}\chi_{ilm} = \chi_{iyy}. \tag{D.63}$$

In case that the fundamental and SH waves are both ordinary, we have

$$\begin{aligned} I_{OO} &= |E_{13y}|^2 \\ &= E_1^4(\chi_{yyy})^2 t_5^2 F_5^{-2} \times (S_{y5y} f_5 + f_8 C_{8y} T_{85y})(S_{y5y} f_5^* + f_8^* C_{8y} T_{85y}), \\ &= E_1^4(\chi_{yyy})^2 t_5^2 F_5^{-2} \times \left[S_{y5y}^2 + (C_{8y} T_{85y})^2 + 2 S_{y5y} C_{8y} T_{85y} (f_5 f_8^* + f_8 f_5^*) \right], \\ &\approx -4 E_1^4(\chi_{yyy})^2 t_5^2 F_5^{-2} S_{y5y} C_{8y} T_{85y} \sin^2 [k_1 L(\xi_5 - \xi_8)], \\ &= 8 E_1^4(\chi_{yyy})^2 \left(\frac{2c}{c + \xi_3} \right)^4 \frac{\xi_8(\xi_5 + \xi_8)(\xi_5 + c)}{(\xi_5^2 - \xi_8^2)^2 (c + \xi_8)^3} \sin^2 [k_1 L(\xi_5 - \xi_8)]. \end{aligned} \tag{D.64}$$

Analogously,

$$\begin{aligned} I_{OE} \approx\ & 8 E_1^4(\chi_{yyy})^2 \frac{\varepsilon_x^{2\omega}}{(\varepsilon_z^{2\omega})^2} \left(\frac{2c}{c + \xi_3} \right)^4 \frac{\xi_9(\xi_5 + \xi_9)}{(\xi_9 + c\varepsilon_x^{2\omega})^3} \\ & \times \left[\frac{\varepsilon_z^{2\omega}}{\varepsilon_x^{2\omega}} (\xi_9^2 + c\varepsilon_x^{2\omega} \xi_5) \chi_{xyy} - s(\xi_5 + c\varepsilon_x^{2\omega}) \chi_{zyy} \right] \\ & \times (\varepsilon_z^{2\omega} \xi_9 \chi_{xyy} - s\varepsilon_x^{2\omega} \chi_{zyy}) \frac{\sin^2 [k_1 L(\xi_5 - \xi_9)]}{(\xi_5^2 - \xi_9^2)^2}. \end{aligned} \tag{D.65}$$

Case 2: the fundamental wave is extraordinary

In this case, we are able to set $I = 6$ in Eqs. (D.59) and (D.60):

$$\begin{aligned} I_{EE} \approx\ & 8 E_1^4 \frac{\varepsilon_x^{2\omega}}{(\varepsilon_z^{2\omega})^2} \left(\frac{2c}{\xi_4 + c\varepsilon_x^{2\omega}} \right)^4 \frac{\xi_9(\xi_6 + \xi_9)}{(\xi_9 + c\varepsilon_x^{2\omega})^3} \\ & \times (\xi_9 \varepsilon_z^{2\omega} X'_{6x} - \varepsilon_x^{2\omega} X'_{6z}) \left[\frac{\varepsilon_z^{2\omega}}{\varepsilon_x^{2\omega}} (\xi_9^2 + c\varepsilon_x^{2\omega} \xi_6) X'_{6x} - s(\xi_6 + c\varepsilon_x^{2\omega}) X'_{6z} \right] \\ & \times \frac{\sin^2 [k_1 L(\xi_6 - \xi_9)]}{(\xi_6^2 - \xi_9^2)^2}, \end{aligned} \tag{D.66}$$

$$I_{EO} \approx 8 E_1^4 (X'_{6y})^2 \left(\frac{2c}{\xi_4 + c\varepsilon_x^{\omega}} \right)^4 \frac{\xi_8(\xi_6 + \xi_8)(\xi_6 + c)}{(c + \xi_8)^3 (\xi_6^2 - \xi_8^2)^2} \sin^2 [k_1 L(\xi_6 - \xi_8)], \tag{D.67}$$

where

$$X'_{6i} = \xi_4^2 \chi_{ixx} - 2 \left(\frac{\varepsilon_x^{\omega}}{\varepsilon_z^{\omega}} \right) s \xi_4 \chi_{ixy} + \left(\frac{\varepsilon_x^{\omega}}{\varepsilon_z^{\omega}} \right)^2 s^2 \chi_{izz}. \tag{D.68}$$

In Chapter 5, the fringes derived from d_{333} was measured at *OO* setup in setting the rotational axis being parallel to the Z axis. The fringes derived from d_{322} and d_{311} were measured at *OE* setup in setting the rotational axis being parallel to the Y and X axis, respectively. We thus obtain, for d_{333},

$$\begin{aligned} I_{OO} &= A \left(\frac{2c}{c + \xi_3} \right)^4 \frac{\xi_8(\xi_3 + \xi_8)(c + \xi_3)}{(c + \xi_8)^3 (\xi_3^2 - \xi_8^2)^2} \sin^2 [k_1(\xi_3 - \xi_8) L] \\ A &= 32 E_1^4 d_{333}^2, \quad \xi_3 = \sqrt{\varepsilon_Z^{\omega} - s^2}, \quad \xi_8 = \sqrt{\varepsilon_Z^{2\omega} - s^2}, \end{aligned} \tag{D.69}$$

for d_{322},

$$I_{OE} = A\left(\frac{2c}{c+\xi_3}\right)^4 c^2 s^2 \frac{\varepsilon_X^{2\omega}}{(\varepsilon_Z^{2\omega})^2} \frac{\xi_9(\xi_3+\xi_9)(\xi_3+c\varepsilon_X^{2\omega})}{(\xi_9+c\varepsilon_X^{2\omega})^3(\xi_3^2-\xi_9^2)^2} \sin^2[k_1(\xi_3-\xi_9)L)],$$

$$A = 32E_1^4 d_{322}^2, \quad \xi_3 = \sqrt{\varepsilon_Y^{\omega} - s^2}, \quad \xi_9 = \sqrt{\frac{\varepsilon_X^{2\omega}}{\varepsilon_Z^{2\omega}}(\varepsilon_Z^{2\omega} - s^2)}, \tag{D.70}$$

and, for d_{311},

$$I_{OE} = A\left(\frac{2c}{c+\xi_3}\right)^4 c^2 s^2 \frac{\varepsilon_Y^{2\omega}}{(\varepsilon_Z^{2\omega})^2} \frac{\xi_9(\xi_3+\xi_9)(\xi_3+c\varepsilon_Y^{2\omega})}{(\xi_9+c\varepsilon_Y^{2\omega})^3(\xi_3^2-\xi_9^2)^2} \sin^2[k_1(\xi_3-\xi_9)L],$$

$$A = 32E_1^4 d_{311}^2, \quad \xi_3 = \sqrt{\varepsilon_X^{\omega} - s^2}, \quad \xi_9 = \sqrt{\frac{\varepsilon_Y^{2\omega}}{\varepsilon_Z^{2\omega}}(\varepsilon_Z^{2\omega} - s^2)}. \tag{D.71}$$

References

[1] H. van Amerongen, L. Valkunas, and R. van Grondelle, *Photosynthetic Excitons* (World Scientific, London, 2000).

[2] G. McDermott, S. M. Prince, A. A. Freer, A. M. Hawthornthwaite-Lawless, M. Z. Papiz, R. J. Cogdell, and N. W. Isaacs, Nature (London) **374**, 517 (1995).

[3] J. L. Herek, W. Wohlleben, R. J. Cogdell, D. Zeidler, and M. Motzkus, Nature, (London) **417**, 533 (2002).

[4] P. Kukura, D. W. McCamant, S. Yoon, D. B. Wandschneider, R. A. Mathies, Science **310**, 1006 (2005).

[5] L. M. Frutos, T. Andruniow, F. Santoro F, N. Ferre, M. Olivucci, Proc. Natl. Acad. Sci. U.S.A. **104**, 7764 (2007).

[6] *The Photochemistry of Carotenoids*, edited by H. A. Frank, A. J. Young, G. Britton, and R. J. Cogdell (Kluwer Academic, Netherlands, 1999), references therein.

[7] *Nonlinear Optical Materials*, edited by H. Kuhn and J. Robillard (CRC Press, Florida, 1992).

[8] H. Dodziuk, *Introduction to Supramolecular Chemistry* (Kluwer Academic, Netherlands, 2002).

[9] J. W. Steed, D. R. Turner, K. Wallace, *Core Concepts in Supramolecular Chemistry and Nanochemistry* (Wiley, Chichester England, 2007).

[10] P. A. Loach, Proc. Natl. Acad. Sci. U.S.A. **97**, 5016 (2000).

[11] R. E. Blankeship, *Molecular mechanisms of photosynthesis* (Blackwell Science, Oxford, 2002).

[12] M. Y. Okamura and G. Feher, in *Anoxigenic photosynthetic bacteria*, edited by R. E. Blankeship, M. T. Madigan, and C. E. Bauer, (Kluwer Academic Publishers, Netherlands, 1995).

[13] V. Sundström, T. Pullerits, and R. van Grondelle, J. Phys. Chem. B **103**, 2327 (1999).

[14] K. Yanagi, his PhD dissertation in 2004 at Osaka City University, Japan.

[15] T. Förster, in *Delocalization Exciton and Excitation Transfer; Modern Quantum Chemistry, Vol. III*, edited by O. Sinanoglu (Academic Press, New York, 1965).

[16] D. Zigmantas, E. L. Read, T. Mančal, A. T. Gardiner, R. J. Cogdell, and G. R. Fleming, Proc. Natl. Acad. Sci. U.S.A. **103**, 12672 (2006).

[17] T. Renger, in *Primary processes of photosynthesis - Part 1*, edited by G. Renger (RSC Publishing, Cambridge, 2008).

[18] H. Lee, Y.-C. Cheng, and G. R. Fleming, Science **316**, 1462 (2007).

[19] G. S. Engel, T. R. Calhoun, E. L. Read, T.-K. Ahn, T. Mančal, Y.-C. Cheng, R. E. Blankenship, and G. R. Fleming, Nature (London) **446**, 782 (2007).

[20] T. Brixner, J. Stenger, H. M. Vaswani, M. Cho, R. E. Blankenship, and G. R. Fleming, Nature (London) **434**, 625 (2005).

[21] K. Yanagi, H. Hashimoto, A. T. Gardiner, and R. J. Cogdell, J. Phys. Chem. B **108**, 10334 (2004).

[22] K. Yanagi, M. Shimizu, H. Hashimoto, A. T. Gardiner, A. W. Roszak, and R. J. Cogdell, J. Phys. Chem. B **109**, 992 (2005).

[23] R. R. Tykwinski, U. Gubler, R. E. Martin, F. Diederich, C. Bosshard, and P. Günter, J. Phys. Chem. B **102**, 4451 (1998).

[24] S. R. Marder, C. B. Gorman, B. G. Tiemann, J. W. Perry, G. Bourhill, and K. Mansour, Science **261**, 186 (1993).

[25] S. R. Marder, W. E. Torruellas, M. Blanchard-Desce, V. Rocci, G. I. Stegeman, S. Gilmour, J.-L. Brédas, J. Li, G. U. Bublitz, and S. G. Boxer, Science **276**, 1233 (1997).

[26] M. G. Kuzyk, Phys. Rev. Lett. **85**, 1218 (2000); Opt. Lett. **25**, 1183 (2000).

[27] J. Zhou, M. G. Kuzyk, and D. S. Watkins, Opt. Lett. **31**, 2891 (2006).

[28] *Femtosecond Technology: From Basic Research to Application Prospects*, edited by T. Kamiya, F. Saito, O. Wada, and H. Yajima (Springer, Berlin, 1999).

[29] B. Ferguson and X.-C. Zhang, Nature Materials **1**, 26 (2002).

[30] C. Zandonella, Science **424**, 721 (2003).

[31] S. Wang, B. Ferguson, D. Abbot, and X.-C. Zhang, J. Biol. Phys. **29**, 247 (2003).

[32] R. Parthasarathy, T. Globus, T. Khromova, N. Swami, and D. Woolard, Appl .Phys. Lett. **87**, 113901 (2005).

[33] T. Globus, M. Bykhovskaia, D. Woolard, and B. Gelmont, J. Phys. D **36**, 1314 (2003).

[34] R. A. Kaindl, M. A. Carnahan, D. Hägele, R. Lövenich, and D. S. Chemla, Nature, (London) **423**, 734 (2003).

[35] R. A. Brooker, Z. Du, J. D. Blundy, S. P. Kelley, N. L. Allan, B. J. Wood, E. M. Chamorro, J.-A. Wartho, and J. A. Purton, Nature, (London) **414**, 286 (2001).

[36] R. Huber, C. Küblerm S. Tübel, A. Leitenstorfer, Q. T. Vu, H. Haug, F. Köhler, and M.-C, Amann, Phys. Rev. Lett. **94**, 027401 (2005).

[37] C. W. Luo, K. Reimann, M. Woerner, T. Elsaesser, R. Hey, and K. H. Ploog, Phys. Rev. Lett. **92**, 047402 (2004).

[38] R. Huber, B. A. Schmid, Y. R. Shen, D. S. Chemla, and R. A. Kaindl, Phys. Rev. Lett. **96**, 017402 (2006).

[39] C. Sirtori, Nature, (London) **417**, 132 (2002).

[40] L. R. Elias, G. Ramian, J. Hu, and A. Amir, Phys. Rev. Lett. **57**, 424 (1986).

[41] G. L. Carr, M. C. Martin, W. R. McKinney, K. Jordan, G. R. Neil, and G. P. Williams, Nature, (London) **420**, 153 (2002).

[42] J. Zyss and G. Berthier, J. Chem. Phys. **77**, 3653 (1982).

[43] T. Hamada, J. Phys. Chem. **100**, 8777 (1996).

[44] F. Castet and B. Champagne, J. Phys. Chem. A **105**, 1366 (2001).

[45] W.-D. Cheng, D.-S. Wu, H. Zhang, X.-D. Li, D.-G. Chen, Y.-Z. Lang, Y.-C. Zhang and Y.-J. Gong, J. Phys. Chem. B **108**, 12658 (2004).

[46] H. Reis, M. G. Papadopoulos, C. Hattig, J. G. Ángyán and R. W. Munn, J. Chem. Phys. **112**, 6161 (2000).

[47] C. Lin and K. Wu, Chem. Phys. Lett. **321**, 83 (2000).

[48] J. D. Jackson, *Classical Electrodynamics, 3rd ed.* (Wiley, New York, 1998).

[49] T. Kushida, *Hikari Bussei Butsurigaku, in Japanese* (Asakura, Tokyo, 1991).

[50] S. Mukamel, *Principles of Nonlinear Optical Spectroscopy* (Oxford University Press, New York, 1995).

[51] G. R. Fleming and M. Cho, Annu. Rev. Phys. Chem. **47**, 109 (1996).

[52] D. C. Rapaport, *The art of molecular dynamics simulation, 2nd ed.* (Cambridge University Press, Cambridge, 2004).

[53] A. Leach, *Molecular Modeling: Principles and Applications, 2nd ed.* (Prentice Hall, New Jersey, 2001).

[54] U. Alon, *An Introduction to Systems Biology: Design Principles of Biological Circuits* (Chapman & Hall/CRC, New York, 2006).

[55] D. C. Rapaport, *The art of molecular dynamics simulation* (Cambridge University Press, Cambridge, 2004).

[56] K. Kwac and M. Cho, J. Chem. Phys. **119**, 2247 (2003).

[57] C. Kittel, *Introduction to Solid State Physics* (Wiley, New York, 1995).

[58] P. W. Anderson, Nature (London) **177**, 393 (1972).

[59] O. V. Prezhdo and P. J. Rossky, Phys. Rev. Lett. **81**, 5294 (1998).

[60] W. Greiner, L. Neise, and H. Stöcker, *Thermodynamics and Statistical Mechanics* (Springer-Verlag, New York, 1995).

[61] M. Toda, R. Kubo, and N. Saito, *Statistical Physics I: Equilibrium statistical mechanics* (Springer-Verlag, Berlin, 1992); R. Kubo, M. Toda, and N. Hashitsume, *Statistical Physics II: Nonequilibrium Statistical Mechanics* (Springer-Verlag, Berlin, 1991).

[62] R. W. Boyd, *Nonlinear Optics* (Academic Press, San Diego, 2003).

[63] R. Kubo, J. Phys. Soc. Japan **17**, 1100 (1962).

[64] W. B. Bosma, Y. J. Yan, and S. Mukamel, Phys. Rev. A **42**, 6920 (1990).

[65] M. Cho, J.-Y. Yu, T. Joo, Y. Nagasawa, S. A. Passino, and G. R. Fleming, J. Phys. Chem. **100**, 11944 (1996).

[66] G. R. Fleming and M. Cho, Annu. Rev. Phys. Chem. **47**, 109 (1996).

[67] Y. Nagasawa, S. A. Passino, T. Joo, and G. R. Fleming, J. Chem. Phys. **106**, 4840 (1997).

[68] R. Jimenez, G. Salazar, J. Yin, T. Joo, and F. E. Romesberg, Proc. Natl. Acad. Sci. U.S.A. **101**, 3803 (2004).

[69] H. Grabert, P. Schramm, and G.-L. Ingold, Phys. Reports **168**, 115 (1988).

[70] M. Sugisaki, K. Yanagi, R. J. Cogdell, and H. Hashimoto, Phys. Rev. B **75**, 155110 (2007).

[71] Y. Tanimura and S. Mukamel, Phys. Rev. E **47**, 118 (1993).

[72] J. L. Oudar and J. Zyss, Phys. Rev. A **26**, 2016 (1982).

[73] J. Zyss and J. L. Oudar, Phys. Rev. A **26**, 2028 (1982).

[74] D. S. Chemla, and J. Zyss, *Nonlinear Optical Properties of Organic Molecules and Crystals, Vol. 1, 2*, (Academic Press Inc., Orland, 1987).

[75] M. Cho, H. M. Vaswani, T. Brixner, J. Stenger, and G. R. Fleming, J. Phys. Chem. B **109**, 10542 (2005).

[76] H. M. Vaswani, J. Stenger, P. Fromme, and G. R. Fleming, J. Phys. Chem. B **110**, 26303 (2006).

[77] T. Polívka and V. Sundström, Chem. Rev. **104**, 2021 (2004).

[78] H. Hashimoto, K. Yanagi, M. Yoshizawa, D. Polli, G. Cerullo, G. Lanzani, S. De Silvestri, A. T. Gardiner, and R. J. Cogdell, Arch. Biochem. Biophys. **430**, 61 (2004).

[79] Y. Koyama, F. S. Rondonuwu, R. Fujii, and Y. Watanabe, Biopolymers **74**, 2 (2004).

[80] R. Z. B. Desamero, V. Chynwat, I. van der Hoef, F. J. Jansen, J. Lugtenburg, D. Gosztola, M. R. Wasielewski, A. Cua, D. F. Bocian, and H. A. Frank, J. Phys. Chem. B **102**, 8151 (1998).

[81] J.-P. Zhang, R. Fujii, P. Qian, T. Inaba, T. Mizoguchi, Y. Koyama, K. Onaka, Y. Watanabe, and H. Nagae, J. Phys. Chem. B **104**, 3683 (2000).

[82] M. Yoshizawa, H. Aoki, and H. Hashimoto, Phys. Rev. B **63**, 180301(R) (2001).

[83] M. Yoshizawa, H. Aoki, M. Ue, and H. Hashimoto, Phys. Rev. B **67**, 174302 (2003).

[84] D. W. McCamant, P. Kukura, and R. A. Mathies, J. Phys. Chem. A **107**, 8208 (2003).

[85] Y. Koyama, M. Kuki, R. O. Andersson, and T. Gillbro, Photochem. Photobiol. **63**, 243 (1996).

[86] J. Savolainen, R. Fanciulli, N. Dijkhuizen, A. L. Moore, J. Hauer, T. Buckup, M. Motzkus, and J. L. Herek, Proc. Natl. Acad. Sci. U.S.A. **105**, 7641 (2008).

[87] J. Hauer, T. Buckup, and M. Motzkus, Chem. Phys. **350**, 220 (2008).

[88] T. Buckup, T. Lebold, A. Weigel, W. Wohlleben and M. Motzkus, J. Photochem. Photobiol. A **180**, 314 (2006).

[89] J. Hauer, T. Buckup, and M. Motzkus, J. Phys. Chem. A **111**, 10517 (2007).

[90] D. Polli, M. R. Antognazza, D. Brida, G. Lanzani, G. Cerullo, S. D. Silvestri, Chem. Phys. **350**, 45 (2008).

[91] M. Sugisaki, M. Fujiwara, K. Yanagi, R. J. Cogdell, and H. Hashimoto, Photosynth. Res. **95**, 299 (2008).

[92] P. Tavan and K. Schulten, J. Chem. Phys. **85**, 6602 (1986).

[93] P. Tavan and K. Schulten, Phys. Rev. B **36**, 4337 (1987).

[94] T. Buckup, J. Savolainen, W. Wohlleben, J. L. Herek, H. Hashimoto, R. R. B. Correia, and M. Motzkus, J. Chem. Phys. **125**, 194505 (2006).

[95] D. Kosumi, K. Yanagi, R. Fujii, H. Hashimoto, and M. Yoshizawa, Chem. Phys. Lett. **425**, 66 (2006).

[96] G. Cerullo, D. Polli, G. Lanzani, S. De Silvestri, H. Hashimoto, and R. J. Cogdell, Science **298**, 22395 (2002).

[97] F. S. Rondonuwu, K. Yokoyama, R. Fujii, Y. Koyama, R. J. Cogdell, and Y. Watanabe, Chem. Phys. Lett. **390**, 314 (2004).

[98] A. Shirakawa and T. Kobayashi, Appl .Phys. Lett. **72**, 147 (1998).

[99] A. Shirakawa, I. Sakane, and T. Kobayashi, Opt. Lett. **23**, 1292 (1998).

[100] G. Cerullo, M. Nisoli, and S. D. Silvestri, Appl .Phys. Lett. **71**, 3616 (1997).

[101] G. Cerullo, M. Nisoli, S. Stagira, and S. D. Silvestri, Opt. Lett. **23**, 1283 (1998).

[102] A. Shirakawa, his PhD dissertation in 1998 at University of Tokyo, Japan.

[103] K. Yanagi, A. T. Gardiner, R. J. Cogdell, and H. Hashimoto, Phys. Rev. B **71**, 195118 (2005).

[104] S. L. Dexheimer, Q. Wang, L. A. Peteanu, W. T. Pollard, R. A. Mathies, and C. V. Shank, Chem. Phys. Lett. **188**, 61 (1992).

[105] Q. Wang, R. W. Schoenlein, L. A. Peteanu, R. A. Mathies, and C. V. Shank, Science **266**, 422 (1994).

[106] U. Banin and S. Ruhman, J. Chem. Phys. **98**, 4391 (1993).

[107] G. Cerullo, G. Lanzani, M. Zavelani-Rossi, and S. De Silvestri, Phys. Rev. B **63**, 241104(R) (2001).

[108] A. E. Johnson and A. B. Myers, J. Chem. Phys. **104**, 2497 (1996).

[109] P.-O. Andersson, S. M. Bachilo, R.-L. Chen, and T. Gillbro, J. Phys. Chem. **99**, 16199 (1995).

[110] A. B. Myers, M. O. Trulson, J. A. Pardoen, C. Heeremans, J. Lugtenburg, and R. A. Mathies, J. Chem. Phys. **84**, 633 (1986).

[111] D. W. McCamant, J. E. Kim, and R. A. Mathies, J. Phys. Chem. A **106**, 6030 (2002).

[112] Y. J. Yan and S. Mukamel, Phys. Rev. A **41**, 6485 (1990).

[113] S. Mukamel, Annu. Rev. Phys. Chem. **41**, 647 (1990).

[114] P. S. Addison, *The Illustrated Wavelet Transform Handbook* (Taylor & Francis, New York, 2002).

[115] M. Hase, M. Kitajima, A. M. Constantinescu, and H. Petek, Nature (London) **426**, 51 (2003).

[116] M. Hase, M. Kitajima, S. I. Nakashima, and K. Mizoguchi, Phys. Rev. Lett. **88**, 067401 (2002).

[117] O. V. Misochko, M. Hase, K. Ishioka, and M. Kitajima, Phys. Rev. Lett. **92**, 197401 (2004).

[118] P. Kukura, R. Frontiera, and R. A. Mathies, Phys. Rev. Lett. **96**, 238303 (2006).

[119] A. Laubereau and W. Kaiser, Rev. Mod. Phys. **50**, 607 (1978).

[120] M. Hase, K. Mizoguchi, H. Harima, S. I. Nakashima, and K. Sakai, Phys. Rev. B **58**, 5448 (1998).

[121] A. Kummrow and A. Lau, Appl. Phys. B **63**, 209 (1996).

[122] S. Mukamel, Phys. Rev. A **28**, 3480 (1983).

[123] R. W. Boyd and S. Mukamel, Phys. Rev. A **29**, 1973 (1984).

[124] H. Kamisaka, S. V. Kilina, K. Yamashita, and O. V. Prezhdo, Nano Lett. **6**, 2295 (2006).

[125] P.-O. Andersson and T. Gillbro, J. Chem. Phys. **103**, 2509 (1995).

[126] J. L. Brédas, C. Adant, P. Tackx, and A. Persoons, Chem. Rev. **94**, 243 (1994).

[127] R. E. Martin and F. Diederich, Angew. Chem. Int. Ed. **38**, 1350 (1999).

[128] J. R. Heflin, K. Y. Wong, O. Zamani-Khamiri, and A. F. Garito, Phys. Rev. B **38**, 1573(R) (1988).

[129] G. P. Zhang, and T. F. George, Phys. Rev. B **63**, 113107 (2001).

[130] For example, Z. G. Soos and D. Mukhopadhyay, J. Chem. Phys. **101**, 5515 (1994); D. Beljonne, J. Cornil, Z. Shaui, J. L. Brédas, F. Rohlfing, D. D. C. Bradley, W. E. Torruellas, V. Ricci, and G. I. Stegeman, Phys. Rev. B **55**, 1505 (1997).

[131] S. Aramaki, W. Torruellas, R. Zanoni, and G. I. Stegeman, Opt. Commun. **85**, 527 (1991).

[132] J. B. van Beek, F. Kajzar, and A. C. Albrecht, Chem. Phys. **161**, 299 (1992); J. Chem. Phys. **95**, 6400 (1991).

[133] G. Puccetti, M. Blanchard-Desce, I. Ledoux, J. M. Lehn, J. Zyss, J. Phys. Chem. **97**, 9385 (1993).

[134] F. Kajzar and J. Messier, Phys. Rev. A **32**, 2352 (1985).

[135] U. Gubler and C. Bosshard, Phys. Rev. B **61**, 10702 (2000).

[136] R. L. Sutherland, *Handbook of Nonlinear Optics* (MARCEL DEKKER, New York, 1996).

[137] P. Pavlides and D. Pugh, J. Phys.: Condens. Matt. 3, 967 (1991).

[138] Y. R. Shen, *The Principles of Nonlinear Optics* (Wiley, Hoboken NJ, 2003).

[139] T. Geisler, J. C. Peterson, T. Bjornholm, E. Fischer, J. Larsen, C. Dehu, J. L. Brédas, G. V. Tormos, P. N. Nugara, M. P. Cava, and R. M. Metzger, J. Phys. Chem **98**, 10102 (1994)..

[140] F. Kajzar, J. Messier, and C. Rosilio, J. Appl. Phys. **60**, 3040 (1986).

[141] F. Kajzar and J. Messier, Phys. Rev. A **32**, 2352 (1985).

[142] Website of Sigma: http://www.sigma-koki.com/english/index.html

[143] I. D. Nikolov and C. D. Ivanov, Appl. Opt. **39**, 2067 (2000).

[144] F. Kajzar and J. Messier, Phys. Rev. A **32**, 2352 (1985).

[145] R. L. Christensen, E. A. Barney, R. D. Broene, M. G. I. Galinato, and H. Frank, Arch. Biochem. Biophys. **430**, 30 (2004).

[146] I. D. W. Samuel *et al.*, I. Ledoux, C. Dhenaut, J. Zyss, H. H. Fox, R. R. Schrock, and R. J. Silbey, Science **265**, 1070 (1994).

[147] M. Fujiwara, K. Yamauchi, M. Sugisaki, A. Gall, B. Robert, R. J. Cogdell, and H. Hashimoto, Phys. Rev. B **77**, 205118 (2008).

[148] A. Mathy, K. Ueberhofen, R. Schenk, H. Gregorius, R. Garay, K. Müllen, C. Bubeck, Phys. Rev. B **53**, 4367 (1996).

[149] P. Y. Han, M. Tani, F. Pan and X.-C. Zhang, Opt. Lett. **25**, 675 (2000).

[150] J. J. Carey, R. T. Bailey, D. Pugh, J. N. Sherwood, F. R. Cruickshank and K. Wynne, Appl. Phys. Lett. **81**, 4335 (2002).

[151] T. Taniuchi, S. Okada and H. Nakanishi, J. Appl. Phys. **95**, 5984 (2004).

[152] B. F. Levine, C. G. Bethea, C. D. Thurmond, R. T. Lynch and J. L. Bernstein, J. Appl. Phys. **50**, 2523 (1979).

[153] G. F. Lipscomb, A. F. Garito and R. S. Narang, J. Chem. Phys. **75**, 1509 (1981).

[154] J. O. White, D. Hulin, M. Joffre, A. Migus, A. Antonetti, E. Toussaere, R. Hierle and J. Zyss, Appl. Phys. Lett. **64**, 264 (1994).

[155] H. Hashimoto, Y. Okada, H. Fujimura, M. Morioka, O. Sugihara, N. Okamoto and R. Matsushima, Jpn. J. Appl. Phys. **36**, 6754 (1997).

[156] H. Hashimoto, H. Takahashi, T. Yamada, K. Kuroyanagi and T. Kobayashi, J. Phys.: Condens. Matter **13**, L529 (2001).

[157] K. Kuroyanagi, M. Fujiwara, H. Hashimoto, H. Takahashi, S. Aoshima and Y. Tsuchiya, Jpn. J. Appl. Phys. **45**, 4068 (2006).

[158] H. Hashimoto, Y. Okada, N. Okamoto and R. Matsushima, J. Lumin. **87-89**, 886 (2000).

[159] J. Jerphagnon and S. K. Kurtz, Phys. Rev. B **1**, 1739 (1970).

[160] E. Rubinstein, M. E. Glicksman, B. W. Mangum, Q. T. Fang and N. B. Singh, J. Cryst. Growth **89**, 101 (1988).

[161] W. G. Pfann, *Zone Melting* (Wiley, New York, 1966).

[162] J. N. Sherwood and S. J. Thomson, J. Sci. Instrum. **37**, 242 (1960).

[163] L. V. Azároff, *Elements of X-ray Crystallography* (McGraw-Hill, New York, 1968).

[164] L. J. Farrugia, J. Appl. Crystallogr. **32**, 837 (1999).

[165] D. N. Nikogosyan, *Nonlinear Optical Crystals*, (Springer Inc., New York, 2005).

[166] I. Shoji, T. Kondo and R. Ito, Opt. Quant. Electron. **34**, 797 (2002).

[167] B. F. Levine, C. G. Bethea, C. D. Thurmond, R. T. Lynch and J. L. Bernstein, J. Appl. Phys. **50**, 2523 (1979).

[168] G. Knöpfle, C. Bosshard, R. Schlesser and P. Günter, IEEE J. Quantum Electron. **30**, 1303 (1994).

[169] C. Jung, B. K. Rhee and D. Kim, Appl. Opt. **39**, 5142 (2000).

[170] J. Ducuing and N. Bloembergen, Phys. Rev. Lett. **10**, 474 (1963).

[171] A. S. Davydov, *Theory of Molecular Excitons* (Plenum Press, New York, 1971).

[172] G. Ferguson, C. Glidewell, J. N. Low, J. M. S. Skakle and J. L. Wardell, Acta Crystallogr., Sect.C **57**, 315 (2001).

[173] C. M. Whitacker, E. V. Patterson, K. L. Kott and R. J. McMahon, J. Am. Chem. Soc. **118**, 9966 (1996).

[174] M. Hoffmann, K. Scmidt, T. Fritz, T. Hasche, V. M. Agranovich and K. Leo, Chem. Phys. **258**, 73 (2000), and references therein.

[175] J. F. Ward, Rev. Mod. Phys. **37**. 1 (1965).

[176] S. D. Bella, M. A. Ratner and T. J. Marks, J. Am. Chem. Soc. **114**, 5842 (1992).

[177] R. Vallée, P. Damman, M. Dosiere, E. Toussaere and J. Zyss, J. Am. Chem. Soc. **122**, 6701 (2000).

[178] J. R. Heflin and A. F. Garito, in *Nonlinear optical materials*, edited by H. Kuhn and J. Robillard, (CRC Press, New York, 1991), p. 13.

[179] W. Bartkowiak and R. Zaleśny, in *Challenges and Advances in Computational Chemistry and Physics*, edited by M. G. Papadopoulos, A. J. Sadlej, and J. Leszczynski (Springer, Netherlands, 2007), p. 129.

[180] R. L. Christensen, *The Photochemistry of Carotenoids, in Advances in Photosynthesis and Respiration*, edited by H. A. Frank, A. J. Young, G. Britton and R. J. Cogdell, (Springer, Netherlands, 2006), p. 137.

[181] E. T. J. Nibbering and T. Elsaesser, Chem. Rev. **104**, 1887 (2004).

[182] S. Mukamel, Phys. Rev. A **28**, 3480 (1983).

[183] S. Mukamel and R. F. Loring, J. Opt. Soc. Am. B **3**, 595 (1986).

[184] B. J. Orr and J. F. Ward, Mol. Phys. **20**, 513 (1971).

[185] D. S. Bethune, J. Opt. Soc. Am. B **6**, 910 (1989).

[186] O. S. Heavens, *Optical Properties of Thin Solid Films* (Dover, Mineola, 1991).